SYNTHESIS AND CHARACTERIZATION OF NEAR-INFRARED LUMINESCENT MANGANESE AND COPPER PIGMENTS

by

EMAN ABDELRAHMAN

(Under the Direction of Tina Salguero)

ABSTRACT

Near-infrared luminescent pigments have been valued throughout history either due to their vivid colors or their meaning for certain cultures. Two blue colored inorganic pigments based on copper and manganese. Egyptian blue, which was synthesized 5,000 years ago was the first synthetic inorganic pigment known to mankind was produced from three simple reactants: copper oxide, calcium carbonate, and silicon dioxide. Around the same time era, faience, quartz-based ceramic often with a colored glassy glaze shares similar components with Egyptian blue pigment. Investigations conducted by our lab using visible induced luminescence on ancient faience samples revealed the presence of Egyptian blue. Manganese blue is a modern inorganic pigment that has been used as a cement whitener and an artist pigment till its production ceased in the 1990s. Manganese blue exhibits stability against light, acids, and bases and in addition displays an emission profile centered at ~1300 nm. For biomedical imaging applications, specifically in the NIR-II windows where better resolution, manganese blue is an ideal candidate for near-infrared biomedical imaging. Chapter 2 discusses the synthesis, nanostructuring, and characterization of manganese blue. Chapter 3 explores, the in-situ synthesis and characterization of Egyptian blue in

faience and chapter 4 investigates different sources of raw materials to achieve the synthesis of Egyptian blue in faience.

INDEX WORDS: Pigments, nanoparticles, blue, faience, Egyptian blue, manganese blue, NIR, melt flux synthesis, biomedical imaging, archaeology

SYNTHESIS AND CHARACTERIZATION OF NEAR-INFRARED LUMINESCENT MANGANESE AND COPPER PIGMENTS

by

EMAN ABDELRAHMAN

B.S., Pharmaceutical Sciences, Ain Shams University (Egypt), May 2006

A Dissertation Submitted to the Graduate Faculty of The University of Georgia in Partial Fulfillment of the Requirements for the Degree

DOCTOR OF PHILOSOPHY

ATHENS, GEORGIA

2022

© 2022

EMAN ABDELRAHMAN

All Rights Reserved

SYNTHESIS AND CHARACTERIZATION OF NEAR-INFRARED LUMINESCENT MANGANESE AND COPPER PIGMENTS

by

EMAN ABDELRAHMAN

Major Professor:	Tina Salguero
Committee:	Paul Schroeder
	Jin Xie

Electronic Version Approved:

Ron Walcott
Vice Provost for Graduate Education and Dean of the Graduate School
The University of Georgia
August 2022

DEDICATION

To my parents – for their unconditional love and endless support

ACKNOWLEDGEMENTS

I would like to start by thanking my father, Dr. Medhat El Dimillawi, my mother, Ms. Suzan Al-Khadrawi, my siblings, Dr. Radwa Medhat and Dr. Ahmed Medhat who have always supported me no matter what and never doubted for a second that I would concur this tough journey. My dear family, I hope to reunite with you one day. Special thanks to my husband, Dr. Alaa Ahmed who held my hands throughout my doctorate years and my lovely precious daughter Lara who inspires me to work hard every day. Of course, I would never forget to thank my cat, Tate, who has been my study companion since the COVID-19 pandemic.

I would like to especially acknowledge my PI, Dr. Tina Salguero. There are no words to describe how an incredible person Dr. Salguero is, whether on the intellectual, professional, or personal level. I deeply thank Dr. Salguero for allowing me the opportunity to volunteer in her lab prior to my admission to the doctoral program and I owe her any knowledge or success in the chemistry or materials field – I would not have accomplished this without your guidance and support. I would also want to extend my gratitude to my committee members Dr. Paul Schroeder and Dr. Jin Xie for their constant support and guidance.

I would also like to sincerely thank all the Salguero group members past and present. I want to thank Matt Seivert, Harshani Rathnaweera, Yassmin Ghafouri, Roshini Ramachandran, Monika Milkovska, Mayra Pedraza, Greg Neher, Matthew Bloodgood, Nick Nugyen, Nicholas Sesing, Casey Rowe, Brad Norvell, and Xena Mansoura. A special thanks to Matt Seivert, my best friend who never hesitated to help me in every way possible and made this journey bearable. Many thanks to Harshani Rathnaweera who held my hand from day one and gladly answered my endless

questions and Matthew Bloodgood for teaching me how to be intricate and thorough when it comes to experiments.

I also wanted to acknowledge the tremendous help and support Dr. Suzanne Ellenberger has provided me over the years. She always helped relieve the burden by teaching my general chemistry classes or helping do my assignments. I will always cherish Dr. Ellenberger's sage advice and the wonderful conversations I have with her.

My special thanks to Georgia Electron Microscopy for all the help and guidance they provided. I would like to start with Dr. Eric Formo for his help with microscopy throughout this long journey and his advice. I would also like to thank the wonderful Ms. Mary Ard, who helped me with carbon coating so many samples and Dr. John Shields for also helping me with microscopy. Further, I would like to thank Mr. Chris Fleisher who helped me create the most wonderful, polished cross-sections and carbon coated my samples for me. I would also like to acknowledge the Dreyfus Foundation through its Special Grant Program in the Chemical Sciences for the support on the faience project. Finally, I want to thank the cast of the "Office" especially Michael Scott, Dwight Schrute, and Pam Beesly!

TABLE OF CONTENTS

Page

ACKNOWLEDGEMENTS v

CHAPTER

1 INTRODUCTION AND LITERATURE REVIEW 1

Near-Infrared Luminescent Quantum Dots 3

Near-Infrared Luminescent Metal Organic Frameworks 4

Persistent Luminescent Phosphors 5

Near-Infrared Luminescent Pigments 6

Melt Flux Synthesis Approach 10

Research Goals 12

References 14

2 SYNTHESIS, NANOSTRUCTURING, AND CHARACTERIZATION OF MANGANESE BLUE PIGMENT 23

Abstract 24

Introduction 25

Experimental 29

Results and Discussion 33

Conclusion 56

References 58

3 THE EGYPTIAN BLUE–EGYPTIAN FAIENCE CONTINUUM 63

Abstract 64

Introduction 64

Experimental 67

Results and Discussion 71

Conclusion 92

References 94

4 INVESTIGATION OF DIFFERENT RAW MATERIALS USED FOR MANUFACTURING EGYPTIAN FAIENCE AND THEIR CORRELATION TO THE IN-SITU SYNTHESIS OF EGYPTIAN BLUE 98

Abstract 99

Introduction 100

Experimental 102

Results and Discussion 108

Conclusion 135

References 138

5 CONCLUSIONS AND FUTURE WORK 142

Conclusions and Future Work 142

References 146

CHAPTER 1

INTRODUCTION AND LITERATURE REVIEW

Luminescence is a broad term encompassing different materials emitting radiation from an electronically or vibrationally excited species not in thermal equilibrium with its environment.[1] Luminescence can be generated in a number of different ways such as chemical or electrochemical reactions, within biological systems, through mechanical force, or by high energy photons.[2] Specifically, near-infrared (NIR) luminescent materials that emit in the NIR region of the electromagnetic spectrum (in the range of ~700 – 2500 nm) have emerged as highly relevant for biomedical imaging and optics application.[4]

A few classes of NIR luminescent materials from the literature include organic molecules like cyanine dye, carbon nanomaterials like carbon nanotubes,[5] NIR fluorescent proteins, and inorganic nanomaterials.[1] Specifically, NIR luminescent materials based on certain d-block metals (manganese, copper, chromium, cobalt, cadmium, zinc, and silver) offer a wide range of properties. Examples include persistent luminescent phosphors based on metals such as manganese, cobalt, nickel, or chromium that be used for biomedical imaging,[6] security inks,[7] and traffic light.[8] Another class includes semiconductor quantum dots containing cadmium, zinc, or silver which are used in applications ranging from remote sensing[9] to night vision[10] and data storage.[11-13] Near infrared metal organic framework based on zinc and copper can potentially be used for biomedical applications[14] and pollution detection.[15] NIR luminescent materials consists of specific compositions that have historically played an important role as pigments, especially

those based on copper and manganese. Applications of these pigments include forensics, [16] optical sensing, [17] and tunable laser materials. [3, 18]

A general distinction in terms of NIR luminescence can be made between solid state semiconductor-based luminescence and the luminescence stemming from discrete ions, organic molecules, or coordination complexes. As illustrated in figure 1.1, the principal mechanism is identical in all cases – the absorption of a photon raises an electron from the ground state to an excited state resulting in the emission of a photon.[2]

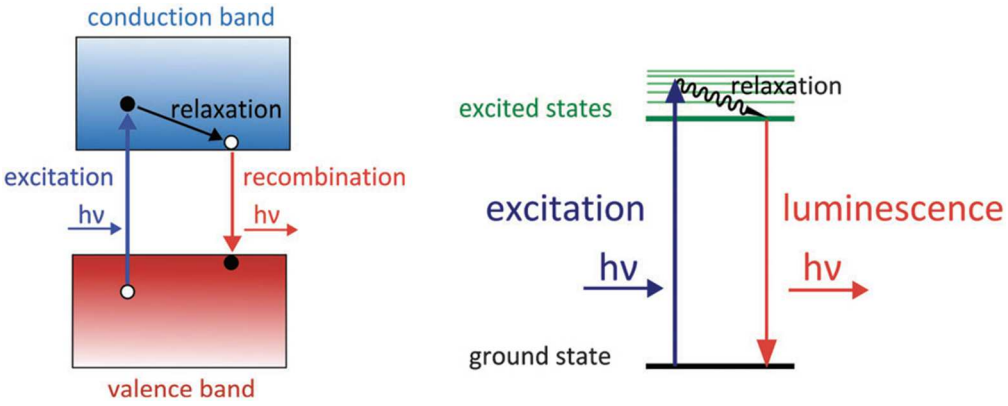

Figure 1.1: Simplified mechanism of semiconductor (electronic bands; left) and molecular based excitation/emission processes (discrete energy levels; right). Adapted with permission from reference[1].

NIR luminescence in a semiconductor-based material consists of four steps. First, charge carriers (electrons or holes) must be excited by radiation (example: UV, VIS, NIR light, electron beam, X-ray radiation, etc.). In the second step, the charge carriers must be stored, and this is dependent on the host material which acts as the trap carrier and the number of charge carriers and defects. In the next step, the captured charge carriers can be released from the traps via thermal, optical, or mechanical disturbance and this depends on the depth of the traps in the host material.

Finally, the excited charge carriers undergo a recombination process, and the long persistent luminescence cycle can start again.[19]

NIR luminescence originating from transition metal ion complexes is more complicated and may be dominated by a variety of charge-transfer processes, such as metal-to-ligand charge transfer, ligand-to-metal charge transfer, and intraligand charge transfer. The emission properties of metal complexes depend on the nature of the metal center, auxiliary ligands, and the local environment.[20] Transitions that result from the transfer of an electron from a primarily ligand orbital to a primarily metal orbital are called metal-to-ligand charge transfer and vice versa is called ligand-to-metal charge transfer. Both metal-to-ligand and ligand-to-metal transitions usually lie at higher energies than d-d transitions and they can be very important in the excitation processes. Intraligand transitions are primarily located on the ligand portion of the molecule and is usually considerably higher in energy than either d-d or charge transfer excited states.[21]

Near-Infrared Luminescent Quantum Dots

Quantum dots are inorganic semiconductor nanoparticles with sizes < 50 nm. The distinct optical properties observed in these compounds, when compared with their bulk counterparts, are due to the existence of quantum confinement effects. The observed quantum confinement effects are directly influenced by the material's composition and physical dimensions.[22] NIR QDs are a specific class of fluorescent probes that emit in the NIR region of the spectra and stand as one of the most promising materials used in pre-clinical setting. Their small size (up to 30 nm), excellent PLQY (up to 45% in aqueous media), high photostability, and biocompatibility are their main advantages over the traditional molecular dyes.[23]

Near infrared luminescent quantum dots based on Cd^{2+}, Cu^{+}, Pb^{2+}, and Ag^{+} have been reported in the literature. Cui et al. reported the synthesis of water-soluble and low toxicity CdS quantum dots with NIR luminescence (~730 nm) through confinement into bovine serum albumin templates with the mediation of L-cysteine.[24] Cu^{+} has been incorporated both as a dopant and a component of quantum dots that results in a broadened emission profile and a bathochromic shift in emission maxima. Yoon et al reported the synthesis of CuInS (CIS) quantum dots and implementing post-alloying of the pre-grown CIS with Ag to shift the NIR emission from 744 nm to 806 nm.[25] Site selective surface passivation synthesis of near infrared luminescent PbS quantum dots has been reported by Zhang et al. for LED application.[26]

Near-Infrared Luminescent Metal Organic Frameworks

Metal organic frameworks (MOFs) are an extensive class of crystalline materials with ultrahigh porosity (up to 90% free volume and enormous internal surface area extending beyond 6000 m^2/g. MOFs have a high degree of variability for both the organic and inorganic components of their structures making them a material of interest for applications such as storage material for hydrogen and methane, membranes, thin films, biomedical imaging, and catalysis.[27] D-block metals such as Co^{2+}, Ni^{2+}, Zn^{2+}, Cd^{2+}, Ti^{2+}, or Fe^{2+} and lanthanides such as Ce^{3+}, Gd^{3+}, Eu^{3+}, or Tb^{3+} along with diverse multi-dentate ligands enhance the properties of MOFs in the NIR region.[28]

Sun et al. investigated the synthesis of Ln^{3+}/Ag^{+}@MOF-1 (Ln = Yb, Nd, Er) to create a novel sensitizer for NIR emission through the interaction of the lanthanide ions with the Ag^{+} resulting in characteristic emissions at 980, 1064, and 1538 nm for Yb, Nd, and Er respectively.[29,30] Aboshyan-Sorgho et al. demonstrated a simple approach for optimizing long-lived near infrared lanthanide-centered luminescence using trivalent chromium chromophores as sensitizers.

Excitation into the Cr(^{2}E)-centered levels with near infrared radiation at 752 nm induces intramolecular Cr ⟶ Ln (Ln = Nd, Er, or Yb) energy transfer, which eventually sensitizes luminescence in the spectral range of 1000 – 1700 nm.[31] In addition, Wang et al. recently reported the synthesis of Cd_2TTFTB (TTFTB = tetrathiafulvalene tetrabenzoate) MOF crystals with broad NIR emission.[32]

Persistent Luminescent Phosphors

Phosphors are materials that can absorb high energy (short wavelength) and convert down convert them into lower energy (longer wavelength). Persistent luminescence also known as afterglow or long-lasting phosphorescence is an optical phenomenon resulted in the luminescence of a phosphor that lasts for several seconds to a few days after switching off the excitation source. Near infrared persistent luminescent phosphors emit in the range of 650 – 1400 nm and can be incorporated in devices with diverse applications in the spectroscopic,[34,35] biomedical imaging,[36,37] and agricultural fields (add more references).[38,39]

Near infrared persistent luminescent phosphors consist of a variety of host materials such as sulfides, aluminates, silicates, germanates, gallates, titanates, and nitrides doped with d-block metal ions such as Cr^{3+}, Mn^{4+}/Mn^{5+}/Mn^{2+}, Co^{2+}, and Ni^{2+}.[8,33] For example, in $ZnGa_2O_4$: Ni^{2+}, occupies Ga^{3+} site in the $ZnGa_2O_4$ spinel structure which gives near infrared persistent luminescent properties after excitation with ultraviolet light at 365 nm. In another example, $Ca_{14}Zn_6Ga_{10}O_{35}$:Mn phosphor contains both Mn^{4+} and Mn^{5+}, leading to an energy transfer process from Mn^{4+} to Mn^{5+} that causes the material to emit at 1152 nm.[40] In $ZnGa_2O_4$: Cr^{3+}, the Cr^{3+} ions impart luminescence properties to the spinel structure centered at 700 nm after excitation with a wavelength in the range of 250 – 580 nm (ultraviolet to visible).[41]

Near-Infrared Luminescent Pigments

Near infrared luminescent pigments (also known as phosphors or luminophores) are synthetically-produced, crystalline compounds that absorb energy followed by the emission of light with a lower energy, i.e., a longer wavelength. Crystal lattices suitable for inorganic luminescent materials are based on colorless silicates, phosphates, sulfides, oxides, or halides predominantly from alkaline earth metals or zinc. Activator ions like Ni^{2+}, Cr^{4+}, Mn^{5+}, Ag^{+} , and Cu^{2+} are incorporated as emission centers in the crystal lattice. The choice of the activator is critical because it determines the target emission wavelength, whereas the host crystal lattice affects the performance and the characteristics of emission. [42,43] The decay time of the emitted light depends on the activator metal center, lattice geometries, and the influence of the crystal field on the host lattice. [44]

Several examples of near infrared luminescent pigments are mentioned in the literature based on d-block metals such as manganese an example is manganese blue, [3, 45-47] or like Cr^{3+}-doped $Bi_2Ga_{(4-x)}Al_xO_9$, [48] or cadmium such as CdS and CdSe,[49, 50] and copper based near infrared luminescent pigments is metal copper tetrasilicates such as calcium copper tetrasilicate, barium copper tetrasilicate, and strontium copper tetrasilicate.[51-53]

Manganese Blue Pigment

Manganese blue is a modern, synthetic, green blue pigment with a composition of $[BaSO_4]_x \cdot [BaMnO_4]_{1-x}$ (color index, CI77112)[54] and the pigment was manufactured from 1935 to the 1990s until the 1990s due to concerns regarding the environmental impact of its production. Manganese blue was first mentioned in the patent literature in 1935 by I.G. Farbenindustrie AG,[45] and it has been used as a cement colorant and an artist's pigment.

Upon examination of the photophysical properties of manganese blue pigment, it was found that the pigment has a broad absorption band between 500 nm and 1250 nm as shown in figure 1.2 which is due to the very strong coupling between the electronic transitions and lattice phonons, typical of transition metal systems. Accorsi et al. and Brunold et al., confirmed according to ligand field theory the presence of near-IR band system extended from 800 – 900 nm which is assigned to $^2E \longrightarrow {}^2T$ ligand field transition split in three nearly overlapping d-d bands as a consequence of Jahn-Teller $T_d \longrightarrow C_{2v}$ distortion. The photoluminescent quantum yield obtained at ~1300 nm is 0.5% and has a corresponding decay time of 7.1 μs.[3,46]

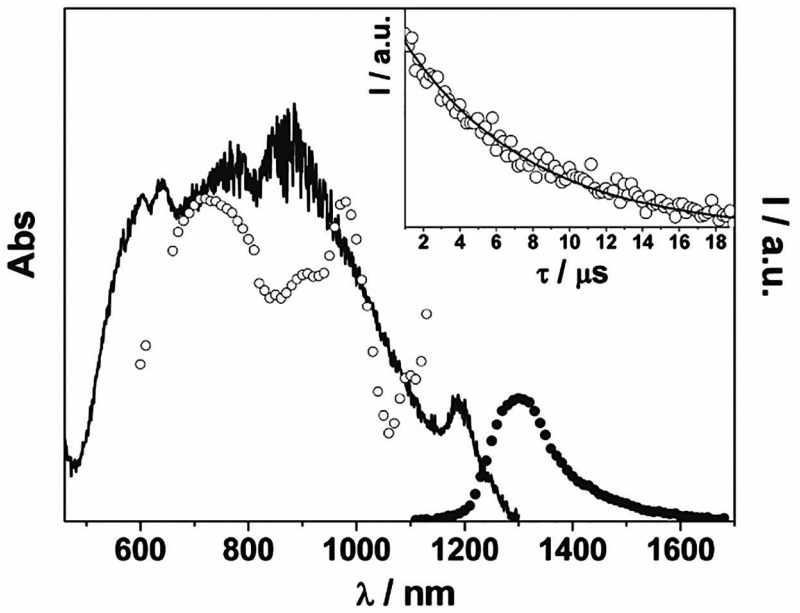

Figure 1.2: Absorbance (black solid line), excitation (hollow circles), and full emission (solid circles) spectra of synthetic manganese blue. Inset: Luminescence decay (7.1 μs, λ_{exc} = 637 nm). Adapted with permission from reference.[36]

It has been proposed that manganese acquires a 5+ or 6+ oxidation state doped in the barium sulfate matrix, and it replaces the sulfur in a 6+ oxidation state which is tetrahedrally coordinated to four oxygens. Brunold et al., conducted photoluminescence studies and determined

that the oxidation state of manganese is a 6+ oxidation state. On the other hand, Accorsi et al. conducted DFT calculations to simulate theoretical photoluminescence spectra for manganese blue that matched the results obtained by Brunold et al. When manganese in a 6+ oxidation state is doped in the barium sulfate matrix, this incurs a distortion in the symmetry of the sulfate ion from C_s to C_{2v} as indicated by the variation in the O-S-O angles between 105.9° and 114.1° as shown in Figure 1.3. A year later, Reinen et al. reported the oxidation state of manganese blue as 5+ oxidation state based on EPR studies.[47] Based on the green-blue color of manganese blue, Mn^{5+} tetrahedrally coordinated to four oxygens absorbs in the green-blue region of the electromagnetic spectra are while Mn^{6+} tetrahedrally coordinated to four oxygens absorbs in the violet-blue region.[55]

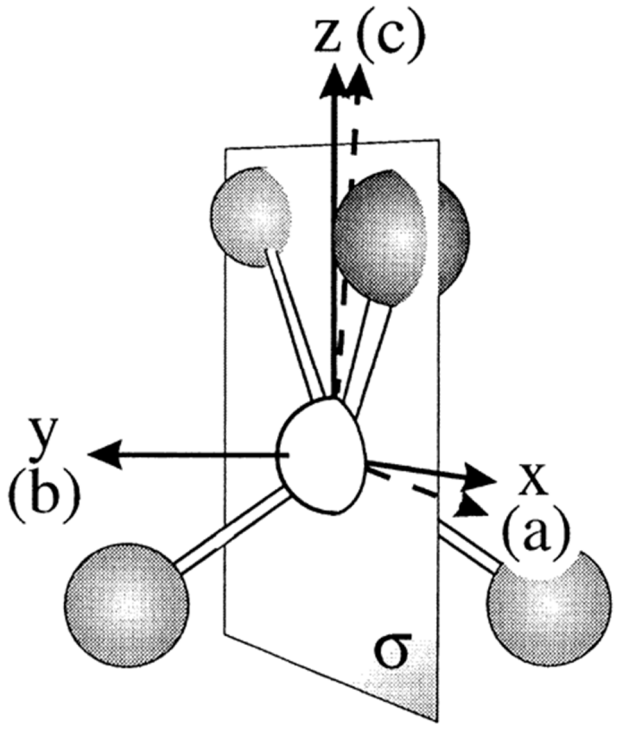

Figure 1.3: An illustration of the sulfate ion (SO_4^{2-}) in barium sulfate. The axes x, y, and z are crystallographic axes and a, b, and c are the molecular axes. The only symmetry element in the SO_4^{2-} ion is the mirror symmetry (σ). When manganese replaces sulfur, the symmetry of the sulfate ion is distorted and becomes approximately C_{2v}. Adapted with permission from reference.[2]

Metal Copper tetrasilicates

Metal copper tetrasilicates are blue, copper-containing inorganic pigments with a composition $ACuSi_4O_{10}$ (A = Ca, Sr, Ba) and the gillespite-type structure. These materials occur naturally as very rare minerals, namely cuprorivaite ($CaCuSi_4O_{10}$), effenbergerite ($BaCuSi_4O_{10}$), and wesselsite ($SrCuSi_4O_{10}$).[56] Fortunately, metal copper tetrasilicates are relatively straight forward to synthesize, which enabled Egyptian Blue, $CaCuSi_4O_{10}$, and Han Blue, $BaCuSi_4O_{10}$, to be utilized as important ancient pigments for thousands of years. The strontium variant, $SrCuSi_4O_{10}$, is less common.[57] Egyptian Blue is credited as being the first synthetic pigment, with the earliest known use dated to 3300 – 3200 BCE in ancient Egypt[58,59]. Han blue has been used at least since 800 BC in ancient China.[53,60] The structure of the metal copper tetrasilicate family is characterized by a $[SiO_4]^{4-}$ tetrahedra linked by copper ions in the square planar position with an alkaline earth metal ion in an 8-fold coordination sitting between the metal silicate layers as shown in figure 1.4.[51,61]

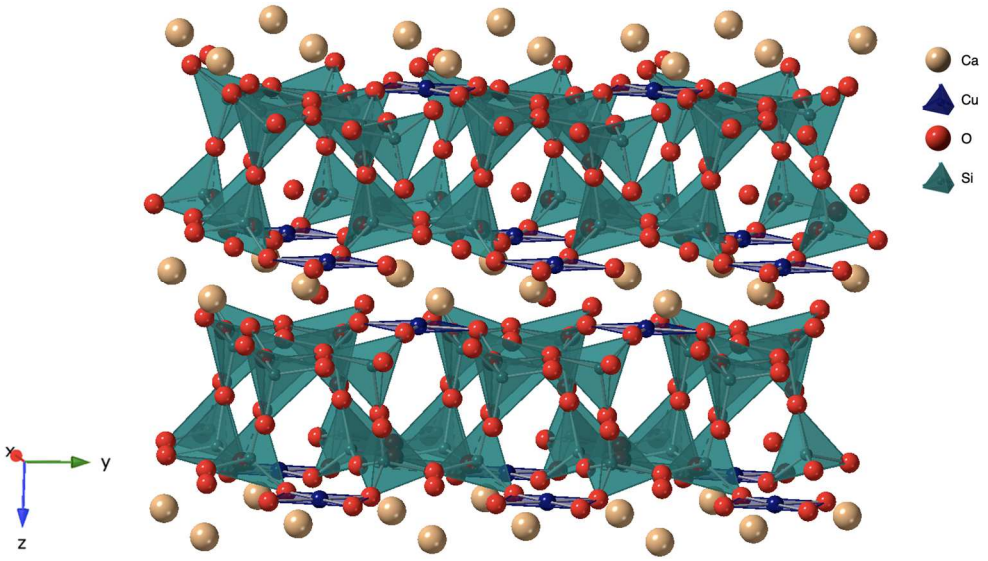

Figure 1.4: Crystal structure of $CaCuSi_4O_{10}$

The source of the brilliant blue color and the NIR luminescence of the metal copper tetrasilicates is the photoactive ion square planer Cu^{2+} ion which is in D_{4h} coordination due to Jahn-

Teller effect and lattice constraints. The change in symmetry from O_h to D_{4h} splits the ground state E_g in to B_{1g} and A_{1g} and T_{2g} into B_{2g} and E_g as shown in figure 1.5.[62] When the pigment is excited in the visible region, three transitions occur: B_{1g} to A_{1g}, E_g, and B_{2g}. The last transition is the one responsible for the emission. The emission for $CaCuSi_4O_{10}$ is a relatively sharp, symmetric band centered at around 910 nm.

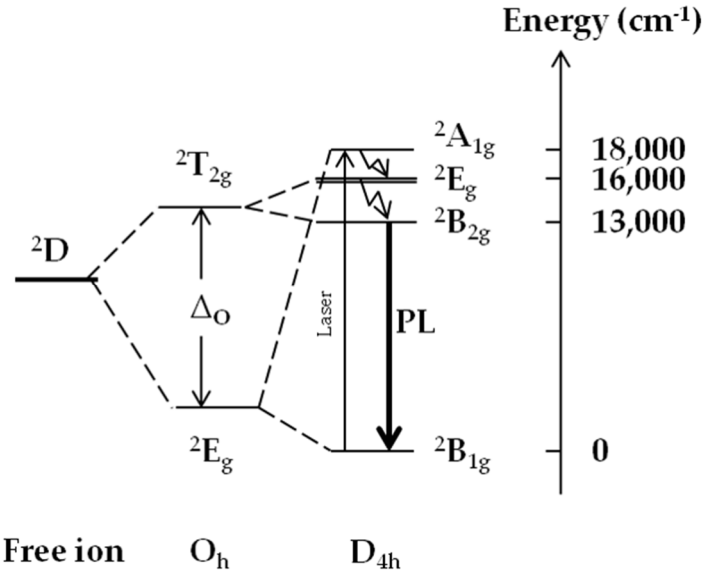

Figure 1.5: Crystal field splitting for Cu^{2+} ion in $ACuSi_4O_{10}$. Adapted with permission from reference.[23]

Melt Flux Synthesis Approach

The synthesis of manganese blue and Egyptian blue pigments via melt flux synthesis route has been reported in the literature.[45,52,63] Flux growth is also known as high temperature solution growth. The flux melts at high temperatures and acts as the solvent in a solution growth. These high-temperature solutions or fluxes are simple inorganic compounds, such as $BaCl_2$, Bi_2O_3, B_2O_3, KOH, PbO, or Na_2CO_3, which melt at conveniently low temperatures. Often combinations of inorganic compounds are used to form an even lower melting eutectic, which can reduce the

melting point of a "high-temperature solution" below 200 °C.[64] In a typical flux growth, first the components of the target compound are dissolved in a flux, which is usually molten salt, oxide, or metal inside of a refractory crucible. Then, crystal growth takes place under supersaturation controlled by cooling or evaporating the flux. By dissolving the components of a desired compound in a flux with a low melting temperature, sometimes in controlled atmosphere or sealed ampoule, flux growth is good for the growth of a large variety of materials, such as compounds that would sublimate, compounds with a high melting temperature, volatile components, poisonous components, or a phase transition below the melting temperature.[65]

Nanostructured Materials

Nanomaterials are materials with less than 100 nm in size at least in one dimension. Nanomaterials maybe characterized according to dimensionality. For example, nanoparticles are zero-dimensional, nanorods or nanotubes are one-dimensional, and nanosheets are two-dimensional. Nanoparticles are synthesized by various methods that are categorized into bottom-up which involves the build-up of material from atom to clusters to nanoparticles or top-down method in which bulk material is reduced to nanometer scale particles.[67] A reduction in the particle size from bulk to nanoparticles displays improved properties such as particle size distribution and morphology which makes them appealing for applications such as biomedical applications.[68-70]

Research Goals

The work in this dissertation describes the novel melt flux synthesis of manganese blue[45] and Egyptian blue pigments and methods to control the crystal growth of both pigments on the micro and nanoscales. Chapter 2 described the synthesis and nanostructuring of manganese blue nanoparticles. Through our understanding of the nature and chemistry of manganese in the barium sulfate matrix, we were able to obtain a morphology on the micron scale and the green-blue color[71,72] on the macroscopic scale with a more uniform particle size distribution in comparison to the rare and unavailable commercially synthesized manganese blue pigment. We further translated our findings to synthesize the pigment on the nanoscale using nanoscale precursors. For biomedical application purposes, we were able to narrow down the particle size distribution using centrifugation and deposit a layer of amorphous silica on the nanoparticles.[54]

Chapter 3 detailed the in-situ synthesis of Egyptian blue crystals that constitutes of three components, calcium, copper, and silicon in faience which is a very complicated system that has the same overlapping elements as Egyptian blue. By eliminating sodium chloride from our flux mixture, we were able to grow Egyptian blue crystals in faience.[73] By tuning the concentration of calcium and at some instance copper, we created a continuum between Egyptian blue and Egyptian faience both lying at the two extremes of the continuum. In-situ crystal growth of micro-sized Egyptian blue was also achieved by controlling the stoichiometry, or using controlled, or both. Finally, from the continuum, we were able to synthesize Egyptian blue objects.

In chapter 4, we investigated the influence of different source of starting material –calcium, copper, alkali flux, and substrates for faience synthesis – and how they influenced the growth and size of Egyptian blue crystals. Calcium carbonate from calcite or dolomitic deposits, calcium hydroxide the main component of lime, and calcium sulfate found in gypsum were possible archaeological sources for the formation of Egyptian blue in faience.[74-76] Copper oxide, basic

copper(II) carbonate, and Egyptian blue[77] were all examined as possible source of copper for the formation of crystalline Egyptian blue and as colorant for the faience glaze. Serendipitously, we synthesized faience using application glazing method. Halophytic plant ashes appeared to be a better flux source in comparison to natron which suggested a possible purification process conducted in the ancient times for the removal of sodium chloride. Finally, alumina, terracotta, and calcium oxide were tested as substrates for faience. Alumina for lab synthesis, and terracotta used for synthesis of archaeological did not disrupt the synthesis of Egyptian blue crystals while calcium oxide used as a slip layer on terracotta appeared to inhibit the in-situ growth of Egyptian blue in faience.[78,79]

References

1. Verhoeven, J., *Glossary of terms used in photochemistry (IUPAC Recommendations 1996).* Pure and Applied Chemistry, 1996. **68**(12): p. 2223-2286.
2. Heine, J. and K. Müller-Buschbaum, *Engineering metal-based luminescence in coordination polymers and metal–organic frameworks.* Chemical Society Reviews, 2013. **42**(24): p. 9232-9242.
3. Brunold, T.C. and H.U. Güdel, *Absorption and Luminescence Spectroscopy of MnO42--Doped Crystals of BaSO4.* Inorganic chemistry, 1997. **36**(9): p. 1946-1954.
4. Jackson, C.T., et al., *Advances in engineering near-infrared luminescent materials.* Iscience, 2021. **24**(3): p. 102156.
5. Yudasaka, M., et al., *Near-infrared photoluminescent carbon nanotubes for imaging of brown fat.* Scientific reports, 2017. **7**(1): p. 1-12.
6. Zhuang, Y., et al., *A brief review on red to near-infrared persistent luminescence in transition-metal-activated phosphors.* Optical Materials, 2014. **36**(11): p. 1907-1912.
7. Katayama, Y., *Red to near-infrared persistent luminescence in transition metal ion activated phosphors.* Journal of the Ceramic Society of Japan, 2017. **125**(11): p. 793-798.
8. Pellerin, M., et al. *Persistent luminescence of transition metal (Co, Ni...)-doped ZnGa2O4 phosphors for applications in the near-infrared range*. in *Oxide-based Materials and Devices IX*. 2018. International Society for Optics and Photonics.

9. Vázquez-González, M. and C. Carrillo-Carrion, *Analytical strategies based on quantum dots for heavy metal ions detection.* Journal of biomedical optics, 2014. **19**(10): p. 101503.

10. Ouyang, J., et al., *Ag2Te Colloidal Quantum Dots for Near-Infrared-II Photodetectors.* ACS Applied Nano Materials, 2021. **4**(12): p. 13587-13601.

11. Hu, D., et al., *High performance flexible nonvolatile memory based on vertical organic thin film transistor.* Advanced Functional Materials, 2017. **27**(41): p. 1703541.

12. Chen, Y.-C., et al., *Nonvolatile memory thin film transistors using CdSe/ZnS quantum dot-poly (methyl methacrylate) composite layer formed by a two-step spin coating technique.* Journal of Applied Physics, 2012. **112**(3): p. 034518.

13. Lv, Z., et al., *Semiconductor Quantum Dots for Memories and Neuromorphic Computing Systems.* Chemical Reviews, 2020. **120**(9): p. 3941-4006.

14. Arun Kumar, S., et al., *Two-dimensional metal organic frameworks for biomedical applications.* Wiley Interdisciplinary Reviews: Nanomedicine and Nanobiotechnology, 2021. **13**(2): p. e1674.

15. Shi, L., et al., *Environmental pollution analysis based on the luminescent metal organic frameworks: A review.* TrAC Trends in Analytical Chemistry, 2021. **134**: p. 116131.

16. Errington, B., et al., *Micronised Egyptian blue pigment: A novel near-infrared luminescent fingerprint dusting powder.* Dyes and Pigments, 2016. **132**: p. 310-315.

17. Borisov, S.M., et al., *New life of ancient pigments: application in high-performance optical sensing materials.* Analytical chemistry, 2013. **85**(19): p. 9371-9377.

18. Brunold, T.C. and H.U. Güdel, *Absorption and luminescence spectroscopy of manganese-doped BaSO4 crystals.* Chemical Physics Letters, 1996. **257**(1): p. 123-129.

19. Arras, J. and S. Bräse, *The World Needs New Colors: Cutting Edge Mobility Focusing on Long Persistent Luminescence Materials.* ChemPhotoChem, 2018. **2**(2): p. 55-66.

20. Ma, D.L., et al., *Bioactive luminescent transition-metal complexes for biomedical applications.* Angewandte Chemie International Edition, 2013. **52**(30): p. 7666-7682.

21. Fleischauer, P.D. and P. Fleischauer, *Photoluminescence of transition metal coordination compounds.* Chemical Reviews, 1970. **70**(2): p. 199-230.

22. Gil, H.M., et al., *NIR-quantum dots in biomedical imaging and their future.* Iscience, 2021. **24**(3): p. 102189.

23. Resch-Genger, U., et al., *Quantum dots versus organic dyes as fluorescent labels.* Nature Methods, 2008. **5**(9): p. 763-775.

24. Cui, Y., et al., *Facile synthesis of near-infrared emissive CdS quantum dots for live cells imaging.* Journal of Nanoscience and Nanotechnology, 2018. **18**(4): p. 2271-2277.

25. Yoon, S.-Y., et al., *Systematic and Extensive Emission Tuning of Highly Efficient Cu–In–S-Based Quantum Dots from Visible to Near Infrared.* Chemistry of Materials, 2019. **31**(7): p. 2627-2634.

26. Zhang, X., et al., *Stability enhancement of PbS quantum dots by site-selective surface passivation for near-infrared LED application.* Nano Research, 2021. **14**(3): p. 628-634.

27. Zhou, H.-C., J.R. Long, and O.M. Yaghi, *Introduction to metal–organic frameworks*. 2012, ACS Publications. p. 673-674.

28. Younis, S.A., et al., *Metal-organic framework as a photocatalyst: Progress in modulation strategies and environmental/energy applications.* Progress in Energy and Combustion Science, 2020. **81**: p. 100870.

29. Sun, N.-N. and B. Yan, *Near-infrared emission sensitization of lanthanide cation based on Ag+ functionalized metal-organic frameworks.* Journal of Alloys and Compounds, 2018. **765**: p. 63-68.

30. Zou, D., et al., *Near-infrared-emissive metal–organic frameworks.* Dalton Transactions, 2019. **48**(20): p. 6669-6675.

31. Aboshyan-Sorgho, L., et al., *Optimizing Millisecond Time Scale Near-Infrared Emission in Polynuclear Chrome(III)–Lanthanide(III) Complexes.* Journal of the American Chemical Society, 2012. **134**(30): p. 12675-12684.

32. Wang, F., et al., *Broad-Band Near-Infrared Doublet Emission in a Tetrathiafulvalene-Based Metal–Organic Framework.* The Journal of Physical Chemistry Letters, 2020. **11**(3): p. 762-766.

33. Zhou, Z., Y. Li, and M. Peng, *Near-infrared persistent phosphors: Synthesis, design, and applications.* Chemical Engineering Journal, 2020. **399**: p. 125688.

34. Rajendran, V., et al., *Ultra-Broadband Phosphors Converted Near-Infrared Light Emitting Diode with Efficient Radiant Power for Spectroscopy Applications.* ACS Photonics, 2019. **6**(12): p. 3215-3224.

35. Wang, C., et al., *An Ultra-Broadband Near-Infrared Cr3+-Activated Gallogermanate Mg3Ga2GeO8 Phosphor as Light Sources for Food Analysis.* ACS Applied Electronic Materials, 2019. **1**(6): p. 1046-1053.

36. Cao, R., et al., *Near-infrared emission Ba3 (PO4) 2: Mn5+ phosphor and potential application in vivo fluorescence imaging.* Spectrochimica Acta Part A: Molecular and Biomolecular Spectroscopy, 2014. **128**: p. 671-673.

37. Zhang, X., et al., *A general strategy for controllable synthesis of Ba 3 (MO 4) 2: Mn 5+(M= V, P) nanoparticles.* RSC Advances, 2017. **7**(17): p. 10564-10569.

38. De Guzman, G.N.A., S.F. Hu, and R.S. Liu, *Enticing applications of near-infrared phosphors: Review and future perspectives.* Journal of the Chinese Chemical Society, 2021. **68**(2): p. 206-215.

39. Leaño, J.L., et al., *Thermally Stable and Deep Red Luminescence of Sr1–xBax[Mg2Al2N4]:Eu2+ (x = 0–1) Phosphors for Solid State and Agricultural Lighting Applications.* ACS Applied Materials & Interfaces, 2020. **12**(20): p. 23165-23171.

40. Liao, Z., et al., *Energy transfer from Mn4+ to Mn5+ and near infrared emission with wide excitation band in Ca14Zn6Ga10O35: Mn phosphors.* Chemical Engineering Journal, 2020. **395**: p. 125060.

41. da Silva, M.N., et al., *Nanosized ZnGa2O4: Cr3+ spinels as highly luminescent materials for bioimaging.* ACS Applied Nano Materials, 2019. **2**(11): p. 6918-6927.

42. Chan, M.-H., et al., *The optical research progress of nanophosphors composed of transition elements in the fourth period of near-infrared windows I and II for deep-tissue theranostics.* Nanoscale, 2022.

43. Feng, X., et al., *Transition metal ion activated near-infrared luminescent materials.* Progress in Materials Science, 2022: p. 100973.

44. Pfaff, G., *Inorganic pigments*, in *Inorganic Pigments*. 2017, de Gruyter.

45. Erich, K. and M. Georg, *Blue pigment colors and aprocess of preparing them*. 1939, Google Patents.

46. Accorsi, G., et al., *Imaging, photophysical properties and DFT calculations of manganese blue (barium manganate (VI) sulphate)–a modern pigment.* Chemical Communications, 2014. **50**(97): p. 15297-15300.

47. Reinen, D., et al., *The nature of the colour centre in manganese blue.* ZEITSCHRIFT FUR ANORGANISCHE UND ALLGEMEINE CHEMIE, 1998. **624**: p. 438-442.

48. Liu, C., et al., *Near-infrared luminescence and color tunable chromophores based on Cr3+-doped mullite-type Bi2 (Ga, Al) 4O9 solid solutions.* Inorganic Chemistry, 2015. **54**(4): p. 1876-1882.

49. Thoury, M., et al., *Near-infrared luminescence of cadmium pigments: in situ identification and mapping in paintings.* Applied Spectroscopy, 2011. **65**(8): p. 939-951.

50. Cesaratto, A., et al., *Analysis of cadmium-based pigments with time-resolved photoluminescence.* Analytical Methods, 2014. **6**(1): p. 130-138.

51. Johnson-McDaniel, D., et al., *Nanoscience of an ancient pigment.* Journal of the American Chemical Society, 2013. **135**(5): p. 1677-1679.

52. Johnson-McDaniel, D. and T.T. Salguero, *Exfoliation of Egyptian blue and Han blue, two alkali earth copper silicate-based pigments.* JoVE (Journal of Visualized Experiments), 2014(86): p. e51686.

53. Berke, H., *The invention of blue and purple pigments in ancient times.* Chemical Society Reviews, 2007. **36**(1): p. 15-30.

54. Abe, N., K. Kanemaru, and M. Yokoyama, *Method of coating inorganic pigments (ultramarine and bronze powder) with dense amorphous silica*. 1983, Google Patents.

55. Lachwa, H. and D. Reinen, *Color and electronic structure of manganese (V) and manganese (VI) in tetrahedral oxo coordination. A spectroscopic investigation.* Inorganic Chemistry, 1989. **28**(6): p. 1044-1053.

56. Barbar, S., K. Patel, and S. Kumar, *Structural, optical and magnetic properties of MCuSi4O10 (M= Ba and Sr) blue pigments.* Journal of Materials Science: Materials in Electronics, 2017. **28**(4): p. 3716-3724.

57. Berdahl, P., et al., *High quantum yield of the Egyptian blue family of infrared phosphors (MCuSi4O10, M= Ca, Sr, Ba).* Journal of Applied Physics, 2018. **123**(19): p. 193103.

58. Accorsi, G., et al., *The exceptional near-infrared luminescence properties of cuprorivaite (Egyptian blue).* Chemical Communications, 2009(23): p. 3392-3394.

59. Mazzocchin, G.A., et al., *A short note on Egyptian blue.* Journal of Cultural Heritage, 2004. **5**(1): p. 129-133.

60. Berke, H., *Chemistry in ancient times: the development of blue and purple pigments.* Angewandte Chemie International Edition, 2002. **41**(14): p. 2483-2487.

61. Chen, Y., et al., *Structure and properties of Egyptian blue monolayer family: XCuSi4O10 (X= Ca, Sr, and Ba).* The Journal of Physical Chemistry Letters, 2016. **7**(3): p. 399-405.

62. Pozza, G., et al., *Photoluminescence of the inorganic pigments Egyptian blue, Han blue and Han purple.* Journal of Cultural Heritage, 2000. **1**(4): p. 393-398.

63. Jaksch, H., et al., *Egyptian blue—Cuprorivaite a window to ancient Egyptian technology.* Naturwissenschaften, 1983. **70**(11): p. 525-535.

64. Bugaris, D.E. and H.C. zur Loye, *Materials discovery by flux crystal growth: quaternary and higher order oxides.* Angewandte chemie international edition, 2012. **51**(16): p. 3780-3811.

65. Yan, J.-Q., *Flux growth utilizing the reaction between flux and crucible.* Journal of Crystal Growth, 2015. **416**: p. 62-65.

66. Kolahalam, L.A., et al., *Review on nanomaterials: Synthesis and applications.* Materials Today: Proceedings, 2019. **18**: p. 2182-2190.

67. Ealia, S.A.M. and M. Saravanakumar. *A review on the classification, characterisation, synthesis of nanoparticles and their application*. in *IOP Conference Series: Materials Science and Engineering*. 2017. IOP Publishing.

68. Jamkhande, P.G., et al., *Metal nanoparticles synthesis: An overview on methods of preparation, advantages and disadvantages, and applications.* Journal of drug delivery science and technology, 2019. **53**: p. 101174.

69. Bhumkar, D.R., et al., *Chitosan reduced gold nanoparticles as novel carriers for transmucosal delivery of insulin.* Pharmaceutical research, 2007. **24**(8): p. 1415-1426.

70. AshaRani, P., et al., *Cytotoxicity and genotoxicity of silver nanoparticles in human cells.* ACS nano, 2009. **3**(2): p. 279-290.

71. Wang, Y., et al., *Synthesis and optical properties of Mn-doped Ba3Al2O6 intense blue oxides.* Optical Materials, 2020. **109**: p. 110327.

72. Zhou, Y., et al., *Synthesis and properties of novel turquoise-green pigments based on BaAl2-xMnxO4+ y.* Dyes and Pigments, 2018. **155**: p. 212-217.

73. Giménez, J., et al., *Effect of NaCl on the fabrication of the Egyptian blue pigment.* Journal of Archaeological Science: Reports, 2017. **14**: p. 174-180.

74. Nenna, M. and P. Nicholson, *Faience technology.* WORKING IN MEMPHIS, 2013: p. 133.

75. Brill, R.H., *Ancient glass.* Scientific American, 1963. **209**(5): p. 120-131.

76. Ragai, J., *Snapshots of chemical practices in Ancient Egypt.* Substantia, 2018. **2**(1): p. 93-101.

77. Ragai, J., *Colour: its significance and production in Ancient Egypt.* Endeavour, 1986. **10**(2): p. 74-79.

78. Wendrich, W., *UCLA Encyclopedia of Egyptology*. 2008: UCLA, Department of Near Eastern Languages and Cultures.

79. Welc, F., *Faience Workshop in Ptolemaic Athribis (Tell Atrib) in the Nile Delta. Archaeological Evidence.* Études et travaux, 2013. **26**: p. 719.

CHAPTER 2

SYNTHESIS, NANOSTRUCTURING, AND CHARACTERIZATION OF MANGANESE BLUE PIGMENT

Introduction

Near-infrared biomedical imaging

Biomedical imaging plays a vital role nowadays, especially in the early detection and diagnosis of diseases like cancer. There are several imaging modalities available on the market such as X-ray radiography, computed tomography (CT), magnetic resonance imaging (MRI), ultrasound (US), positron emission tomography (PET), single photon emission computed tomography (SPECT) and fluorescence imaging.[2] Unfortunately, tomographic imaging modalities such as CT, PET, and SPECT use hazardous ionizing radiation, while MRI and PET intrinsically have limited spatial resolution. In contrast, fluorescence imaging does not suffer from the aforementioned drawbacks but instead provides benefits such as real-time image acquisition and spatial resolution in living organisms by the interaction of non-hazardous optical radiation, such as ultraviolet radiation, visible light, and infrared radiation with cells and tissues.[3] Fluorescence imaging in the visible range (400 – 700 nm) is not effective due to the poor photon penetration depth in most mammalian tissues, which compromises resolution and contrast due to scattering and/or absorption by biological tissue coupled with tissue autofluorescence.[4, 5] Therefore, fluorescence imaging has been expanded to longer wavelength such as the near-infrared region

(~700 – 1700 nm). Imaging in the near infrared window offers a deeper tissue penetration depth with an improved signal-to-background ratio due to reduced photon scattering, absorption, and tissue autofluorescence. Near-infrared biomedical imaging includes a NIR-I window (~700 – 900 nm), in which body tissue autofluorescence produces substantial background noise and is limited to tissue penetration depth of 1-2 cm.[6-8] To overcome the disadvantages of imaging in the NIR-I window, deep tissue imaging up to ~4 cm[8, 9] has been achieved in the NIR-II window (1000 – 1700 nm), in which there is minimal tissue autofluorescence and scattering, leading to higher imaging resolution.[10]

Nanoparticles for biomedical imaging

Unlike small-molecule contrast agents that are restricted by non-specific distribution, rapid clearance rate and enhanced tumor accumulation due to the enhanced permeability and retention (EPR) effect of tumor.[11, 12] Nanoparticles used as contrast agents offer many advantages such as their potent capacity of being functionalized with biomolecules such as siRNA, peptides or they can be loaded with drugs such as anticancer drug.[13, 14] For example, Liu et al. synthesized NaYF4:Yb^{3+},Er^{3+}@$NaGdF_4$ up conversion nanoparticles where they deposited a silica coating and functionalized it with Cys5 labelled peptide for detection of cancer.[15] They can also be used as a multimodal imaging modalities or in image guided therapy.[16] Gurunathan et al. synthesized hollow mesoporous silica nanoparticles that were loaded with both chemotherapeutic and photothermal agents for image guided therapy.[17] Persistent luminescent near-infrared nanoparticles have additional advantages compared with molecular probes, such as they are not subject to non-specific protein binding, therefore, their optical properties are not affected. In addition, their luminescent properties are not affected by solvent polarity, ionic strength, pH, and temperature.[1]

Manganese-based near-infrared luminescent materials

There are several examples of Mn^{2+}, Mn^{4+}, Mn^{5+}, or Mn^{6+}-based near-infrared luminescent materials that exist in the literature. Law et al. have reported the synthesis and characterization of Mn^{2+}:ZnS quantum dots as a bimodal imaging probe for near-infrared imaging and MRI contrast. Using transmission electron microscopy (TEM), they were able to estimate the particle size as 3.3 nm. When excited at ~630 nm, these nanoparticles emit at ~791 nm.[19] A near-infrared phosphor, $RbZnF_3:Yb^{3+}$, Mn^{2+} has been reported by Han et al. with emission centered at ~780 nm. Using density functional theory calculations and extended X-ray absorption fine structure, these researchers were able to confirm that the luminescence is due to Mn^{2+} resulting from the Mn^{2+} – Mn^{2+} dimer induced by Mn^{2+} aggregation in $RbZnF_3$.[20]

Mn^{4+} has an ionic radius similar to Al^{3+}, Si^{4+}, Ti^{4+}, and Ge^{4+} in octahedral sites, therefore and a number of publications report near infrared luminescence via Mn^{4+} doping.[21] As an example, Du et al. described near-infrared luminescent perovskite-type solid solutions $LaAl_{1-x}Ga_xO_3$ and $La_{1-x}Gd_xAlO_3$ doped with Mn^{4+}.[22] In this study, they tailored the emission and afterglow via crystal field control and composition modification, and they tracked changes originating from the $^2E_g \longrightarrow {}^4A_{2g}$ emission of Mn^{4+} using photoluminescence measurements. Li et al. reported a Mn^{4+}/Yb^{3+} co-doped La_2MgTiO_6 near-infrared phosphor which can convert short wavelength light (250 – 550 nm) into near-infrared emission at 990 nm.[23]

A $Ba_3(PO_4)_2:Mn^{5+}$ phosphor with a broad excitation range of 200 – 900 nm and narrow emission peak at ~1191 nm has been reported by Cao et al.[24] The authors found that the optimal doping concentration was ~1 mol% Mn^{5+}, with a fluorescence lifetime of ~550 μs. Similarly, Zhang et al. synthesized Mn^{5+} doped $Ba_3(MO_4)_2$ (M= V or P) nanoparticles for luminescence imaging in the NIR-II window (~1190 nm).[25]

Brunold et al. reported the near-infrared emission from Mn^{6+} doped in K_2SO_4, K_2CrO_4, K_2SeO_4, and $BaSO_4$ at 10 K, but unfortunately, the luminescence was quenched with increasing temperature in all cases except $BaSO_4$. This work demonstrated that Mn^{6+} -doped $BaSO_4$ displays luminescence at room temperature with an absorption at 625 nm and an emission centered at 1075 nm.[26, 27]

Manganese blue pigment

Manganese blue pigment is a green-blue colored pigment with manganese content ranging from 2.5-3.5% and barium sulfate content ranging from 80-85%.[28] While it was being produced industrially, manganese blue was employed as cement whitener and an artist's pigment. Synthesis of the pigment has been reported in the patent literature around 1935 by a German company, I.G. Farbenindustrie. The patent described the synthesis of the pigment as a melt flux approach in which barium nitrate which also acts as an oxidizing agent along with the addition of a basic substance such as barium oxide, barium nitrate, and barium hydroxide. Different sources of manganese have been described in the patent, for example, $Mn(NO_3)_2$, $kMnO_4$, K_2MnO_4, and $BaMnO_4$. Bulk barium sulfate can be used for the synthesis, or it can be synthesized in-situ using a source of barium such as barium nitrate or barium hydroxide and sodium sulfate.[1] Manganese blue has been reported to have superior stability and is resistant to light, acids, and alkali.[29] It has been described as a barium manganate(V) sulfate, in which manganese in a 5+ oxidation state is incorporated in the barium sulfate matrix by replacing S^{6+}.[30] Therefore, the pigment particles is a solid solution of $BaSO_4$ and $Ba_3(MnO4)_2$ as a result of the substitution of sulfur by manganese. Incorporation of manganese in the barium sulfate matrix imparts the pigment properties such as its unique green-blue color and near-infrared luminescence. In 2014 Accorsi et al. conduced photoluminescence

measurements on manganese blue where they found that the pigment exhibits a broad absorption band (600 – 1200 nm) and its emission is centered at ~1300 nm. The pigment exhibits near-infrared luminescent properties with emission centered at ~1300 nm,[31] which potentially can be exploited for applications like NIR luminescence biomedical imaging specifically in the NIR-II window.

An additional advantageous aspect of manganese blue is the barium sulfate matrix. Barium sulfate is a well-established X-ray contrast agent in the medical field and has well-known biocompatibility, low water solubility, and high clearance rate.[32] In general, inorganic nanoparticles have advantages including low toxicity, hydrophilicity, biocompatibility, and high stability.[33] The nanostructuring of manganese blue can lead to dual mode contrast for near-infrared luminescence imaging and micro-CT.

To develop a procedure for the synthesis of manganese blue nanoparticles, the synthesis of bulk manganese blue particles must be fully understood. The nature and the of manganese incorporated in the barium sulfate host must be investigated. The post-synthetic acid treatment is a challenging aspect that must be finessed. There are very few reports in the literature for the synthesis of manganese blue via a melt flux synthesis method followed by a post-synthetic acid treatment of the pigment to remove unwanted manganese products.[1] So far, there are no experimental procedures detailing the synthesis of the pigment. Although the patent literature mentions multiple synthetic procedures for the pigments, but the synthesis temperature is not clearly defined, and the specific source of manganese used is not highlighted. They also describe post-synthetic acid treatment using dilute hydrochloric acid solution which when used is detrimental to the pigment.

In this work, we demonstrate the preparation and purification of bulk manganese blue pigment and a nanoparticulate form stability of manganese blue pigment against heat and light of

this material. Composition, structure, morphology, and NIR luminescence is confirmed for both products. Furthermore, we deposit a thin layer of silica on the nanoparticles to aid with stability and chemical functionalization. Centrifugation protocols after silica coating allowed us to size-select the nanoparticles to yield a controllable and narrow size distribution.

Material Preparation and Characterization

Materials: barium sulfate (Sigma Aldrich, 99.99% trace element basis) or 1.10 g (4.71 mmol) barium sulfate nanoparticles were synthesized according to the procedure reported by Zhang et al., [34] manganese(IV) oxide (Sigma Aldrich, 99.99% trace metals basis) or amorphous manganese(IV) oxide particles were prepared according to the procedure reported by Ragupathy et al.,[35] barium nitrate (Sigma Aldrich, 99.99% trace metals basis), sodium nitrite (J.T. Baker Chemical Company, ≥ 97.0%), hydrochloric acid (Sigma Aldrich, ACS reagent, 37%), oxalic acid (Sigma Aldrich, ≥ 99%) solution, RU^{TM} sodium silicate solution [$Na_2O(SiO_2)_x(H_2O)_x$] (Sigma Aldrich, reagent grade purity, 26.5% SiO_2), LUDOX SM colloidal silica (Sigma Aldrich, 30 wt. % suspended in H_2O). A commercial obtained manganese blue pigment sample (old stock manufactured pre-1990) was obtained from Kremer Pigmente.

Melt flux synthesis of bulk manganese blue bulk: manganese blue pigment bulk particles were synthesized according to the method developed by Mr. Roman Beauclerc. 5.50 g (23.6 mmol) barium sulfate, 0.355 g (4.08 mmol) manganese(IV) oxide or manganese oxide particles, and 9.31 g (35.6 mmol) barium nitrate for synthesis of nanoparticles were ground in an agate mortar and pestle until a dull grey homogeneous powder is produced. Then the reactants were transferred to a

50 mL nickel crucible and fired in a small box furnace using a ramp rate of 5 °C/min to 710 °C for two hours for the bulk synthesis The reaction was left to cool down naturally to room temperature and then the sintered frit is removed and transferred to a beaker for purification. Post-synthetic acid treatment was conducted according to the method developed by Mr. Roman Beauclerc. 0.80 g (11.6 mmol) sodium nitrite were added to 30.0 g of 6.0 M (164 mmol) hydrochloric acid, and the resultant acid solution was poured over the reactant frit and stirred using a Teflon magnetic stirrer for one hour. This was followed by washing with 25.0 g of 3% sodium nitrite solution followed by washing with 75 mL of 1% oxalic acid solution. The product was then decanted and dried in a vacuum oven at ~50 °C for 12 h. Calculation of the percentage yield is based on the melt flux synthesis. The mass isolated is 4.04 g of pigment and the percentage yield is 25.8%

Melt flux synthesis of manganese blue nanoparticles: 1.10 g (4.71 mmol) barium sulfate nanoparticles, or 0.0700 g (0.805 mmol) amorphous manganese oxide particles, and 1.86 g (7.12 mmol) barium nitrate for synthesis of nanoparticles were ground in an agate mortar and pestle until a dull grey homogeneous powder is produced. Then the reactants were transferred to a 50 mL nickel crucible and fired in a small box furnace using a ramp rate of 5 °C/min to 520 °C for three hours. The reaction was left to cool down naturally to room temperature and then the sintered frit is removed and transferred to a beaker for purification. Post-synthetic acid treatment was conducted according to the method developed by Mr. Roman Beauclerc. 0.80 g (11.6 mmol) sodium nitrite were added to 30.0 g of 6.0 M (164 mmol) hydrochloric acid, and the resultant acid solution was poured over the powder reactant and stirred using a Teflon magnetic stirrer for one hour. This was followed by washing with 25.0 g of 3% sodium nitrite solution followed by washing with 75 mL of 1% oxalic acid solution. The product was or centrifuged and dried in a vacuum

oven at ~50 °C for 12 h. Calculation of the percentage yield is based on the melt flux synthesis. The mass isolated was 0.805 g of pigment and the percentage yield is 65.9%.

Silica coating of manganese blue nanoparticles: The pigment nanoparticles were coated with a layer of amorphous silica according to the method described by Abe et al.[36] For coating of the pigment nanoparticles with a layer of amorphous silica, 0.282 g of acid treated nanoparticles were dispersed in 2.37 mL of deionized water. The pH of the solution is brought to a pH in the range of 9.0 – 10.0 using RU^{TM} sodium silicate solution [$Na_2O(SiO_2)_x(H_2O)_x$]. This is followed by simultaneously adding 1.41 g of 4.83 wt% LUDOX SM colloidal silica using a KD scientific KDS210 infuse/withdraw syringe pump at a rate of 0.008 mL/min and 1.33 g of 2.74 wt. % oxalic acid added at also at a rate of 0.008 mL/min while monitoring the pH in the range of 9.8 – 10.0. After the colloidal silica and the oxalic acid were added, the pH of the solution was allowed to stand at a pH of 7.0. The slurry was washed with water and decanted to remove all the sodium salt followed by filtering and drying in a vacuum oven at ~50 °C for 12 hours. The percentage yield is 83.9%.

Visible-induced luminescence imaging: Manganese blue bulk pigment and nanoparticles samples were illuminated with a red LED light array (LEDLB-24-RED/BLUE-F-BLACK, 72 Watts–- 9~42 VDC, Larson Electronics LLC) and imaged using a Xenics Bobcat 320-GigE Vision 100 Hz camera (0.9 to 1.7 μm imaging range). Images were post-processed using Adobe Photoshop CC 2022; specifically, the dimensions of the images were adjusted to a width of 1500 and then cropped, and the luminescence was false-colored for clarity.

SEM/EDS: Products were characterized using a Thermo Fisher Scientific (FEI) field-emission SEM Teneo microscope, operating at 10 keV and using a spot size of 10. Energy-dispersive spectroscopy (EDS) data were collected with an integrated Oxford Instruments X-MAX^N detector operated at 10 keV. The powder samples were sputter coated with a ~200 Å layer of carbon.

Powder X-ray diffraction (PXRD): Powder X-ray diffraction (PXRD) was conducted on the powder sample using a Bruker D8 instrument with a Co-Kα X-ray source ($\boldsymbol{\lambda} = 1.78890$ Å) operated at 35 kV and 40 mA. The data were collected from 10 to 80° 2θ at a scan rate of 0.1 s/step. OriginPro 8.5 was used for peak fitting (Gaussian type) and to determine FWHM. The Scherrer equation was used to determine the crystallite size.

SE/EDS: Scanning electron microscopy imaging was conducted using a Hitachi SU9000EA microscope with an accelerating voltage of 30 kV and spot size of 5 μA. The samples were dispersed in ~20 mL isopropyl alcohol and drop-cast on Ted Pella TEM lacey grids. Energy-dispersive spectroscopy (EDS) data were collected with an integrated Oxford Large Area Windowless Energy Dispersive Spectroscopy.

Optical microscopy: Samples were examined using a Leica DVM6 digital microscope with a 3664 x 2748-pixel camera using a low magnification objective (190x magnification). Illumination source was a ring light LED array. Z-stacking was used for some of the samples.

Thermogravimetric analysis (TGA): was carried out using a Perkin Elmer TGA 8000™ Thermogravimetric analyzer. Analysis of the bulk pigment was conducted in air from 30-1000 °C at a rate of 10 °C/min.

Raman Analysis: Analysis on the bulk sample was conducted using Thermo Scientific DXR Raman microscope (10x magnification, 532 nm irradiation, laser power of 10 mW).

Particle size analysis: analysis was conducted using ImageJ and Origin Pro software.

X-ray Photoelectron Spectroscopy (XPS): was conducted using Physical Electronics PHI VersaProbe III Scanning ESCA Microprobe (XPS) with a scanning monochromatic X-ray source. The data was collected at a 90° angle with a 30 second etch and 60 sweeps. OriginPro 8.5 software was used for peak fitting (Gaussian type) and further data analysis.

Results and Discussion

Melt flux synthesis of manganese blue using different manganese sources

The preparation of manganese blue begins from three reactants: (1) barium sulfate, which becomes the matrix for manganese ions, (2) a manganese source, such as manganese(IV) oxide, and (3) barium nitrate, which acts as a flux and an additional source of barium and oxygen in the reaction. The melting point of barium nitrate is ~592 °C, past which it can form a molten solution with the other components to enable the incorporation of manganese ions. This is followed by recrystallisation to allow the manganese-doped barium sulfate particles to grow from the flux.

Additionally, barium nitrate is a strong oxidizing agent,[37] which is important for the incorporation of the correct oxidation state of manganese in the barium sulfate matrix. According to Reinen et al., manganese present in a 5+ oxidation state and tetrahedrally coordinated to four oxygens is responsible for the green-blue color of the pigment.[30] In addition, related systems like $BaAl_{2-x}Mn_xO_{4+y}$ and $Ba_3Al_{2-x}Mn_xO_{6+y}$, display colors ranging from turquoise to sky or ocean blue as a result of incorporation of Mn^{5+} in $BaAl_2O_4$ or $Ba_3Al_2O_6$ respectively but the authors did not report any luminescent properties.[38, 39] In our experiments, we examined several manganese sources, such as $KMnO_4$ in which manganese exists as a 7+ oxidation state, K_2MnO_4 in which manganese exists as a 6+ oxidation state, and $BaMnO_4$ in which manganese also exists as a 6+ oxidation state. All flux reactions were conducted at 720 °C for 1 h. The resultant product from these manganese sources always acquired a dark green color. As mentioned in the patent literature, if manganese is not correctly incorporated in barium sulfate, green or brown colors are produced[1] due to oxidation states other than 5+. For instance, $KMnO_4$ starts decomposing at a temperature of ~250 °C, giving K_2MnO_4, MnO_2, and O_2.[40] As the temperature increases beyond 250 °C to ~590 °C (the temperature at which barium nitrate melts), K_2MnO_4 decomposes to K_3MnO_4 and $K_4Mn_7O_{16}$.[41] We hypothesize that such transformations caused the incorporation of manganese in undesirable or even multiple oxidation states in our products.

The temperature of manganese blue preparation is also very important. As previously mentioned, manganese blue is a solid solution of $BaSO_4$ and $Ba_3(MnO_4)_2$ and it has been reported that systems similar to $Ba_3(MnO_4)_2$ such as $Ba(MnO_4)_2$ decompose at a temperature beyond 800 °C to produce other barium manganese compounds.[42] Experimentally, we have attempted temperatures up to 750 °C and we noticed that it was detrimental to the pigment as it altered the morphology of the pigment and produced unwanted barium manganate products.

Post-synthetic acid treatment using 1M HCl and 1M $NaHSO_3$ solutions

The purification of manganese blue has been a challenging aspect of this project. The literature mentions that, to remove unwanted manganese byproducts and thereby reveal the true and desirable green blue color of the pigment, the raw product should be treated with a dilute acid solution, such as hydrochloric acid in combination with sodium bisulfite, nitric acid, or sulfuric acid.[1] In addition to the low incorporation of manganese as a result of the reaction, the use of dilute hydrochloric acid in a concentration range of 0.1 – 1 M resulted in a light blue product that does not match the color saturation of the pigment. Furthermore, the manganese content was far lower compared to that in a commercial manganese blue sample due to the low incorporation of manganese resulting from the synthesis and the post-synthetic acid treatment. Figure 2.1a-c shows optical images of the raw product from attempts to prepare manganese blue using $KMnO_4$ as a manganese source (a) showing the green color before purification with hydrochloric acid and sodium bisulfite, the post-synthetic acid treatment pigment after purification using 1 M HCl and 1 M sodium bisulfite (b) showing a light blue color, a comparison between the reaction and manganese blue pigment using optical imaging (c) and PXRD (d). Because barium sulfate is the host material, the PXRD patterns for both the reaction and the commercial pigment match the barium sulfate reference pattern (ICDD 04-006-2788). From SEM images (Figure 2.2), we noticed a difference in particle morphology between the product derived from reaction with $KMnO_4$ and the commercial pigment. The commercial pigment particles had a distinct rounded morphology with a flat top and bottom while the crystals synthesized using $KMnO_4$ have an elongated multifaceted morphology. From the elemental composition of the sample synthesized using $KMnO_4$, specifically the composition of manganese in atomic percent in the pigment is very low

again in comparison to the commercial pigment. As a confirmation, from the elemental composition for the reaction using $KMnO_4$, the atomic percentage of sulfur is higher than in the commercial pigment as manganese replaces sulfur in the barium sulfate matrix. We also noticed at some instances that the surface of barium sulfate crystals was etched which might also have contributed to the low manganese content in the synthesized crystals.

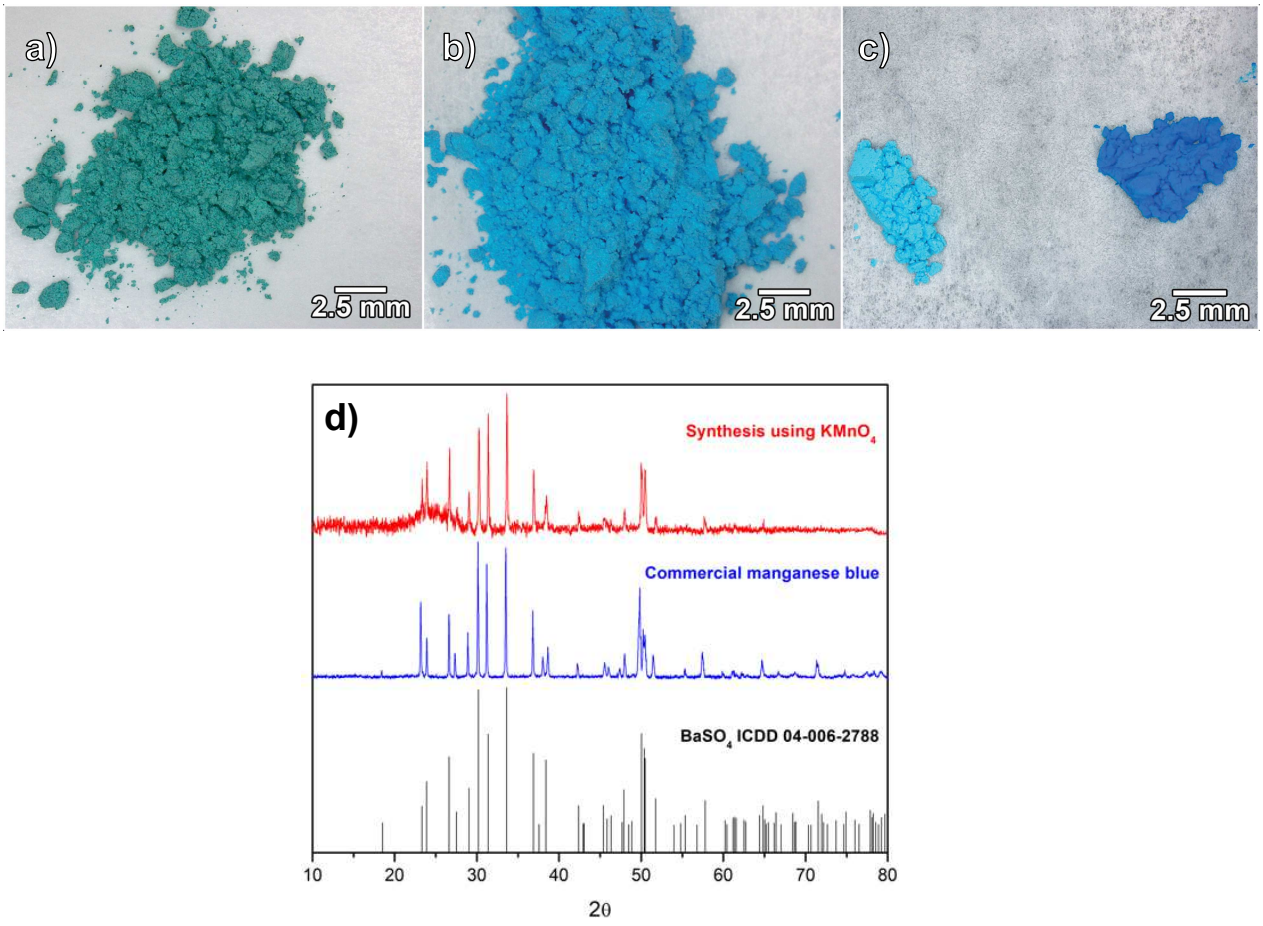

Figure 2.1: An attempt to synthesize manganese blue using $KMnO_4$ as a manganese source[1]: a) pre-acid treatment, b) post-synthetic acid treatment using 1M HCl and 1M $NaHSO_3$, c) comparison with commercial manganese blue sample showing the difference in color between the two samples, and d) PXRD comparison between the manganese blue products using $KMnO_4$ and the commercial manganese blue pigment.

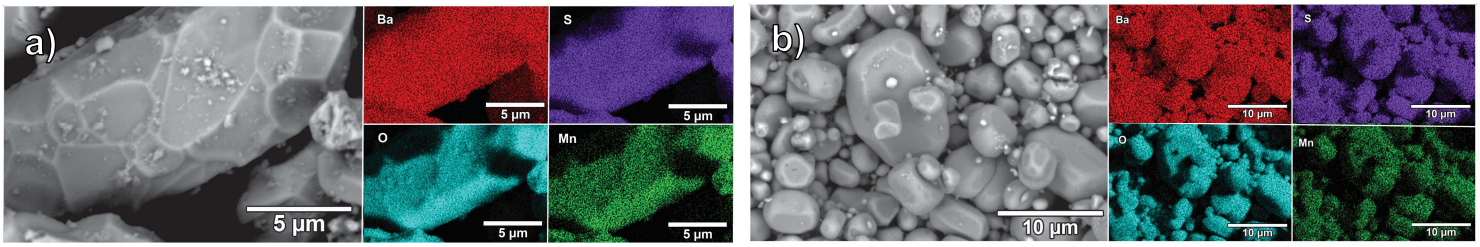

Element	Ba	S	O	Mn
At%	25.1	17.0	57.1	0.1

Elemen	Ba	S	O	Mn
At%	24.9	13.1	59.6	1.9

Figure 2.2: SEM, elemental maps, and elemental composition of a) manganese blue synthesis using $KMnO_4$ as a manganese source (post-synthetic acid treatment) and b) manganese blue commercial pigment.

Melt flux synthesis of Manganese blue using manganese(IV) oxide

Using MnO_2 as a source of manganese in bulk barium sulfate provided drastically different results. MnO_2 decomposes at a temperature of ~500 °C to give trivalent Mn_2O_3.[43] This temperature is also relatively close to the decomposition of barium nitrate versus the other manganese sources. Also, because barium nitrate is an oxidizing agent, it can oxidize the 3+ or 4+ oxidation states of manganese to in the 5+ oxidation state, imparting the green-blue color to the pigment. The reaction was fired at 710 °C for one or two hours.

Pigment purification by post-synthetic acid treatment using nitrous acid and oxalic acid

The acid treatment of the raw pigment first with dilute hydrochloric acid following with 0.1 M sodium bisulfite appeared to be overly harsh, as evidenced by color difference between the synthesized and the commercial samples. As an alternative, sodium nitrite dissolved in 6.0 M HCl(aq) creates a nitrous acid solution in-situ, which is a weak acid and therefore not as harsh as dilute HCl(aq), a stronger acid. The use of nitrous acid allows unwanted manganese compounds to be dissolved, and additional washing with aqueous oxalic acid is helpful because it acts as a

reducing agent and produces barium oxalate along with other soluble salts. These solutions can be decanted from the product particles to isolate the pure pigment. After drying the overall yield is 25.6%. The low yield could be attributed to decantation. To raise the yield, centrifugation or filtration can be used over decantation.

Optical microscope and SEM images of melt flux synthesized manganese blue pigment using MnO_2 after firing one or two hours are shown below in Figure 2.3. From the optical images, we observed that the sample fired for one hours is lighter in color in comparison to the commercial pigment and the sample fired for two hours. SEM images show that the sample fired for one hour has a broader crystal size distribution in comparison to the commercial sample and the sample fired for two hours. By firing the reaction for a longer period (two hours) we obtained a narrower crystal size distribution compared to the one-hour sample. It is likely that the intensity of the color increases with an increase in the crystal size.

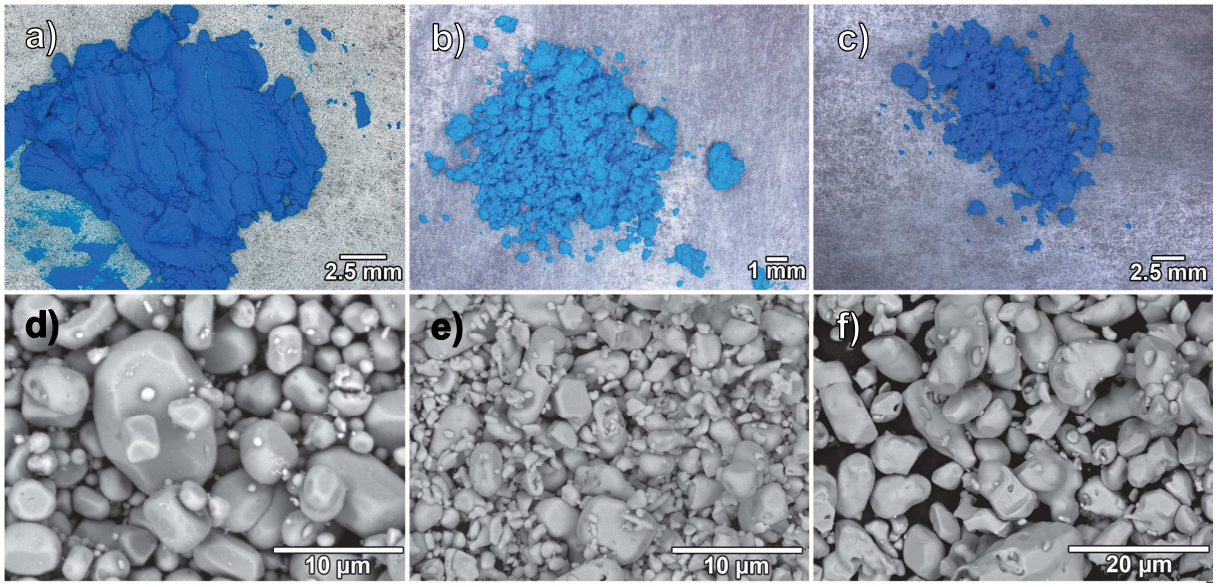

Figure 2.3: Optical microscope images of a) commercial manganese blue, b) lab synthesized manganese blue using the melt flux route (1h), and c) lab synthesized manganese blue using the melt flux route (2h) fired at the same temperature as product (b). The corresponding SEM images d-f are shown below the optical microscope images.

PXRD analysis and comparison (Figure 2.4) reveals that the synthesized sample's pattern matches barium sulfate, which is consistent with the low doping levels of manganese that do not significantly distort or modify the barium sulfate matrix.

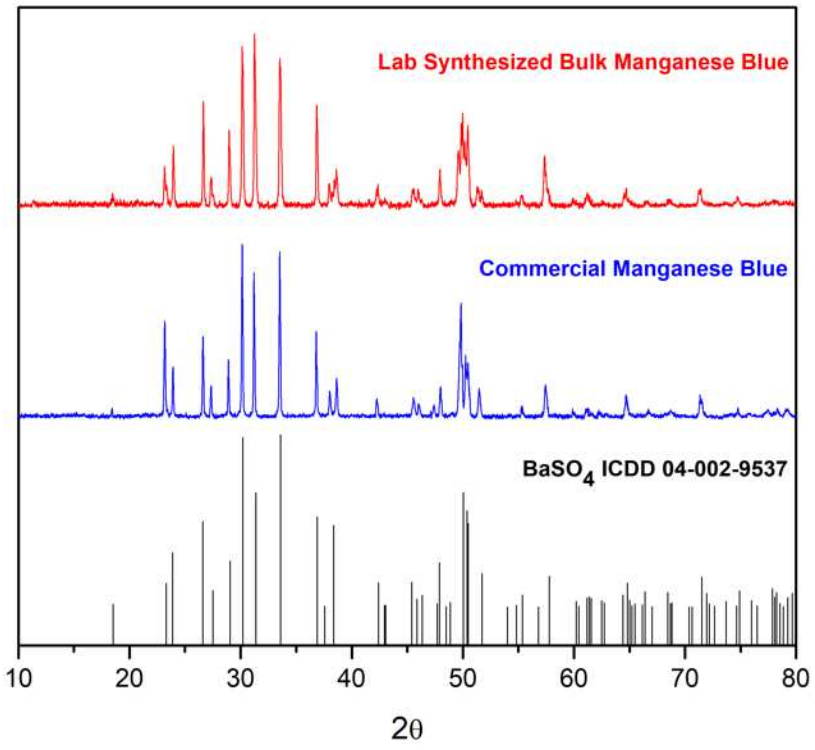

Figure 2.4: PXRD patterns of melt flux synthesized manganese blue pigment using MnO_2 as a manganese source fired for 1h and a commercially obtained manganese blue pigment.

Examining the elemental data for the products fired at one and two hours (Figure 2.5), we find that the atomic percentage of manganese is higher in the reaction fired for one hour. The manganese content in the one-hour sample (Figure 2.5 (a)) is very similar to the manganese content in the commercial pigment (~1.9 At%). We have noticed that in the commercial sample, that the crystals with smaller size have a higher manganese content than the larger crystals and this might explain

why the sample fired for two hours has a lower manganese content due to the more uniform and larger crystal size (Figure 2.5 (b)).

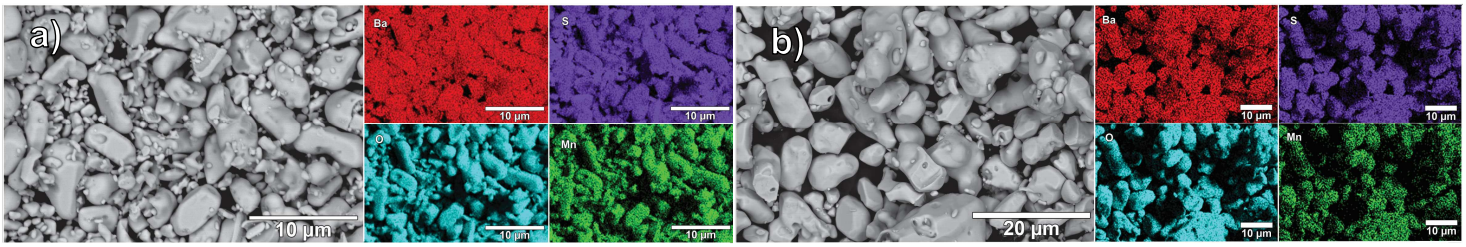

Element	Ba	S	O	Mn
At%	21.4	14.2	61.9	2.3

Element	Ba	S	O	Mn
At%	25.0	15.8	57.9	1.0

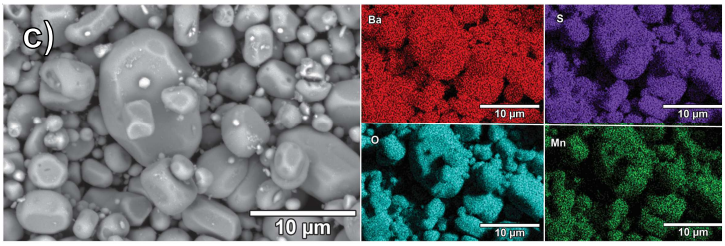

Element	Ba	S	O	Mn
At%	24.9	13.1	59.6	1.9

Figure 2.5: SEM, elemental maps, and elemental atomic % of manganese blue a) lab synthesized sample for one hour, b) lab synthesized sample for two hours, and c) commercial pigment.

We also evaluated "granulation power" of our bulk pigments compared to commercial manganese blue samples, in both powder form (simply dispersed in water) and formulated with a binder as a watercolor paint. The granulation power of a pigment is the ability of larger particles to settle in certain regions of the substrate, forming a unique texture of mottled color. Granulation is a pigment characteristic desirable by artists for aesthetic purposes that is especially relevant for watercolor paints. We can see from Figure 2.6 that the lab-synthesized manganese blue displays

the least granulation compared to the other two samples, which we can attribute to its more uniform particle size.

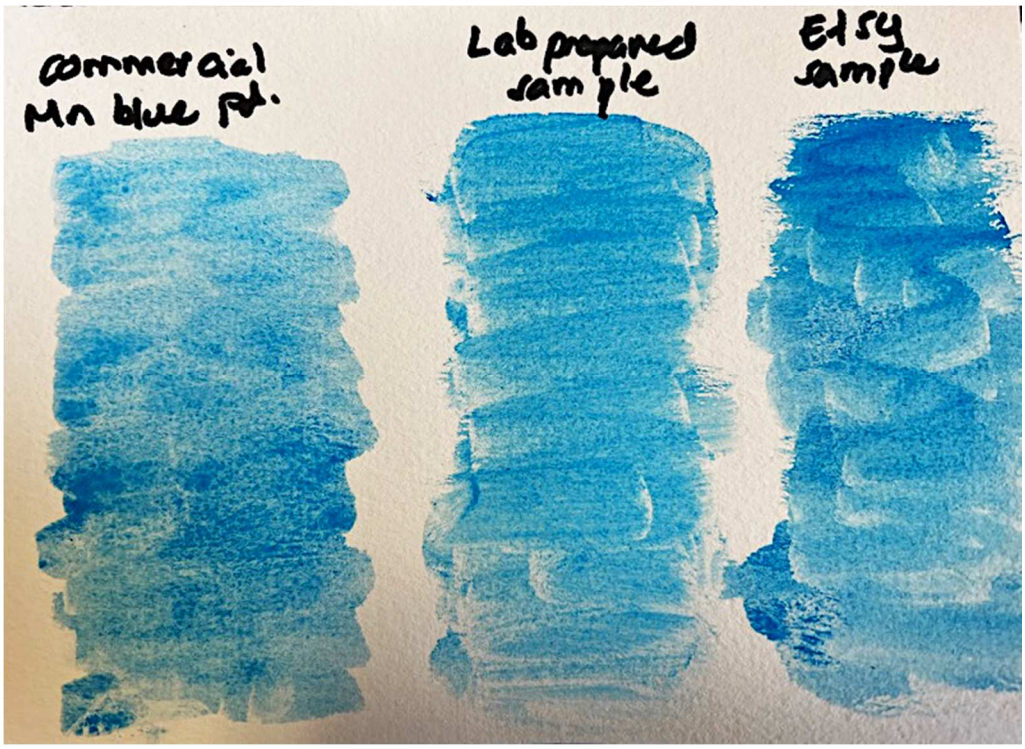

Figure 2.6: Granulation power test for the manganese blue bulk pigment synthesized for two hours (middle) compared to commercial manganese blue powder sample (left) and another commercial manganese blue pigment sample dispersed in binder. The manganese blue pigment displays the least granulation due to its uniform particle size.

The stability of manganese blue is a critical aspect for its use as a pigment or for biomedical imaging. Although the literature mentions that this pigment is remarkably thermally and chemically stable and lightfast, no reports have included data. Therefore, we conducted thermogravimetric analysis on the 2-hour lab synthesized manganese blue bulk pigment particles. From the TGA curve in Figure 2.7 (a), we noticed four transitions at ~175 °C, 200 °C, 500 °C, and 600 °C and an overall 7 wt% mass loss from room temperature to 1000 °C. PXRD and Raman measurements confirmed the stability of this material. From the PXRD patterns in Figure 2.7 (b),

we noticed that there was no drastic change or appearance of new peaks until 600 °C where we noticed small new peaks at ~28° and 29° 2θ. The two peaks matched manganese(II) sulfate with a space group of *Cmcm,* which is the α-$MnSO_4$ or the anhydrous polymorph.[44] From Figure 2(c), the Raman patterns at different temperature confirm that that the average crystal structure of the sample did not change, consistent with its thermal stability.

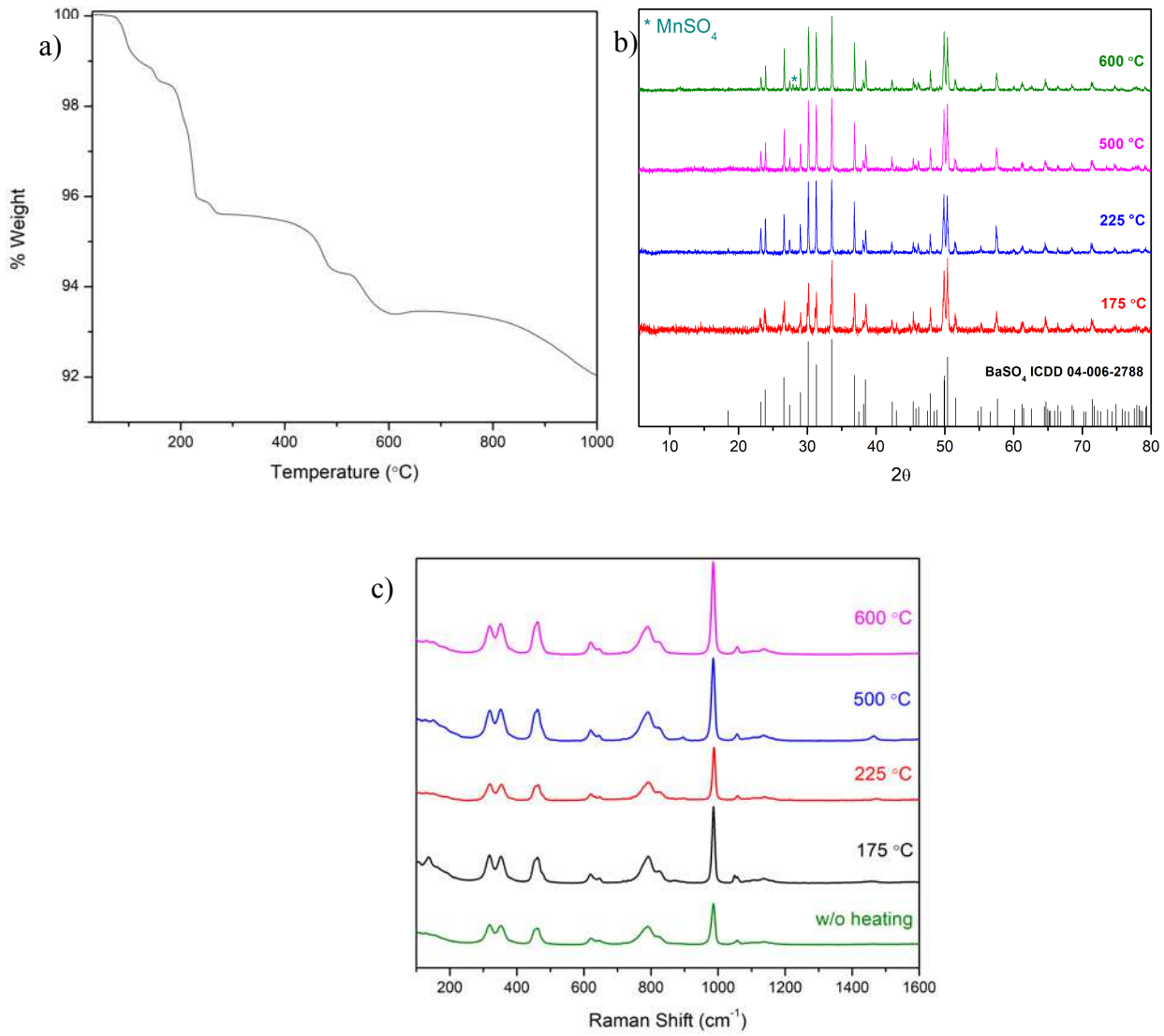

Figure 2.7: a) TGA curve of manganese blue pigment, b) PXRD patterns of manganese blue pigment heat at a temperature of 175 to 600 °C, and c) corresponding Raman spectra of the pigment heated at a temperature of 175 to 600 °C.

Finally, XPS analysis was conducted on the manganese blue pigment synthesized for one hour to confirm that the oxidation state of manganese in the pigment is a 5+ oxidation state. The reason for choosing this sample is it contains the highest amount of manganese and in order to obtain better XPS signals for manganese as there is a correlation between the signal intensity and the composition of manganese in the sample. Figure 2.8 shows the XPS spectra for Ba, S, O, and Mn. In Figure 2.8(d), there are two and they correspond to 642.8 eV and 654.2 eV respectively. Barium containing green-blue pigments containing manganese 5+ oxidation state was reported in the literature and have similar binding energies for the $2p_{3/2}$ peak to our lab synthesized sample at 642.8 eV[45] and 642.75[46] as well as the $2p_{1/2}$ at 654.4 eV which confirms the oxidation state in our pigment is a 5+ oxidation state.

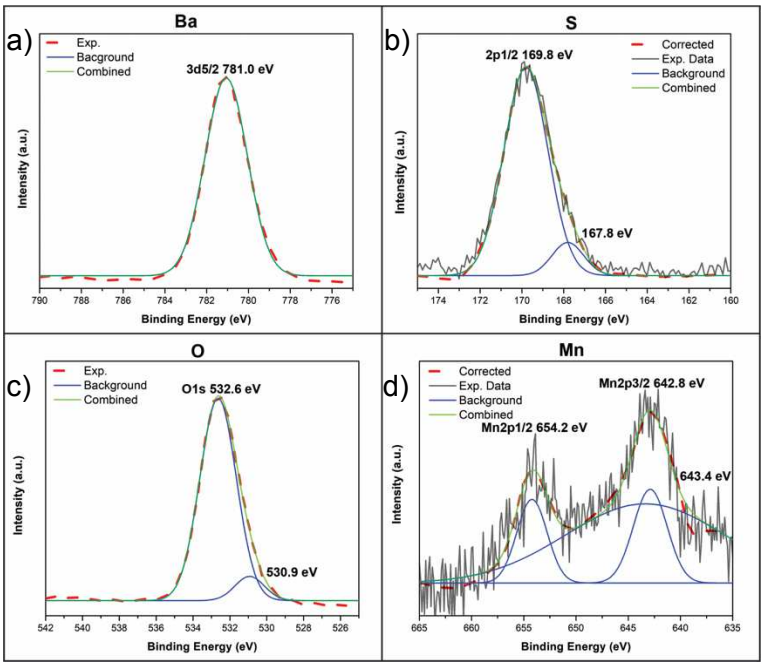

Figure 2.8: XPS analysis of the manganese blue pigment sample synthesized at for one hour. Panels a-d represent the XPS spectra of barium, sulfur, oxygen, and manganese respectively.

Nanostructuring of Manganese blue pigment

Our goal for this project is to nanostructure manganese blue for NIR biomedical imaging applications. A single published report of barium sulfate nanoparticles doped with Mn^{6+} was not reproducible in our hands, unfortunately.[34] Therefore, we modified and optimized the synthetic procedure for bulk manganese blue to yield a nanostructured product. We used barium sulfate nanoparticles synthesized using ethylene diamine tetraacetic acid (EDTA) as a capping ligand and amorphous manganese(IV) oxide nanoparticles that become crystalline when annealed at a higher temperatures. As a result of using nano precursors and due to their higher reactivity and surface area we started by reducing the reaction temperature from 710 to 650 °C while running the reaction for one hour like the bulk synthesis. By looking at the PXRD and comparing it to the bulk synthesized pigments for two hours and the commercial pigment. We did not notice any difference in terms of PXRD of the product compared with bulk samples (Figure 2.9), but we noted a change in the morphology of the crystals and a difference in the color saturation to a lighter green-blue color. In Figure 2.10(c), the pigment synthesized at 650 °C is compared to the commercially obtained manganese blue. The lighter tone is consistent with a smaller crystal size, an effect that has been reported for other pigments as well.[47]

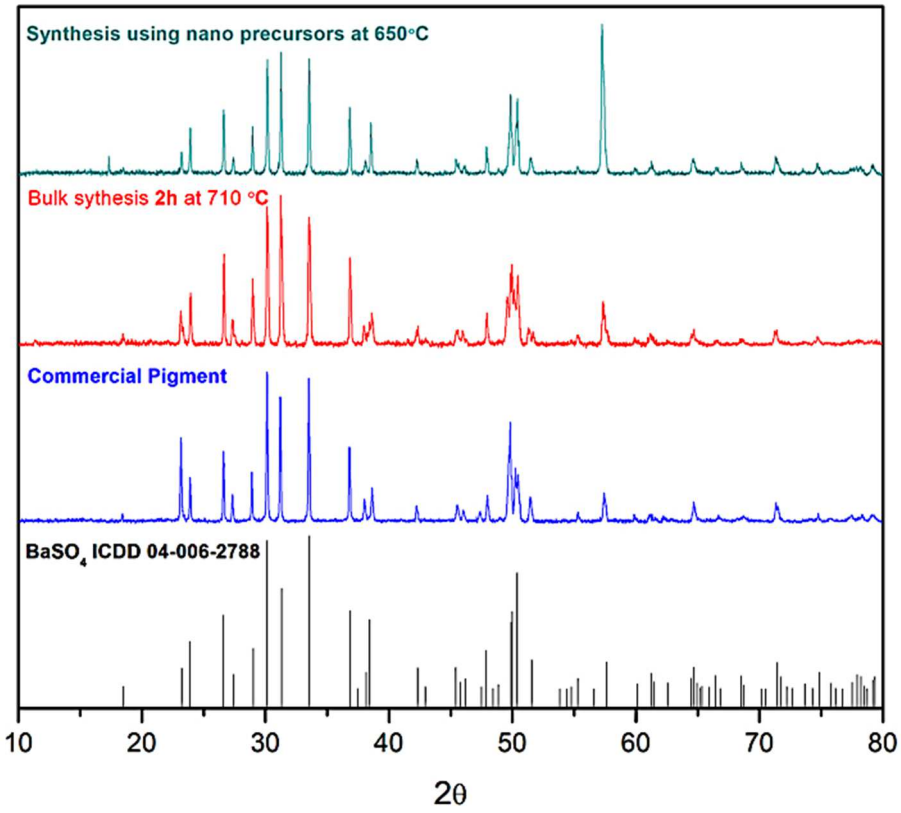

Figure 2.9: PXRD of manganese blue synthesized at 650 °C using starting nanomaterials (green pattern), bulk manganese blue synthesized at 710 °C (red pattern), and commercial pigment (blue pattern). All the patterns match barium sulfate ICDD 04-006-2788.

Figure 2.10(a) shows the morphology of the product from SEM imaging, which appear as rod-like, faceted crystals. These microrod particles are smaller in comparison to the bulk sample (synthesized at 710 °C/2 h), with dimensions ranging from 2 -10 μm long to 0.5-2 μm wide. This morphology can be explained by the presence of the capping reagent, ethylenediaminetetraacetic acid used for the synthesis of barium sulfate nanoparticles which perturbs the extension of the crystal growth in different directions, resulting in anisotropic crystal growth.[48] The ligand-oriented attachment occurs supposedly at lower temperatures as the organic ligand are burned off at higher temperatures. Elemental mapping (Figure 2.10) shows the homogeneous distribution of manganese at an incorporation level of ~1.5 At%. The results suggest a correlation between the size of the crystals and the manganese content, with the smaller microrods having greater Mn

loading compared to the larger bulk crystals (1.0 At%). NIR imaging also demonstrated that the microstructured manganese blue is strongly luminescent, as shown in Figure 2.10 (b).

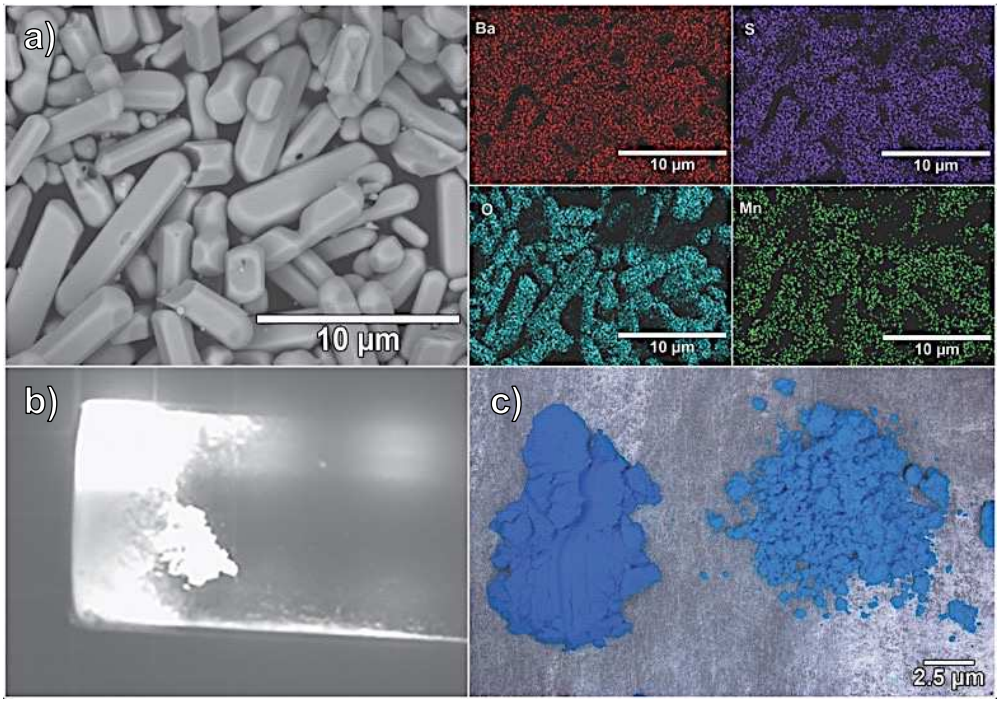

Figure 2.10: a) SEM image of manganese blue microrods synthesized at 650 °C and the corresponding elemental mapping, b) near-infrared luminescence imaging of manganese blue microrods, and c) optical microscope image of manganese blue commercial pigment (left) and manganese blue microrods synthesized at 650 °C.

Our next step toward manganese blue nanoparticles was to further lower the synthesis temperature. Lowering the reaction temperature to 550 °C while keeping the firing temperature at 2 h provided an intriguing product. From the PXRD pattern of this material (Figure 2.11), we noticed two things. First, there were certain peaks in the PXRD pattern that showed slight broadening at the base at ~30°, 31°, 33°, and 38° 2θ, Figure 2.11 (a) and (b), which suggests the presence of nanoparticles.[49] We also conducted Scherrer analysis on the aforementioned peaks and we estimated that the crystallite size is ~49.6 nm. From Figure 2.11(a), SEM imaging confirmed the presence of nanoparticles on the surface of barium nitrate. We hypothesize that the

manganese blue nanoparticles nucleate and grow from barium nitrate, as it is the flux, which solidifies upon cooling. From the EDS data, we clearly can see an overlap between barium, sulfur, and oxygen with 0.8 At% presence of manganese based on area EDS analysis.

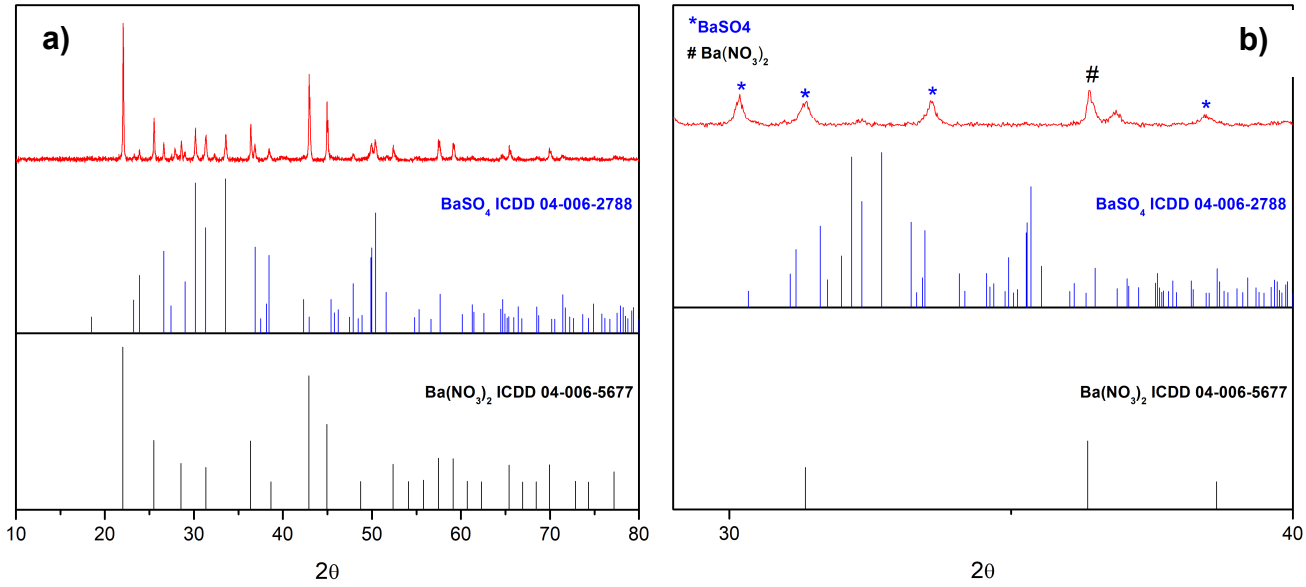

Figure 2.11: a) PXRD pattern of manganese blue synthesized from nanoscale precursors at 550 °C for 2 hours and b) a close-up of the PXRD peaks showing the peak broadening indicating the presence of manganese blue nanoparticles.

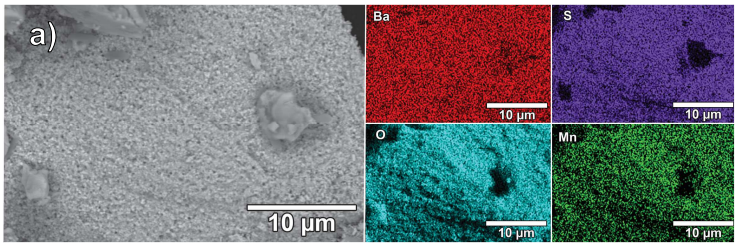

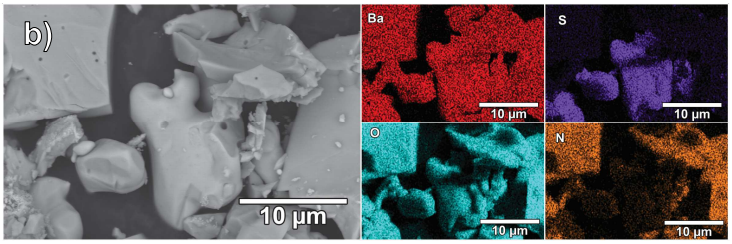

Element	Ba	S	O	Mn
At%	24.3	13.7	55.1	0.8

Element	Ba	S	O	Mn
At%	31.7	16.7	50.3	1.2

Figure 2.12: a) SEM and corresponding elemental mapping of the nanoparticle synthesis fired at 550 °C for 2h showing the presence of manganese blue nanoparticles as indicated by the overlap of Ba, S, O, and Mn, and b) sintered crystals present in the same products of the reaction fired at 550 °C.

Screening the rest of the sample synthesized at 550 °C revealed some manganese blue crystals ~10 µm in size [Figure 2.12 (b)], indicating that further reduced temperatures are needed to produce smaller crystals. Another experiment was conducted also using nanoscale precursors, but the reaction temperature was decreased from 550 to 500 °C for three hours. We noticed that the color of the powder stayed the same as the unreacted powder, therefore we observed a change in the color of the reaction. When the sample was analyzed using PXRD, the broadened peaks were still retained which indicates that the nanoparticles might be present in the sample (Figure 2.13). From SEM and elemental mapping, we were able to confirm that the nanoparticles were manganese blue (Figure 2.14). The atomic percentage of manganese in this sample from area EDS is 0.7 At%.

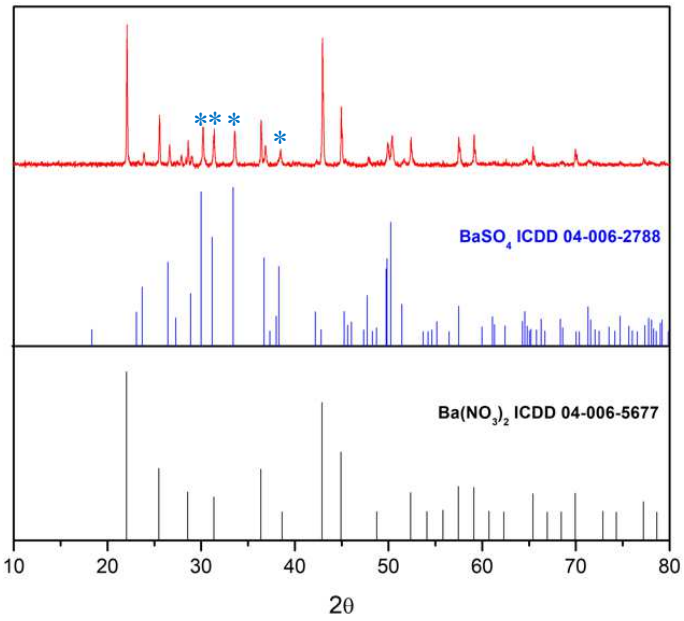

Figure 2.13: PXRD pattern of manganese blue nanoparticle synthesis at 520 °C for 2 hours. Peak broadening is indicated on the pattern by (*).

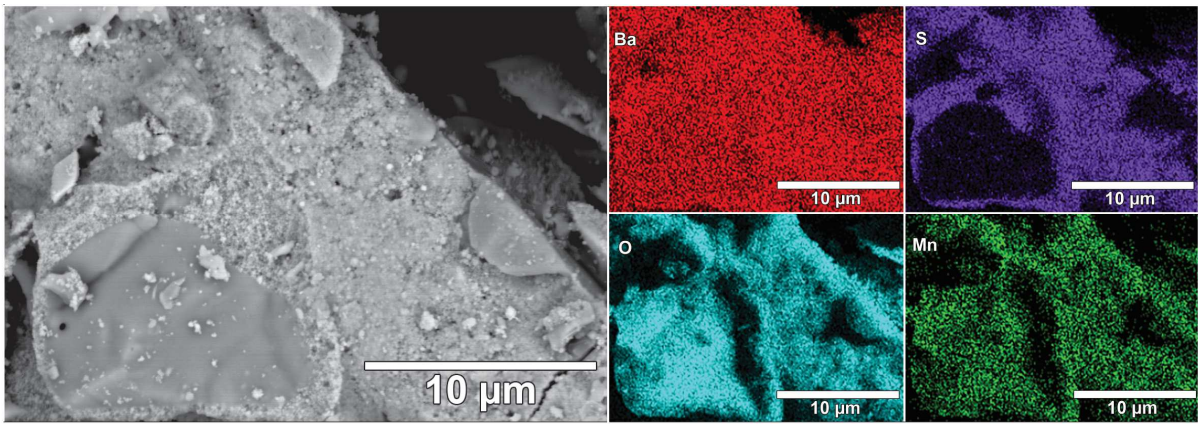

Element	Ba	S	O	Mn
At%	29.1	17.7	62.1	0.7

Figure 2.14: SEM image, corresponding elemental mapping, and elemental composition of manganese blue nanoparticle synthesis at 520 °C for 3 hours.

In efforts to increase the incorporation of manganese in the nanoparticles, therefore, the same sample fired at 520 °C for three hours was reground and fired once again at the same temperature for three additional hours. This time, we noticed that the nanoparticles increased in size and the manganese content in the nanoparticles increased from 0.7 to 0.9 At%. We found that by conducting the post-synthetic acid treatment on the as synthesized nanoparticles, we found that we could get rid of the unreacted materials in the reaction since soluble barium salts were formed and can be easily washed. Our results were confirmed when we did secondary electron (SE) imaging coupled with EDS. PXRD pattern in Figure 2.15(a) indicates only the presence of barium sulfate and the absence of barium nitrate. The SE and elemental mapping show an overlap between barium, sulfur, oxygen, and manganese is consistent with manganese blue composition and suggests homogeneity (Figure 2.15(b)). In terms of the size of the nanoparticles, they were in the range of ~50 – 300 nm indicating that broad size distribution of the nanoparticles with a mean particle size of ~150 nm (Figure 2.15(c)). The atomic percentage of manganese in the sample was still maintained at 0.7 which is an indication that the post-synthetic acid treatment also works for the nanoparticles as the particles were not etched and the manganese content stayed the same as the raw nanoparticles.

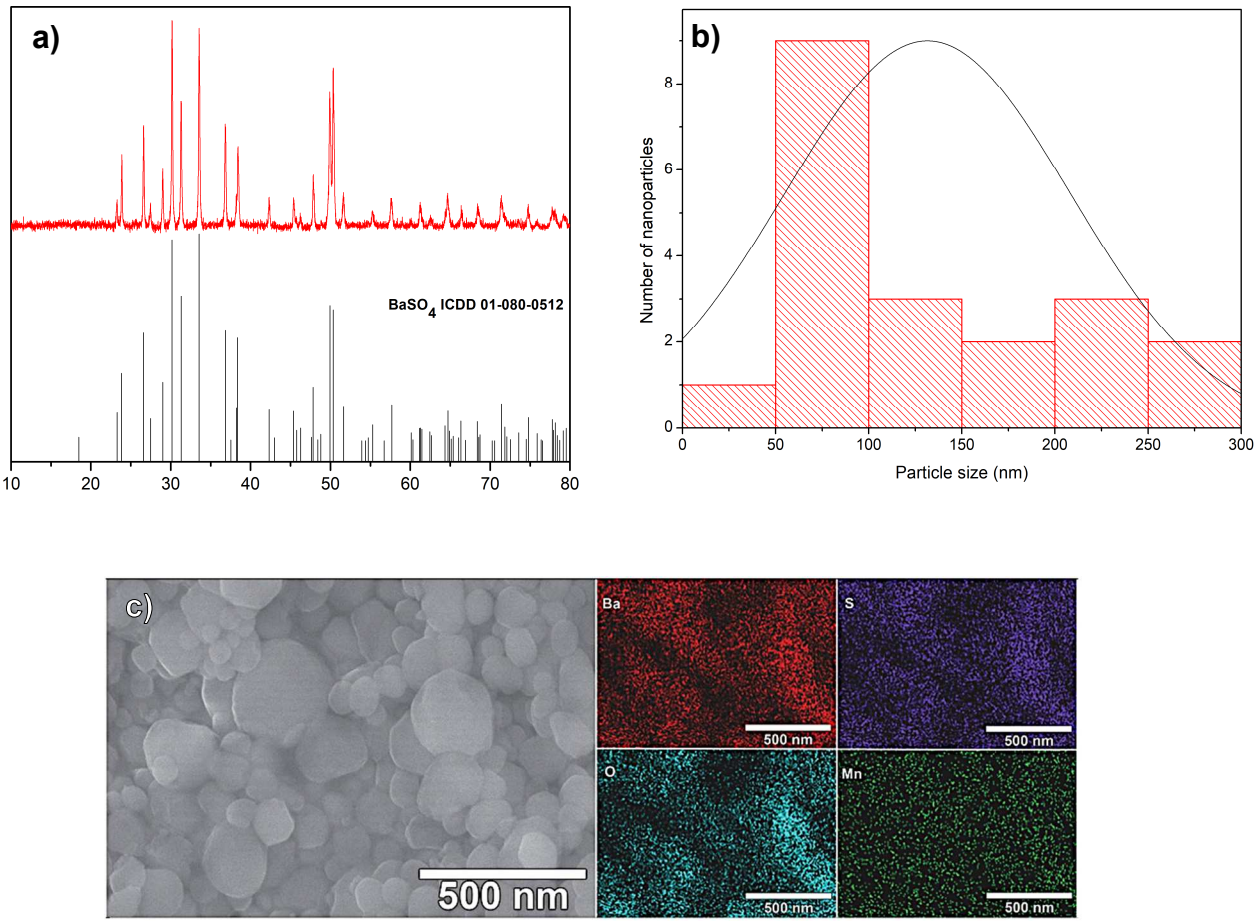

Element	Ba	S	O	Mn
At%	9.8	17.7	10.8	0.7

Figure 2.15: a) PXRD pattern of manganese blue nanoparticles post-synthetic acid treatment indicating that absence of barium nitrate flux, b) particle size distribution obtained from the SE image in (c) and c) SE imaging, the corresponding elemental mapping, and elemental mapping of acid treated manganese blue nanoparticles at 520 °C for 2 hours.

For biomedical applications, it is preferred that the size of the nanoparticles is within the range of 1 – 100 nm in diameter as particles with these dimensions are comparable to biological functional units.[50] Another important aspect is the timely clearance of the nanoparticles used in near-infrared imaging with minimum retention in major organs after administration, preferably

through the renal clearance pathway.[3] Therefore, it is imperative for us to narrow the particle size distribution of the manganese blue nanoparticles. To achieve this, we performed size selection of the acid treated nanoparticles by centrifugation. This was achieved by dispersing the nanoparticles in isopropyl alcohol followed by centrifuging the sample to an rpm as low as 100 – 500 rpm to obtain the smallest particle size. The particles remain in suspension for ~30 minutes. The particles shown in figure 2.16(a), with an improved particle size distribution of ~40 – 160 nm suitable for biomedical imaging, were obtained at 500 rpm. The mean particle size is ~85 nm, Figure 2.16(b)

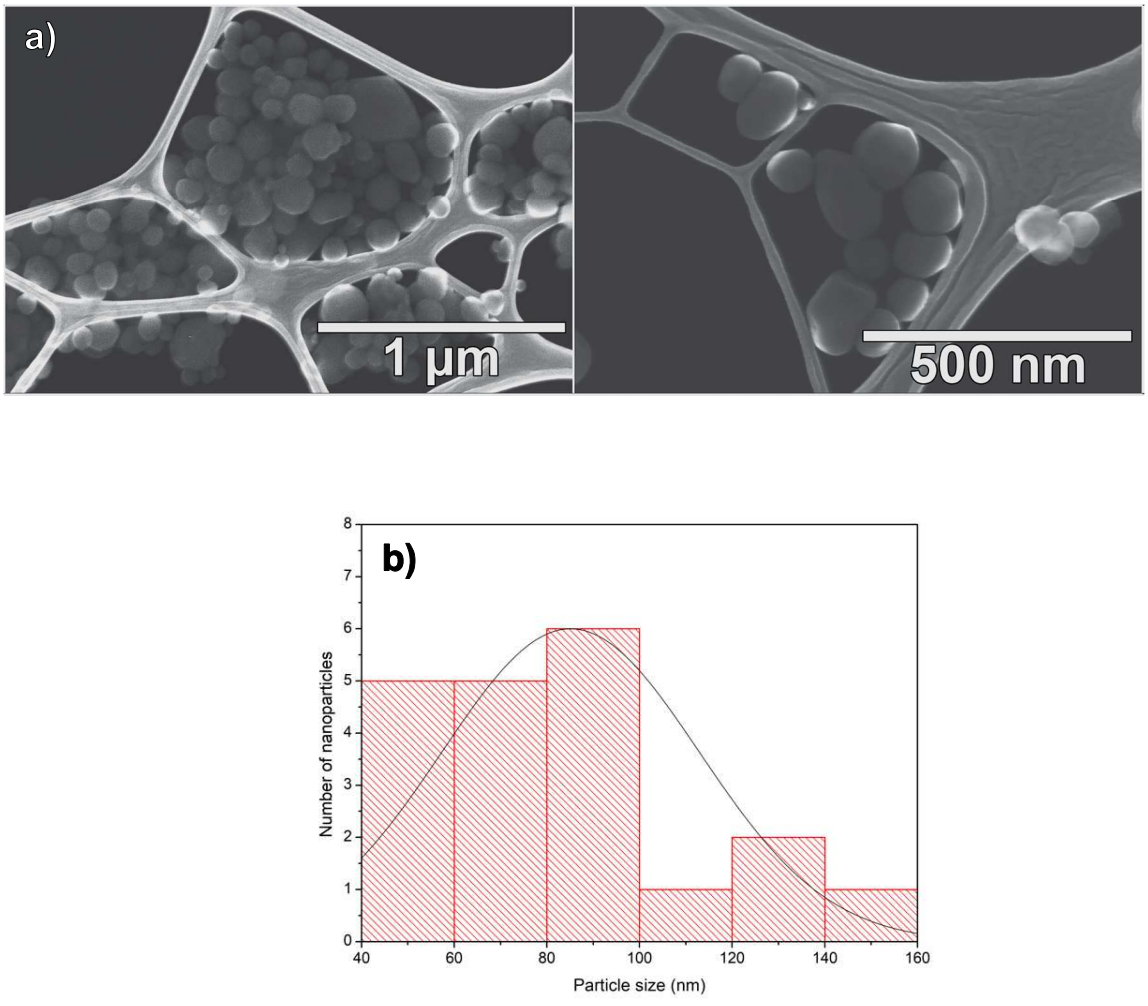

Figure 2.16: a) SE imaging and the corresponding elemental mapping of acid treated manganese blue nanoparticles at 520 °C for 2 hours, and b) particle size distribution using size selection by centrifugation.

Coating of nanoparticles for biomedical imaging applications offers multiple advantages, such as preventing particle agglomeration and helping with further functionalization and conjugation to proteins, enzymes, antibodies, and anticancer drugs.[51] One of the common coating materials is silica, in part due to its high stability, especially in aqueous media. Other reasons include easy regulation of the coating process, chemical inertness, controlled porosity, processability, and most importantly optical transparency.[52] With all that in mind, we proceeded to coat the acid treated nanoparticles with a layer of amorphous silica according to the method suggested by Abe et al for coating of bulk manganese blue pigment.[36] PXRD (Figure 2.17) showed no change in structure between uncoated and coated particles.

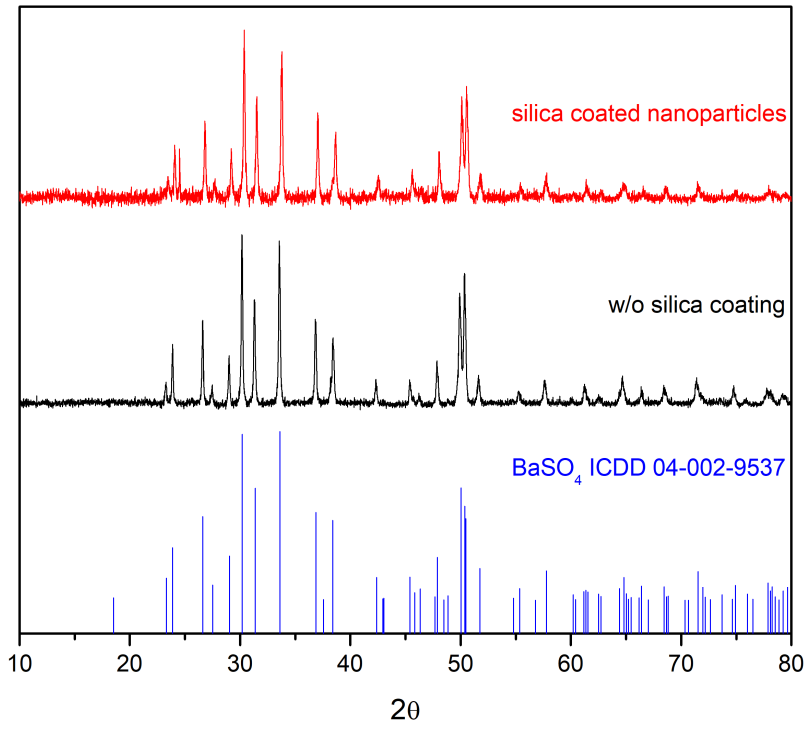

Figure 2.17: PXRD patterns of manganese blue acid treated nanoparticles before silica coating (red pattern) and without silica coating (black pattern).

We also wanted to confirm from the other optical properties such as color and near-infrared imaging shown in Figure 2.18((a) and (b)). The color of the pigment nanoparticles stayed the same as seen with other pigment examples in the literature.[53] This was also reflected in the near-infrared images as qualitatively there was no change in luminescence. SE imaging and elemental mapping as well as EDS mapping shows the homogeneous deposition of amorphous silica on the manganese blue nanoparticles.

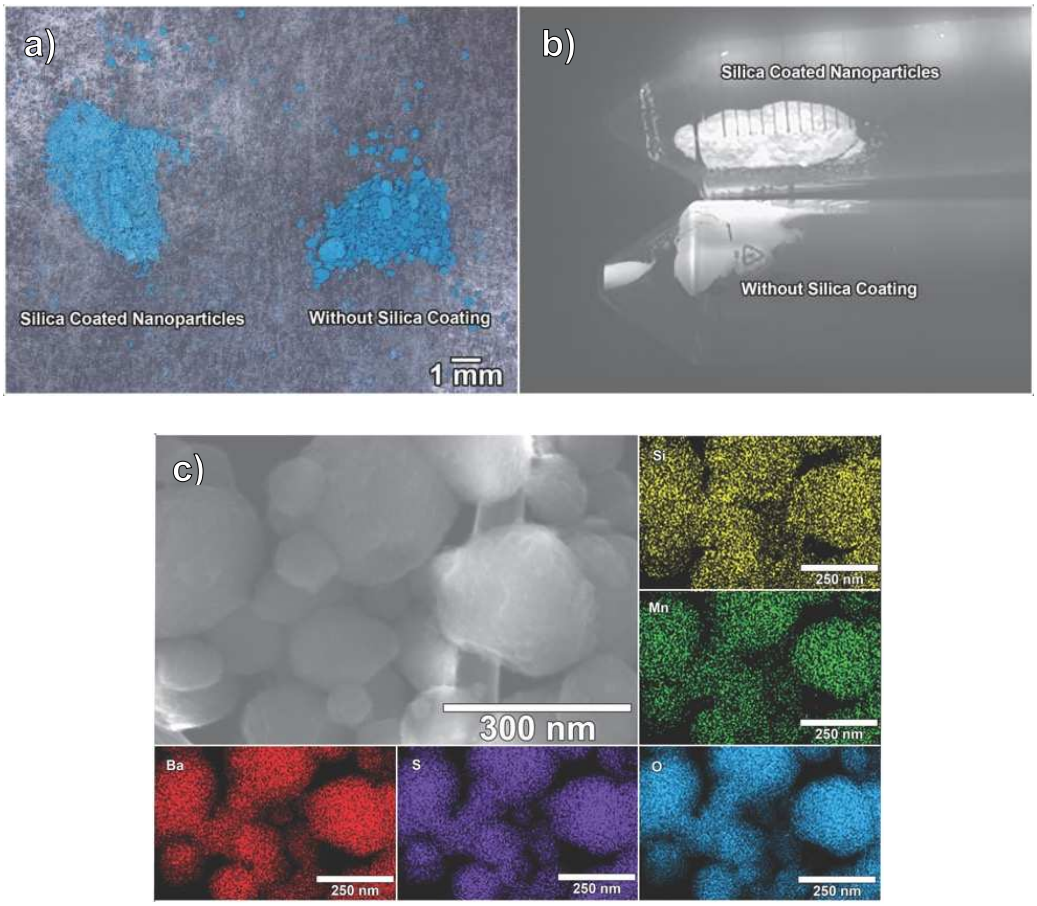

Element	Ba	S	O	Mn	Si
5.0	5.0	6.4	84.9	0.2	3.4

Figure 2.18: a) Comparison between silica coated nanoparticles and without silica coating showing that the color did not change, b) near infrared luminescence imaging comparison of the nanoparticles with and without silica coating. The luminescence is the same intensity from the image, and c) SE and elemental mapping showing the amorphous silica deposition

The particle size distribution for the manganese blue silica coated shows a particle size was in the range of 50 – 250 nm with a mean particle size of ~125 nm, Figure 2.19. We should mention that the particles have been silica coated after the size selection process. The silica coating is estimated to be ~40 nm which means that the particle size distribution needs to be narrowed down using further size selection by centrifugation or the particle size can be reduced by reducing the thickness of the silica coating.

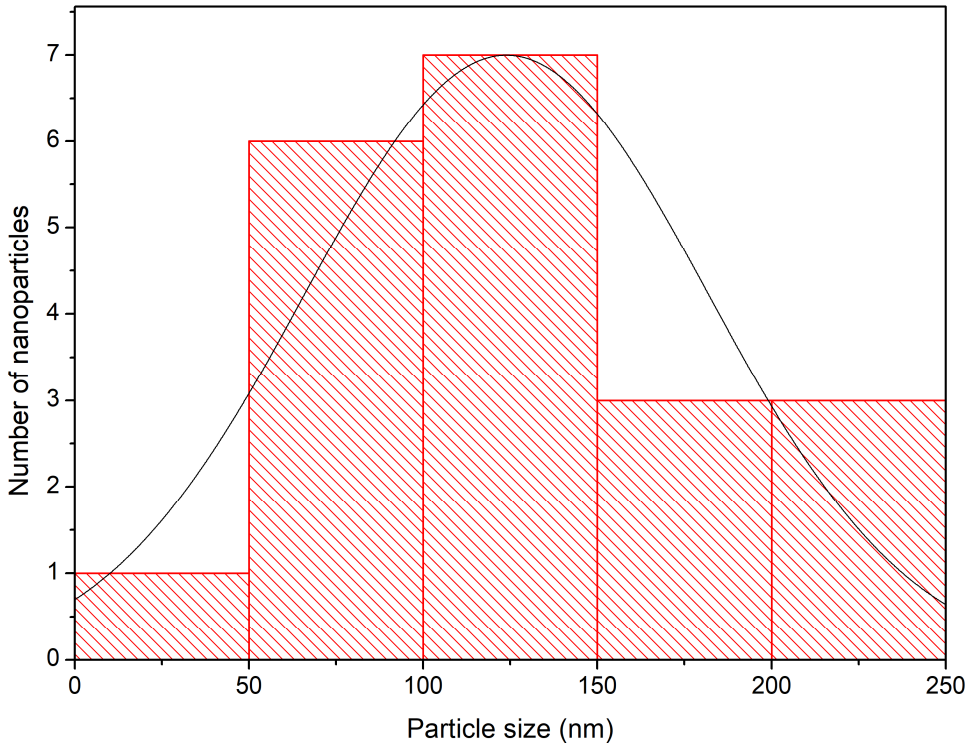

Figure 2.19: Particle size distribution of the silica coated nanoparticles. The mean particle size is ~125 nm.

Conclusion

We successfully synthesized bulk manganese blue pigment using manganese(IV) oxide and barium nitrate, which is an oxidizing flux. We were also able to get a uniform particle size

distribution of the pigment through firing for two hours instead of one hour. The choice of the acid for post-synthetic treatment is also crucial for the color and the manganese content of the pigment. Nitrous acid formed by combining 6.0 M HCl and sodium nitrite is a better choice than for the post-synthetic acid treatment than a dilute solution of hydrochloric acid. We also performed initial stability studies using color fastness, TGA, PXRD, and Raman to evaluate the stability the pigment.

With our understanding and control over the bulk synthesis of the pigment, we applied a similar synthetic procedure using nanoscale starting materials. By using nanoscale reactants, we decreased the reaction temperature to 520 °C from 710 °C, a significant 190 ° change. We also found that by using the same post-synthetic acid procedure, we were able to get rid of the excess barium nitrate flux and obtain the manganese blue nanoparticles. The nanoparticles maintained the same green-blue hue as the bulk manganese blue pigment as well as the near-infrared luminescence.

After we were able to synthesize the manganese blue nanoparticles, our next goal was to narrow the particle size distribution and add an amorphous silica coating for biomedical translation. Through size selection by centrifugation, we were able to narrow the crystal size of manganese blue nanoparticles which particle is ~85 nm which is suitable for our biomedical applications. Importantly, the nanoparticle coating allowed the retention of the material's luminescence, and in future work, it can be modified by well-established chemistries for surface functionalization or drug loading.

References

1. Erich, K. and M. Georg, *Blue pigment colors and aprocess of preparing them*. 1939, Google Patents.
2. Han, X., et al., *Applications of nanoparticles in biomedical imaging.* Nanoscale, 2019. **11**(3): p. 799-819.
3. Hong, G., A.L. Antaris, and H. Dai, *Near-infrared fluorophores for biomedical imaging.* Nature biomedical engineering, 2017. **1**(1): p. 1-22.
4. Johnsen, S., *Hidden in plain sight: the ecology and physiology of organismal transparency.* The Biological Bulletin, 2001. **201**(3): p. 301-318.
5. Frangioni, J.V., *In vivo near-infrared fluorescence imaging.* Current opinion in chemical biology, 2003. **7**(5): p. 626-634.
6. Gao, X., et al., *In vivo cancer targeting and imaging with semiconductor quantum dots.* Nature biotechnology, 2004. **22**(8): p. 969-976.
7. Wang, R. and F. Zhang, *NIR luminescent nanomaterials for biomedical imaging.* Journal of Materials Chemistry B, 2014. **2**(17): p. 2422-2443.
8. Cao, J., et al., *Recent progress in NIR-II contrast agent for biological imaging.* Frontiers in bioengineering and biotechnology, 2020. **7**: p. 487.
9. Cai, Y., et al., *Optical nano-agents in the second near-infrared window for biomedical applications.* Chemical Society Reviews, 2019. **48**(1): p. 22-37.

10. Li, D., et al., *Excretable lanthanide nanoparticle for biomedical imaging and surgical navigation in the second near□infrared window.* Advanced Science, 2019. **6**(23): p. 1902042.

11. Grodzinski, P., et al., *Integrating nanotechnology into cancer care*. 2019, ACS Publications.

12. Li, X., et al., *Metal–ligand coordination nanomaterials for biomedical imaging.* Bioconjugate Chemistry, 2019. **31**(2): p. 332-339.

13. Lee, J.H., et al., *All□in□one target□cell□specific magnetic nanoparticles for simultaneous molecular imaging and siRNA delivery.* Angewandte Chemie International Edition, 2009. **48**(23): p. 4174-4179.

14. Lu, K., et al., *Nanoscale metal–organic frameworks for therapeutic, imaging, and sensing applications.* Advanced Materials, 2018. **30**(37): p. 1707634.

15. Li, X., et al., *The Peptide Functionalized Inorganic Nanoparticles for Cancer-Related Bioanalytical and Biomedical Applications.* Molecules, 2021. **26**(11): p. 3228.

16. Li, X., et al., *Cancer□associated, stimuli□driven, turn on theranostics for multimodality imaging and therapy.* Advanced Materials, 2017. **29**(23): p. 1606857.

17. Gurunathan, S., et al., *Nanoparticle-mediated combination therapy: Two-in-one approach for cancer.* International journal of molecular sciences, 2018. **19**(10): p. 3264.

18. Lian, X., M.-Y. Wei, and Q. Ma, *Nanomedicines for near-infrared fluorescent lifetime-based bioimaging.* Frontiers in Bioengineering and Biotechnology, 2019. **7**: p. 386.

19. Law, W.-C., et al., *Manganese-doped near-infrared emitting nanocrystals for in vivo biomedical imaging.* Optics express, 2016. **24**(16): p. 17553-17561.

20. Han, X., et al., *Heavy Mn 2+-doped near-infrared photon upconversion luminescence in fluoride RbZnF 3: Yb 3+, Mn 2+ guided by dopant distribution simulation.* Journal of Materials Chemistry C, 2020. **8**(35): p. 12164-12172.

21. Feng, X., et al., *Transition metal ion activated near-infrared luminescent materials.* Progress in Materials Science, 2022: p. 100973.

22. Du, J. and D. Poelman, *Near-infrared persistent luminescence in Mn4+ doped perovskite type solid solutions.* Ceramics International, 2019. **45**(7): p. 8345-8353.

23. Li, W., et al., *Near-infrared emission of Yb3+ sensitized by Mn4+ in La2MgTiO6.* Journal of Luminescence, 2018. **194**: p. 547-550.

24. Cao, R., et al., *Near-infrared emission Ba3 (PO4) 2: Mn5+ phosphor and potential application in vivo fluorescence imaging.* Spectrochimica Acta Part A: Molecular and Biomolecular Spectroscopy, 2014. **128**: p. 671-673.

25. Zhang, X., et al., *A general strategy for controllable synthesis of Ba 3 (MO 4) 2: Mn 5+(M= V, P) nanoparticles.* RSC Advances, 2017. **7**(17): p. 10564-10569.

26. Brunold, T.C. and H.U. Güdel, *Absorption and luminescence spectroscopy of manganese-doped BaSO4 crystals.* Chemical Physics Letters, 1996. **257**(1): p. 123-129.

27. Brunold, T.C. and H.U. Güdel, *Absorption and Luminescence Spectroscopy of MnO42--Doped Crystals of BaSO4.* Inorganic chemistry, 1997. **36**(9): p. 1946-1954.

28. Vyboishchik, A. and M. Popov, *Production of deep-coloured pigments from non-ferrous raw materials.* Materials Today: Proceedings, 2021. **38**: p. 1560-1563.

29. Kearton, R., *Pigments and the artist's palette.* Journal of the Society of Dyers and Colourists, 1995. **111**(12): p. 368-372.

30. Reinen, D., et al., *The nature of the colour centre in manganese blue.* ZEITSCHRIFT FUR ANORGANISCHE UND ALLGEMEINE CHEMIE, 1998. **624**: p. 438-442.

31. Accorsi, G., et al., *Imaging, photophysical properties and DFT calculations of manganese blue (barium manganate (VI) sulphate)–a modern pigment.* Chemical Communications, 2014. **50**(97): p. 15297-15300.

32. Ketegenov, T., et al., *Recent Advances in the Preparation of Barium Sulfate Nanoparticles: A Mini-Review.* ChemEngineering, 2022. **6**(2): p. 30.

33. Jackson, C.T., et al., *Advances in engineering near-infrared luminescent materials.* Iscience, 2021. **24**(3): p. 102156.

34. Zhang, X., et al., *Controllable synthesis of Mn6+ doped nanoparticles by a facile anion exchange method.* Nanotechnology, 2016. **28**(2): p. 025604.

35. Ragupathy, P., H. Vasan, and N. Munichandraiah, *Synthesis and characterization of nano-MnO2 for electrochemical supercapacitor studies.* Journal of the Electrochemical Society, 2007. **155**(1): p. A34.

36. Abe, N., K. Kanemaru, and M. Yokoyama, *Method of coating inorganic pigments (ultramarine and bronze powder) with dense amorphous silica*. 1983, Google Patents.

37. Young, J.A., *Barium Nitrate.* Journal of Chemical Education, 2006. **83**(1): p. 34.

38. Wang, Y., et al., *Synthesis and optical properties of Mn-doped Ba3Al2O6 intense blue oxides.* Optical Materials, 2020. **109**: p. 110327.

39. Zhou, Y., et al., *Synthesis and properties of novel turquoise-green pigments based on BaAl2-xMnxO4+ y.* Dyes and Pigments, 2018. **155**: p. 212-217.

40. Moghaddam, A.Z. and G.J. Rees, *Thermal decomposition of potassium permanganate: thermogravimetry, differential scanning calorimetry and hot-stage microscopy studies.* Fuel, 1984. **63**(5): p. 653-656.

41. Herbstein, F., G. Ron, and A. Weissman, *The thermal decomposition of potassium permanganate and related substances. Part I. Chemical aspects.* Journal of the Chemical Society A: Inorganic, Physical, Theoretical, 1971: p. 1821-1826.

42. Henning, H., et al., *Crystal structures and thermal decomposition of permanganates AE [MnO4] 2· n H2O with the heavy alkaline earth elements (AE= Ca, Sr and Ba).* Zeitschrift für Naturforschung B, 2017. **72**(8): p. 555-562.

43. Jildeh, Z.B., et al., *Thermocatalytic behavior of manganese (IV) oxide as nanoporous material on the dissociation of a gas mixture containing hydrogen peroxide.* Nanomaterials, 2018. **8**(4): p. 262.

44. de Beauvoir, T.H., et al., *Densification of MnSO4 ceramics by Cool-SPS: Evidences for a complex sintering mechanism and magnetoelectric coupling.* Journal of the European Ceramic Society, 2018. **38**(11): p. 3867-3874.

45. Kim, S.W., et al., *Discovery of novel inorganic Mn5+-doped sky-blue pigments based on Ca6BaP4O17: Crystal structure, optical and color properties, and color durability.* Dyes and Pigments, 2017. **139**: p. 344-348.

46. Sun, Y., et al., *Enhanced oxide ion conductivity in stabilized cubic BaInO2. 5 by Mn5+ doping.* Inorganic Chemistry Communications, 2013. **33**: p. 151-153.

47. Johnson-McDaniel, D. and T.T. Salguero, *Exfoliation of Egyptian blue and Han blue, two alkali earth copper silicate-based pigments.* JoVE (Journal of Visualized Experiments), 2014(86): p. e51686.

48. Tsuruoka, T., et al., *Nanoporous nanorods fabricated by coordination modulation and oriented attachment growth.* Angewandte Chemie, 2009. **121**(26): p. 4833-4837.

49. Holder, C.F. and R.E. Schaak, *Tutorial on Powder X-ray Diffraction for Characterizing Nanoscale Materials.* ACS Nano, 2019. **13**(7): p. 7359-7365.

50. Nune, S.K., et al., *Nanoparticles for biomedical imaging.* Expert opinion on drug delivery, 2009. **6**(11): p. 1175-1194.

51. McNamara, K. and S.A. Tofail, *Nanoparticles in biomedical applications.* Advances in Physics: X, 2017. **2**(1): p. 54-88.

52. Guerrero□Martínez, A., J. Pérez□Juste, and L.M. Liz□Marzán, *Recent progress on silica coating of nanoparticles and related nanomaterials.* Advanced materials, 2010. **22**(11): p. 1182-1195.

53. Liu, S.-G., et al., *Enhanced high temperature oxidization resistance of silica coated γ-Ce2S3 red pigments.* Applied Surface Science, 2016. **387**: p. 1147-1153.

The EGYPTIAN BLUE– EGYPTIAN FAIENCE CONTINUUM

Based on "The Egyptian Faience – Egyptian Blue Continuum" Eman Abdelrahman, Sang Lee, Briel Power, Peter Lacovara, Renée A. Stein, and Tina T. Salguero. To be submitted to the *Journal of Archaeological sciences*.

Abstract

Two of the most distinctive blue materials of the ancient world—Egyptian blue and Egyptian faience—have similar chemical compositions based on calcium, copper, silicon, and oxygen, yet their micro- and macrostructures are dramatically different. This contribution considers the relationships between these materials. Based on analytical studies of ancient faience objects and modern laboratory reproductions, we find that Egyptian blue and Egyptian faience are chemically related, meaning that relatively small variations in the starting materials can lead to either of these products selectively or to mixed products. Visible-induced luminescence imaging reveals that ancient Egyptian faience objects often contain Egyptian blue crystals within their interiors (i.e., not part of the glassy surface layer); this fact has not been appreciated previously. Laboratory experiments show that two conditions must be met for the in-situ generation of Egyptian blue within faience: (1) there must be a source of calcium ions, such as starting materials (e.g., calcium carbonate, calcium hydroxide, calcium oxide) or substrate (e.g., limestone), and (2) sodium chloride, which inhibits the formation of Egyptian blue, must not be present. These chemical signatures provide new insight into the diverse raw materials used for faience production. Furthermore, our results show how tuning the identity, ratios, and proportions of starting materials leads to a continuum of Egyptian blue-Egyptian faience products. We conclude that the world's first synthetic pigment (Egyptian blue) and the world's first glazed ceramic material (Egyptian faience) were intimately intertwined technochemical developments.

Introduction

As once the English writer and art critic John Ruskin described blue in a quote: *"blue is everlastingly appointed by the deity to be a source of delight"*. Blue has been valued in many cultures, either by its embodiment in beliefs or through expressions in artwork. For example, in ancient Egypt, blue colored semiprecious stones such as lapis lazuli were considered to possess special magical powers for warding off evil spirits and for curing medical ailments.[1] Turquoise, another semiprecious stone was used to adorn deities like Isis, Nephtys, and Nut on pectorals on mummies of kings like Tutankhamen, which represented transcendence.[2] Due to the high demand and rarity of these blue precious stones, there was strong motivation to develop alternatives.[3]

Faience is a glazed ceramic material[4] composed of a sintered ground quartz or quartz sand body, which is crystalline, coated with a glassy, alkaline glaze. This outer glaze and minor glassy components within the body serve to bind the silica-rich core grains together.[5-7] The glaze was often colored and, depending on the colorant used, different glaze colors were produced. For example, copper oxide produces an attractive green-blue glaze like turquoise. The production of faience started in Egypt and the Near East around the 4th or 5th millennium BC and continued until the Roman Period.[5] Faience was used most often to make small objects such as beads, amulets, small figurines, simple bowls, cosmetic jars, rings, or other trinkets.[8]

Faience is a complex, composite system that involves mixing the quartz source with amounts of lime (CaO and/or $Ca(OH)_2$), an alkali flux that can be derived either from natron or plant ashes; the resulting material is fired at temperatures in the range of 950-1000 °C.[9, 10] Three fabrication techniques have been employed for making faience objects: application, cementation, and efflorescence glazing. In application glazing, the glazing powder or slurry is applied to the faience core. Cementation glazing involves the burial of the unglazed dry faience core in a glazing

powder that partially melts on heating, reacting with the surface quartz core and glazing it. Finally, the efflorescence technique is unique in combining the glaze mixture in the core, mixing it water, and leaving it to dry, which results in the migration of salts to the object's surface. Upon firing, this salt mixture generates the glaze.[11]

Around the same era that faience production began, Egyptian blue pigment with the chemical formula of $CaCuSi_4O_{10}$ was also first produced. Egyptian blue was the first synthetic pigment ever produced and, like faience, was also used to produce objects like beads, statuettes, scarabs, and inlays with a very similar color and luster to lapis lazuli.[12] Egyptian blue is synthesized using components similar to faience; quartz, lime, a copper compound, and an alkali flux. The reactants are fired at a temperature range of 850–1000 °C.

With very similar compositions (calcium, copper, and silicon) and firing conditions, faience and Egyptian blue possess similar features. In this work we describe the formation of Egyptian blue crystals within a matrix of Egyptian faience. The motivation behind our research lies in our collaboration with Michael C. Carlos Museum at Emory University. We were allowed the opportunity to screen authentic ancient faience samples and found that numerous examples display near infrared luminescence from the crystalline silica core. To duplication this phenomenon, we prepared faience samples using a melt flux route using different sources of calcium, copper, and fluxes. By optimizing stoichiometry, reaction conditions, and flux composition, we were able to achieve the in-situ formation of Egyptian blue in the quartz core of Egyptian faience. These results were corroborated with SEM/EDS and near infrared luminescence imaging. We also established the existence of a material continuum, with Egyptian faience on one end and Egyptian blue at the other extreme, that is accessible by tuning the stoichiometry and concentration of the calcium source.

Materials Preparation and Characterization

1. Visible-induced luminescence imaging

Faience samples were illuminated with a red LED light array (LEDLB-24-RED/BLUE-F-BLACK, 72 Watts - 9~42 VDC, Larson Electronics LLC) and imaged using a Xenics Bobcat 320-GigE Vision 100 Hz camera (0.9 to 1.7 μm imaging range). Images were post-processed using Adobe Photoshop CC 2018; specifically, the dimensions of the images were adjusted to a width of 1500 and then cropped, and the luminescence was false-colored for clarity.

2. Laboratory sample preparation

Materials: Quartz pebbles (obtained from the Department of Geology, University of Georgia) were pre-ground using a Fritsch Pulverisette 6 planetary ball mill (using ~30, 10 mm silicon nitride grinding balls in a 80 mL silicon nitride milling bowl) at 450 rpm for 30 min. Kaolinite, Na_2CO_3 (anhydrous powder, 99.999% trace metal basis), $Ca(OH)_2$ (ACS reagent, ≥95.0% purity), $CaCO_3$ (BioXtra, ≥99.0 % purity), $NaHCO_3$ (BAKER ANALYSED™ A.C.S reagent, JT Baker™) and CuO (99.99% trace metal basis) were purchased from Sigma-Aldrich. CaO was prepared by firing $CaCO_3$ in a box furnace at 1000 °C for 12 h. Additional materials include ball clay (obtained from the Ceramics program, Lamar Dodd School of Art, University of Georgia) and commercial gum arabic (Jacquard brand, "pure *Acacia Senegal* and *A. Arabica*").

Faience preparation (efflorescence method): 0.750 g (12.5 mmol) of pre-ground quartz, 0.0500g (0.194 mmol) of kaolinite, 0.0500 g of ball clay, 0.0500 g (0.472 mmol) of Na_2CO_3, 0.0500 g

(0.675 mmol) of $Ca(OH)_2$ or 0.0675 g (0.675 mmol) of $CaCO_3$ or 0.0378 g (0.675 mmol) of CaO, 0.0500 g (0.595 mmol) of $NaHCO_3$, 0.0107 g of gum Arabic, and 0.0150 g (0.188 mmol) of CuO were ground together using a Fritsch Pulverisette 6 planetary ball mill (using ~30, 10 mm silicon nitride grinding balls in a 80 mL silicon nitride milling bowl) at 450 rpm for 30 min. The resulting grey powder was mixed with 216 μL of distilled water to form a paste, which then was molded into a ~10×2.5 mm soft pellet. This material was placed on a substrate (alumina, terracotta) and allowed to effloresce overnight. Then the sample/substrate was transferred to a box furnace and fired at 930 °C (heating ramp of 15 °C/min) for 12 h. The furnace was allowed to cool down naturally. The product pellet easily separates from the substrate.

Crystal growth studies: for *controlled cooling* experiment, we followed the cooling method according to Pradell et al.[13] Faience was heated in a box furnace at a ramp rate of 3 °C/min to 930 °C and left to dwell for 12 hours at 930 °C. The sample was cooled form 930 °C to 650 °C at a rate of 2 °C/min. Beyond 650 °C the sample was allowed to cool naturally to room temperature. For *controlled cooling* experiment following Johnson-Mc Daniel et al.[14] the samples were fired to 930 °C (heating ramp of 5 °C/min), then dwell for 12 h at 930 °C then the sample is cooled at a rate of 0.8 °C/min from 930 °C to room temperature. For the crystal growth of Egyptian blue in Faience using an *air quench* technique, the faience pellet was fired to 930 °C (heating ramp of 5 °C/min) and left to dwell for 12 h at 930 °C. At the end of the 12 hours, the sample was taken out of the furnace at 930 °C and left to cool on the bench top naturally to room temperature.

Preparation of Egyptian Blue Objects:

The synthesis of EB objects entails a two-step synthesis process. In the first step, 0.600 g (9.90 mmol) of pre-ground quartz, 0.0500g (0.194 mmol) of kaolinite, 0.0500 g of ball clay, 0.0500 g (0.472 mmol) of Na_2CO_3, 0.0200 g (2.70 mmol) of $Ca(OH)_2$, 0.0500 g (0.595 mmol) of $NaHCO_3$, 0.0107 g of gum Arabic, and 0.0210 g (2.90 mmol) of CuO were ground together using a Fritsch Pulverisette 6 planetary ball mill (using ~30, 10 mm silicon nitride grinding balls in a 80 mL silicon nitride milling bowl) at 450 rpm for 30 min. The resulting grey black powder was mixed with 216 μL of distilled water to form a paste, which then was molded into a ~10×2.5 mm soft pellet. This material was placed on a substrate (alumina, terracotta) and allowed to effloresce overnight. Then the sample/substrate was transferred to a box furnace and fired at 930 °C (heating ramp of 15 °C/min) for 12 h. The furnace was allowed to cool down naturally. The grey black product pellet does not separate easily from the substrate. In the second step, the black-grey product pellet is broken into smaller pieces using an agate mortar and pestle and mixed with an additional 20% quartz, 5% quartz, 5% ball clay (the percentages are by mass of the pellet) then transferred to a Fritsch Pulverisette 6 planetary ball mill (using ~30, 10 mm silicon nitride grinding balls in an 80 mL silicon nitride milling bowl) at 450 rpm for 30 min. The product is mixed with water until it forms a paste. The paste formed is thixotropic. The paste is then pressed into a silicon chocolate mold, followed by removal from the mold then left to dry overnight. The dried sample in step 2 is transferred to a substrate (alumina, terracotta) and fired at 930 °C (heating ramp of 15 °C/min) for 12 h. The blue product separates easily from the substrate.

3. Material characterization

Sample preparation: Faience was cut using a Buhler IsoMet™ low speed precision saw. Samples were mounted (with exposed cross section) in a mixture of 2:1 Buhler EpoThin™ epoxy:hardener, then allowed to set for 24 h. Then each epoxy puck was transferred to a Hilloquest thin section machine to further expose the material's cross-section. Then each puck was transferred to a glass plate where it was hand-polished for 15 min using 600 μm grit silicon carbide powder and 15 min using 1000 μm grit silicon carbide powder. This was followed by transferring each epoxy puck to a Buhler MiniMet™ 1000 grinder polisher, where they were polished using 5 μm grit for 80 min and 1 μm grit for 80 min.

Optical microscopy: Samples were examined using a Leica DVM6 digital microscope with a 3664 x 2748-pixel camera using a low magnification objective (190x magnification). Illumination source was a ringlight LED array. Z-stacking was used for pellet cross-section.

SEM/EDS: Polished cross sections were coated by approximately depositing a 200 Å layer of carbon using a JOEL JEE-4x vacuum evaporator. Samples were examined by scanning electron microscopy (SEM) with an FEI Teneo FE-SEM, operating at 10 keV and using a spot size of 10. Energy-dispersive spectroscopy (EDS) data were collected with an integrated Oxford Instruments X-MAX^N detector operated at 10 keV. The EDS results are an average of three different spots/areas. The dimensions of the images have an average of height of 55.63 μm and average width of 83.51μm.

Powder X-ray diffraction (PXRD): Powder X-ray diffraction (PXRD) was conducted on the powder sample using a Bruker D8 instrument with a Co-Kα X-ray source ($\boldsymbol{\lambda} = 1.78890$ Å) operated at 35 kV and 40 mA. The data were collected from 10° to 80° 2θ at a scan rate of 0.1 s/step.

Results and Discussion

In-situ synthesis of Egyptian blue crystals in Egyptian faience

Figure 1. shows nine faience objects obtained from the Michael C. Carlos University with their origin, the period the samples were synthesized in, optical images, and corresponding near-infrared luminescence images with an outline to show the objects' boundaries. The luminescence is produced either from the cross-section of the objects or in one case from the surface of the object. We attempted to reproduce similar results using the efflorescence method. There have been few reports in the literature for the synthesis of Egyptian Faience using the efflorescence method[4, 6,8] but none of these reports have conducted near infrared imaging to show the presence of Egyptian blue in the crystalline silica core.

The synthesis procedure we followed is a melt flux synthesis process which serves two purposes: the formation of a glassy glaze and of Egyptian blue crystals in the faience core. Since this is a melt flux synthesis method the component of the flux plays a major role. We have attempted to use the following salt mixture as a flux: sodium chloride, sodium bicarbonate, and sodium carbonate in a (1: 1.2: 1.8) but unfortunately when the faience samples were synthesized using this flux mixture no near-infrared luminescence was observed. This could be explained by the fact that the growth Egyptian blue crystals were inhibited by the presence sodium chloride in the flux mixture according to the results reported by Giménez et al.[15] They found that if the

concentration of sodium chloride is > 10%, there will be no formation of Egyptian blue crystals and they found that Egyptian green pigment in which the main component is wollastonite or parawollastonite, a calcium silicate polymorph and a copper-rich amorphous phase. The percentage of NaCl in our faience reactions was 5% but the temperature at which the faience has been fired at might play an important role. Egyptian blue crystals exist in the range of 870 – 1080 °C, and parawollastonite exists ~900-950 °C and 1150 °C. Therefore, there is an overlap in two ranges for the formation of Egyptian blue and wollastonite. Our faience synthesis occurs at 930 °C, which is a high temperature and in addition the presence of sodium chloride might have been an additional factor for inhibiting the formation of Egyptian blue crystals and favoring the formation of wollastonite. The formation of Egyptian blue is also desirable at lower temperatures such as ~800 °C.[16]

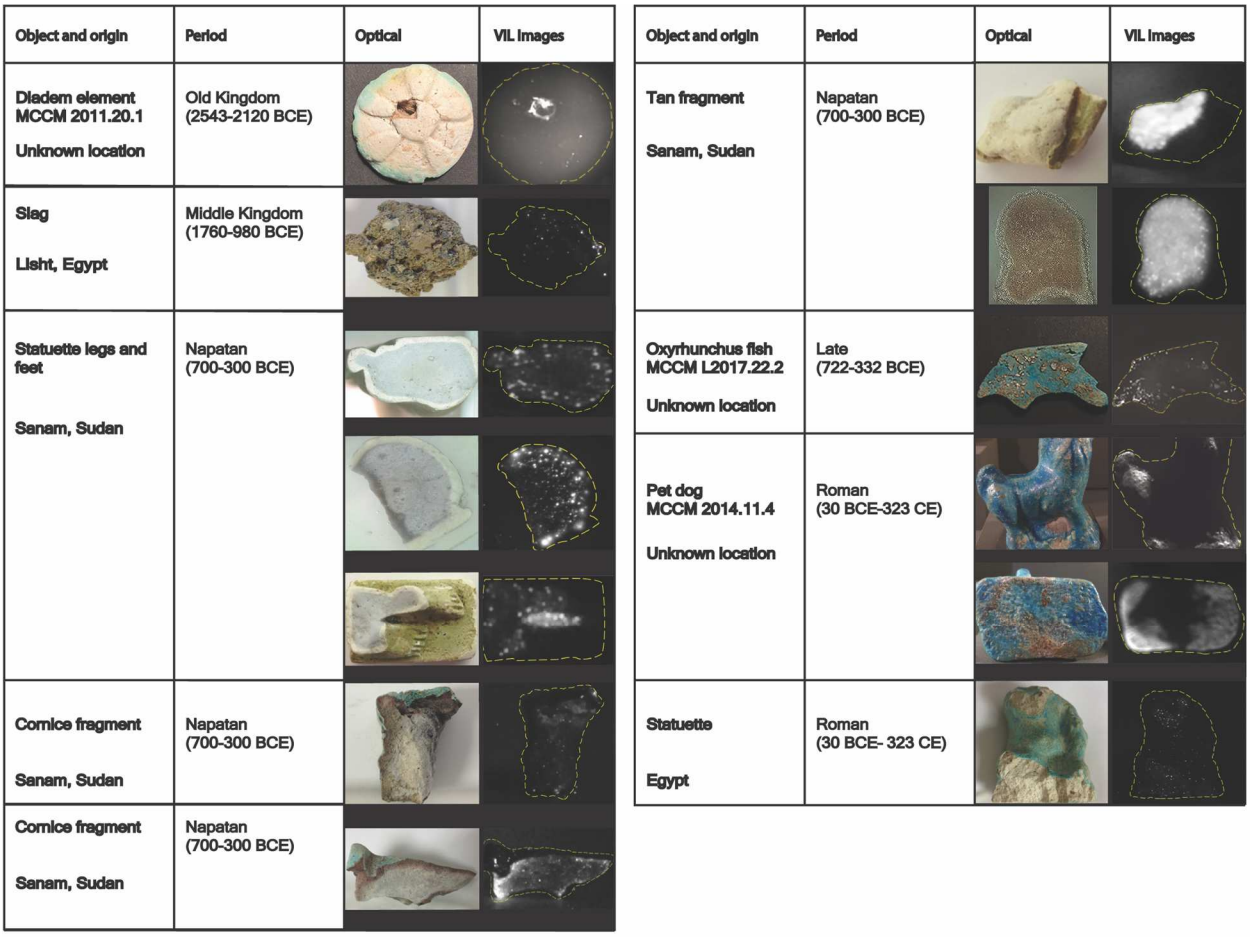

Figure 1. Optical and corresponding near-infrared luminescence images of nine ancient faience objects with the origin and production era.

With these findings, we excluded sodium chloride from the melt flux, and we were successfully able to achieve the in-situ synthesis of Egyptian blue in Faience as shown in Figure 2. The image to the left is the optical image of a polished cross-section of a lab synthesized and to the right is a near infrared image showing light emitted from the sample as which due to the presence of Egyptian blue crystals formed in faience. The near-infrared luminescence is produced in the faience body or core as indicated by the red arrows in Figure 2. The faience body is mainly composed of crystalline quartz grains and the formation of Egyptian blue crystals occurs in the crystalline body versus the amorphous glassy glaze. From Figure 2., the faience samples shown

have blue colored cross-sections which gave us an idea about the diffusion of ions particularly Cu^{2+}. The first ion to diffuse into this liquid phase is Cu^{2+}, possibly from the glaze to the body which explains the blue color throughout the faience samples. This is followed the by the decomposition of the soda flux at ~760 °C forming a eutectic mixture with quartz giving rise to a liquid phase that covers and consumes the quartz crystals. The Cu^{2+} ions also form an amorphous coating around the quartz crystals at ~900 °C. At ~900 °C, Ca^{2+} ions start diffusing and the crystallization of crystalline phases such as calcium silicate (CaSiO3) and Egyptian blue (CaCuSi4O10) have high nucleation rate at this elevated temperature.[17]

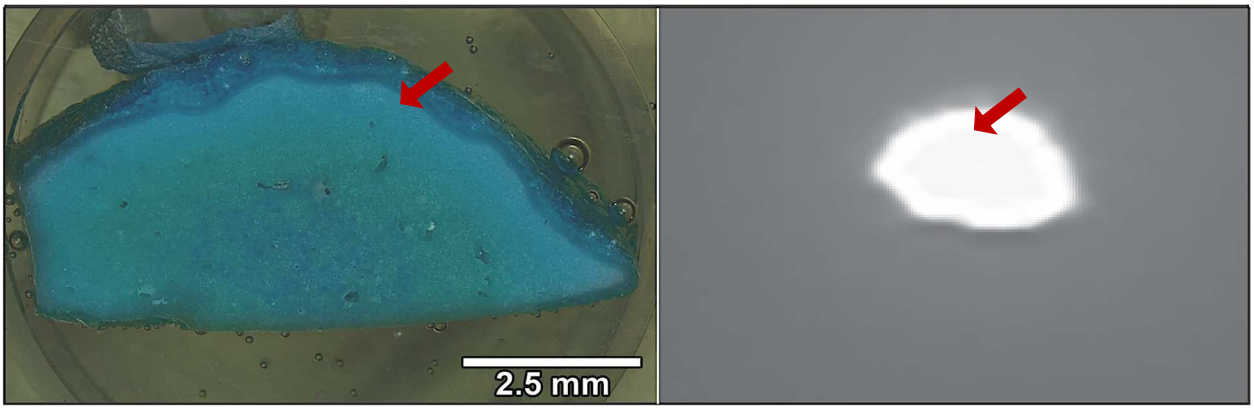

Figure 2. Optical image of a polished cross-section of lab synthesized faience sample (left) and the corresponding near-infrared image (right). The light emitted from the core of the faience sample indicated by the red arrow and corresponds to the in-situ formation of Egyptian blue in the sample.

We have also noticed that mechanochemical grinding process is imperative for the in-situ Synthesis of Egyptian blue in Faience. Mechanochemical grinding processes include but not limited to grinding with a mortar and pestle and ball-milling in which the powder reactants are shaken vigorously with balls made of materials such as stainless steel in a sealed vessel.[18] Ball-milling provides shear-force where the particle size is reduced by impact and attrition which causes a reduction in crystallite and particle size, to create structural defects, and increases the surface

area to allow greater reactivity.[19, 20] Grinding using a ball mill was a process that we conducted religiously throughout our synthetic experiments. As a control, we conducted the synthesis of Egyptian blue in Faience using an agate mortar and pestle and we noticed a substantial difference in the results between manual grinding with an agate mortar and pestle and grinding using ball-milling. Figure 2. shows the optical images of a faience samples and corresponding near-infrared images synthesized using ball milling and grinding using an agate mortar and pestle. It is worthy to mention that manual grinding of a single faience sample took ~2 hours each day for 10 days to produce near-infrared luminescence which indicates the formation of Egyptian blue. From the results in Figure 2., there is a clear difference in the luminescence produced from the faience core in the two samples which can be related to the efficiency of grinding. When compared to the ancient faience samples in Figure 1. that produced a substantial amount of luminescence indicates that in ancient times they might have used intensive labor and time to produce powder reactants that are fine for their faience objects.

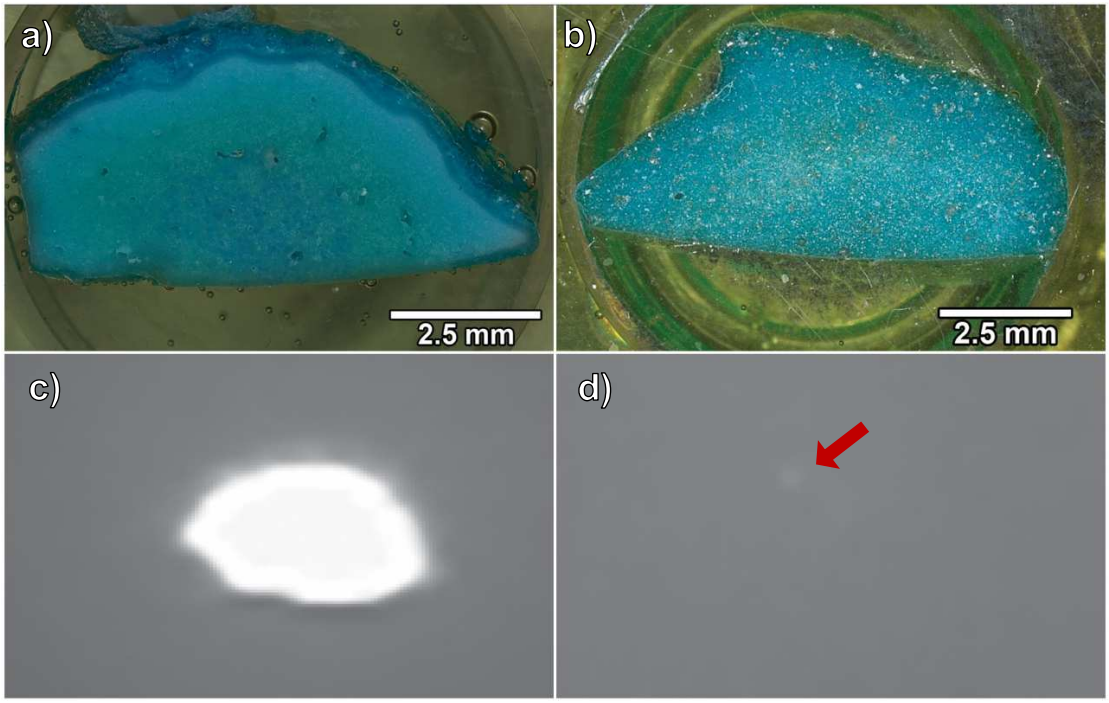

Figure 3. Optical images of lab synthesized faience samples using ball milling (a) and manual grinding with an agate mortar and pestle (b). The corresponding near-infrared images (c) and (d) are shown below the optical image. In image (d), the very faint near-infrared luminescence from the sample ground with an agate mortar and pestle is indicated by a red arrow.

Egyptian blue-Egyptian faience continuum

Although faience is a complex system, we achieved the growth of Egyptian blue crystals in the faience core, and with our prior knowledge of the overlapping compositions of faience and Egyptian blue, there is a possibility of creating a continuum between the two materials. In fact, by varying the concentration of the calcium source in our faience recipes, we were able to tune the concentration of Egyptian blue crystals and thus the luminescence from this series of faience samples. Figure 4. shows the optical and SEM images of seven lab-synthesized faience samples with variable concentrations of calcium hydroxide. The ratio of calcium to copper in each sample

has also been reported for each sample in Figure 4. Table 1 represents the percent weight oxide of the seven samples shown in Figure 4.

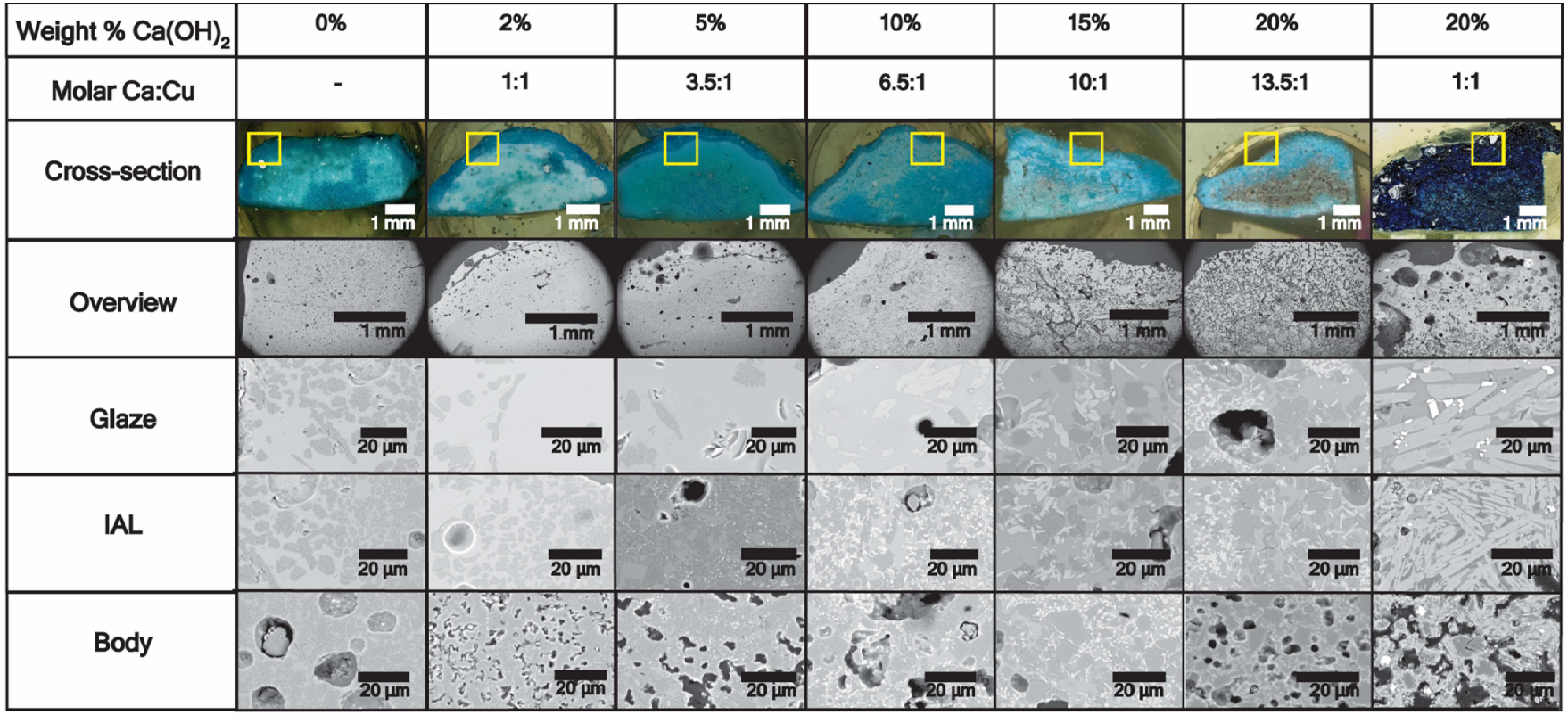

Figure 4. Optical microscope images of polished cross-sections of lab synthesized faience samples using variable concentrations of calcium hydroxide. The corresponding SEM images for each samples reveals the faience microstructures (glaze, interaction layer, and body) as the concentration of calcium hydroxide changes. The sample labeled 20% to the extreme right has an equal molar concentration of calcium and copper.

		SiO_2	CaO	Na_2O	CuO	Al_2O_3	K_2O	TiO_2	N_2O/CaO	Na_2O/CuO
0%	**Glaze**	82.4	-	10.5	3.3	-	0.4	-	-	3.2
	IAL	89.6	-	4.4	1.6	-	0.3	-	-	2.7
	Body	89.2	-	3.9	1.9	4.5	0.2	0.2	-	2.0
2%	**Glaze**	78.2	2.2	15.1	5.5	-	0.5	0.2	6.9	2.7
	IAL	84.4	1.3	8.3	2.9	2.6	0.3	0.2	6.4	2.9
	Body	87.3	1.7	2.6	1.2	6.8	0.2	-	1.5	2.2
5%	**Glaze**	76.7	4.7	11.3	4.2	2.7	0.5	-	2.4	2.7
	IAL	87.4	3.5	4.4	1.3	3.3	-	-	1.3	3.4
	Body	88.7	3.5	0.3	0.1	3.8	-	-	0.1	3
10%	**Glaze**	69.1	8.9	12.3	6.1	3.2	0.4	-	1.4	2.0
	IAL	80.0	8.2	5.9	2.6	3.1	0.2	-	0.7	2.3
	Body	81.2	7.6	4.3	2.1	4.5	-	0.2	0.6	2.0
15%	**Glaze**	73.2	11.4	9.1	3.3	2.5	0.3	0.2	0.8	2.7
	IAL	76.5	9.9	5.3	2.3	2.8	0.2	-	0.5	2.3
	Body	80.1	8.5	5.1	2.2	3.7	0.3	-	0.6	2.3
20%	**Glaze**	78.4	9.4	7.1	1.8	3.1	0.2	-	0.7	3.9
	IAL	80.0	9.2	6.5	1.5	2.6	0.2	-	0.7	4.3
	Body	74.9	14.0	3.8	1.6	5.4	0.2	-	0.3	2.3
20% EB	**Glaze**	58.2	10.5	4.0	24.8	2.2	0.1	-	0.4	0.2
	IAL	62.0	11.8	3.1	20.3	2.5	0.2	-	0.3	0.1
	Body	63.9	10.4	2.4	17.9	5.1	0.3	-	0.2	0.1

Table 1. Oxide wt% of the elements present in the faience microstructures along with Na_2O/CaO and N_2O/CuO ratios. IAL = interaction layer.

Typically, faience has three distinctive microstructures: an outermost, glassy glaze layer, an interaction layer consisting of quartz embedded the continuous glassy glaze and the core contains varying amounts of interparticle glass binding other adjacent quartz particles together.[21] We have tracked the changes in the faience microstructures as the concentration of calcium hydroxide increases using SEM as shown in Figure 5. As we increase the concentration of calcium from 0% to 5%, we noticed that there is no change in the glaze, interaction layer or quartz-based core. But starting at 10% calcium hydroxide concentration, we observed the formation of needle-like crystals especially in the interaction layer and the quartz-core that grew larger in size as we approach 15 % concentration. As confirmed using EDS Figure 5., the needle like crystals were parawollastonite crystals in SEM image of the glaze of the 15% sample. Parawollastonite, a calcium silicate polymorph with the formula $CaSiO_3$, starts forming at a temperature between 900-950 to 1150 °C and these crystals are usually embedded in the silica-rich copper-containing glassy phase. It has been reported by Pagés-Camagna et al., that parawollastonite forms when there is a high concentration of calcium exceeding the concentration of copper.[17] The SEM images of the interaction layer in Figure 5. And glaze of a faience sample prepared with a ratio of calcium to copper of 10:1 show the presence of copious parawollastonite crystals, which are around 5 μm in size in the interaction layer and body.

Upon increasing the concentration of copper such that the molar concentration of calcium hydroxide to copper oxide is 1:1 in the 20% sample, we noticed the formation of rectangular, rod-shaped crystals. From Figure 5., we noticed an overlap of calcium, copper, and silicon on the elemental map which strongly indicates that the sample consists mostly of Egyptian blue crystals. This also matches the morphology of Egyptian blue described in the literature upon investigation of ancient samples.[17, 22, 23] To further confirm that the 20% sample with the calcium hydroxide to

copper oxide ratio of 1:1 is mostly Egyptian blue, we conducted PXRD. The PXRD pattern matched to calcium copper tetrasilicate, as shown in Figure 6.(a), with a minor phase of calcium silicate at ~27° and 29° 2θ, which often forms with Egyptian blue. There is also a peak at ~35° 2θ that corresponds to cristobalite, a high temperature of silicon dioxide. We attempted to further process the sample by grinding and refiring it once again. The PXRD results in Figure 6.(b) show that with the sample processing through regrinding and firing the sample, the calcium silicate at ~27° and 29° 2θ as well as ~35° 2θ peaks become quite diminished. Figure 6.(c) shows a zoomed in view of the PXRD patterns of the two samples and the calcium silicate peaks are affected. Microstructural analysis of ancient Egyptian blue objects has revealed that the final objects after a two-step production process reveal the presence of silicates such as wollastonite.[17, 24, 25] The wollastonite phase can also be confirmed from our elemental mapping for the 20% sample as shown in the calcium rich regions on the map. Finally, in the 20% sample in Figure 5. we noticed the presence of some bright features by SEM. From the elemental mapping and composition, we confirmed that these bright particles were copper oxide with chemical formula CuO (tenorite phase).[26, 27] This copper oxide phase did not appear as one of the phases on PXRD, perhaps due to low concentration.

Examining the data in Table 1., we noticed a common trend among the percentage weight oxides. Faience is a quartz ceramic, in which the quartz particles are held by a glassy phase. In all the samples, SiO_2 increases from the glaze to the interaction layer to the core of the faience as the core consists mostly of quartz particles. The glaze on the faience we prepared in the lab is a soda-lime glaze. In the 2, 5, 10, and 15 % samples we noticed that the wt% of calcium oxide is the highest in the glaze and decreases as we move to the core. On the contrary, both 20% samples have a higher CaO wt% in the body versus the glaze and the interaction layer. This is probably due to

the abundance of the crystalline phases in the two samples whether it is wollastonite or Egyptian blue. We also noticed that Na_2O has the highest wt% in the glaze. In the efflorescence synthetic method that we employed for the synthesis of faience, the flux mixture is added to the rest of the powder reactants and left to dry before firing. Upon drying, and while the water is evaporating, the salts are brought to the surface by capillary action and deposited on the surface. When the samples are fired the flux salts melt and form the glassy glaze.

With regards to the Na_2O/CaO ratios, we noticed that the ratios decrease from the glaze to the interaction layer to the body. One possible explanation would be the preferential efflorescence of sodium carbonate and sodium bicarbonate which are the flux components over the insoluble components such as calcium hydroxide and copper oxide when the water evaporates pulling the components to the surface. Although calcium hydroxide and copper oxide do not experience significant efflorescence, when fired the effloresced carbonates react with the underlying calcium hydroxide and copper oxide to form the glaze.[5] As for the Na_2O/CuO ratio, we noticed that the this particular value for the glaze and the interaction layer are more or less the same or slightly higher in the interaction layer due to the presence of an extensive network of interstitial glass holding the quartz grains together. In the faience 20% $Ca(OH)_2$ sample with the same calcium to copper ratio, has the lowest Na_2O/CuO and Na_2O/CaO ratios and one possible explanation is the formation of crystalline Egyptian blue and the decreased content of the glass phases.

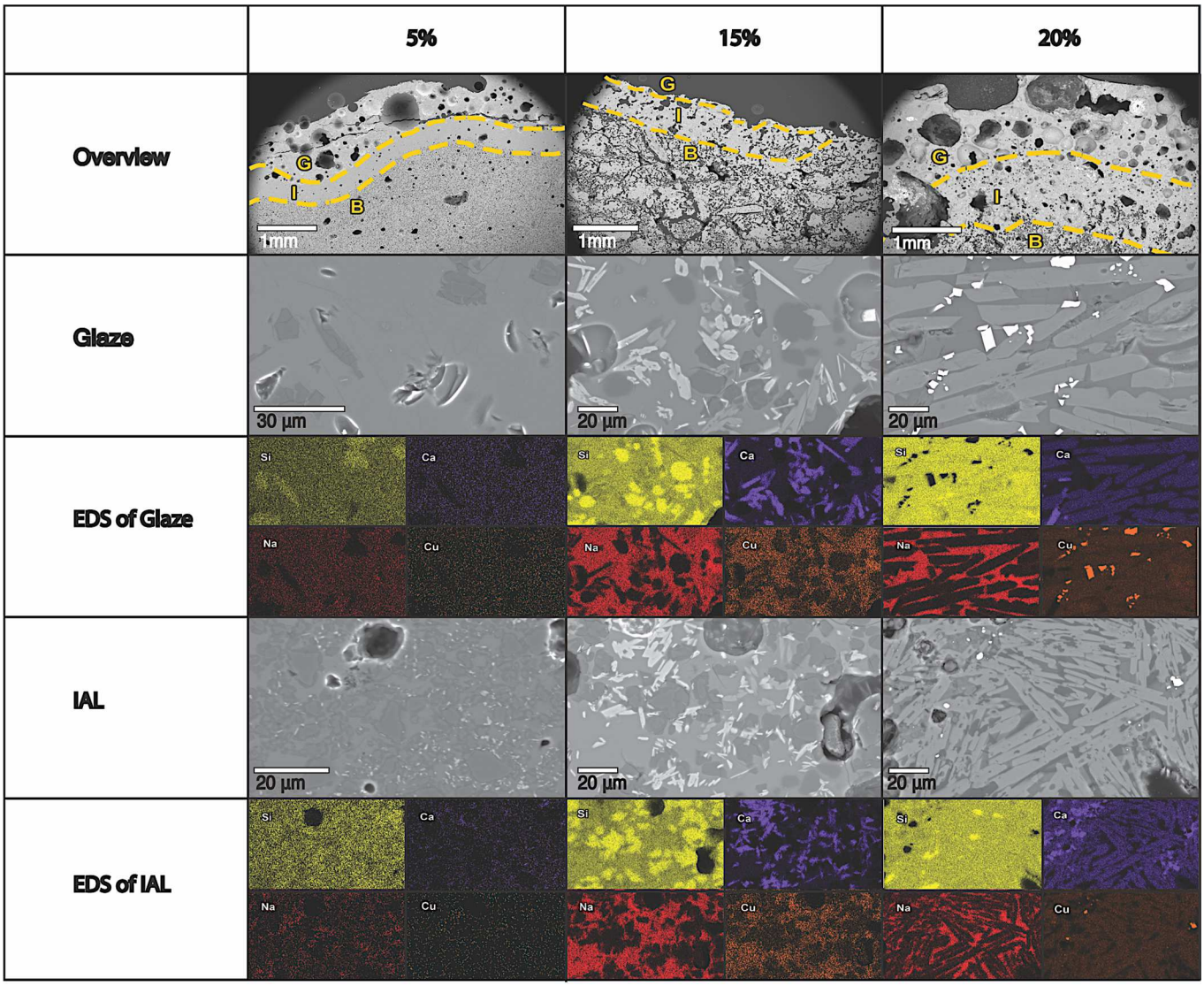

Figure 5. SEM images and elemental maps of polished cross-sections of faience samples prepared with 5, 15, and 20 wt% calcium hydroxide. The sample with 20 wt% calcium hydroxide has a 1:1 molar ratio of Ca:Cu and shows the formation Egyptian blue crystals in the glaze and interaction layer (light gray) as shown by the overlap of calcium, silicon, and copper. Egyptian blue crystals are held together by a glassy phase. In the 5 wt% sample and as the ratio of Ca:Cu increases, the formation of parawollastonite crystals and upon increasing the concentration of calcium to 15% while keeping the concentration of copper oxide the same as the 5 wt% sample, the parawollastonite crystals grow larger.

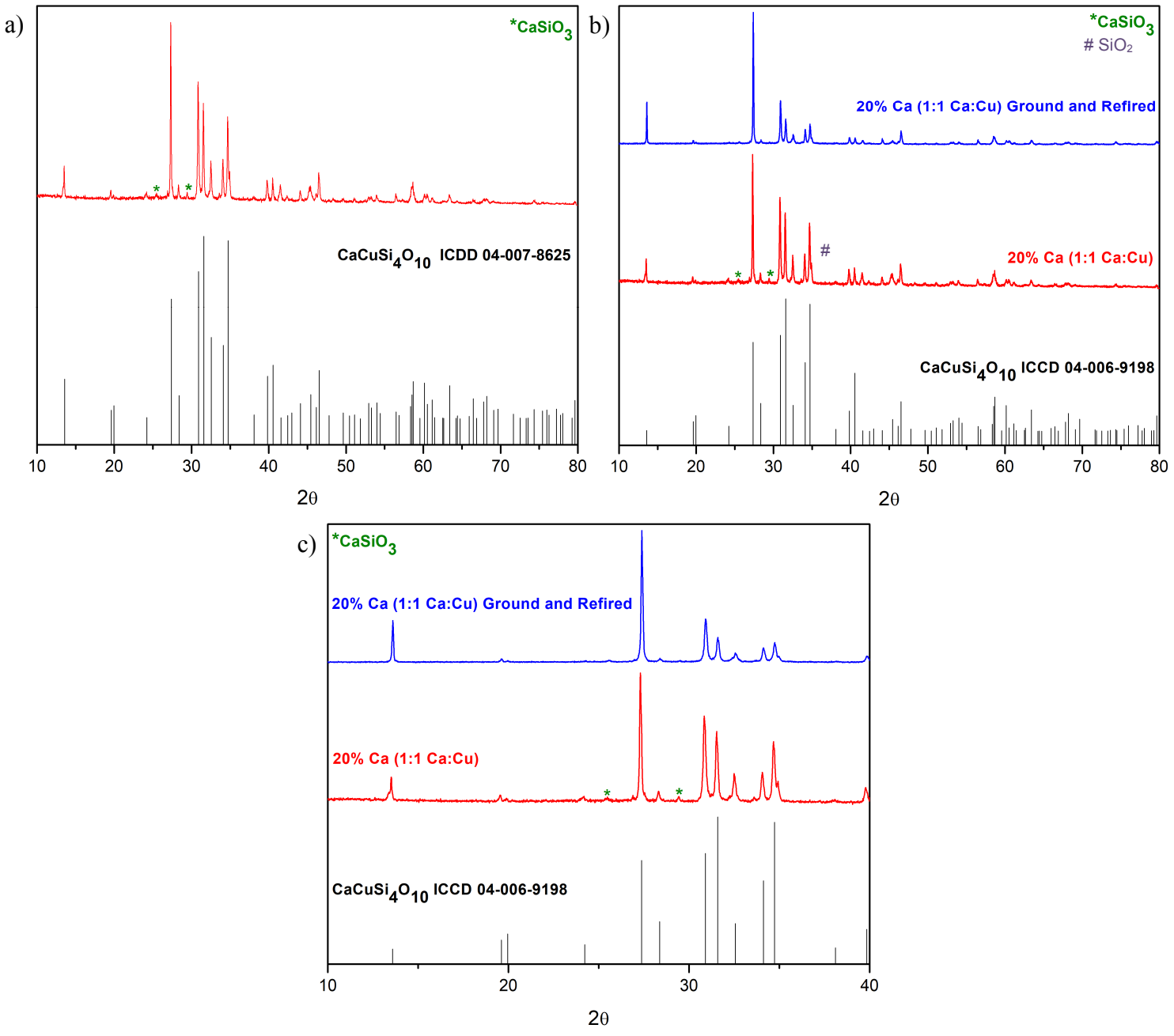

Figure 6. PXRD patterns of a) the faience 20% sample with the 1:1 calcium to copper ratio. The pattern matches calcium copper tetrasilicate or Egyptian blue. The peaks at ~27° and 29.5° 2θ is wollastonite (β-$CaSiO_3$), b) the blue pattern represents the grinding and refiring of the same sample which results in the disappearance of the wollastonite peaks versus the original sample which is represented by the red pattern, and c) a closeup of the PXRD peaks comparing the two patterns and how the wollastonite peaks are affected. There is also an additional peak in the red pattern at ~35° 2θ that also disappeared upon processing of the sample.

Through near-infrared imaging we were also able to demonstrate that luminescence in the faience samples can be tuned by altering the concentration of the calcium and copper source. Near infrared imaging was utilized in this process as a semi-quantitative tool to determine whether Egyptian blue was formed in the core of the faience samples or not. Egyptian blue formed in the faience samples we synthesized and under the conditions we described are difficult to image and quantify under SEM as they are submicron in size.

Figure 7. (a) shows an optical image and corresponding near-infrared luminescence images showing different faience samples with the variable calcium hydroxide concentration as well as varying the concentration of copper oxide at some instances. The sample at 0% displays no near-infrared luminescence due the absence of a calcium source which is required for the formation of Egyptian blue crystals. As the concentration of calcium hydroxide increases to 2 wt%, we started noticing the evolution of luminescence from the sample. In Figure 7., we also prepared two faience samples with 5 wt% calcium hydroxide. The first 5 wt% sample contains a 3.5:1 molar ratio of calcium hydroxide to copper oxide and displays luminescence from the core of the sample. The second faience sample also labeled 5 wt% which is a unique sample that in fact lies in the middle of the faience continuum. This second 5 wt% sample contains a 1:1 molar ratio of calcium hydroxide to copper oxide. Figure 8. shows the optical image and corresponding near-infrared image, SEM image of the core and elemental mapping of the 5 wt% sample. We observed first thing from the optical image that the sample has a blue-green color very reminiscent to the color of faience and a vivid blue color which is close to the color of Egyptian blue. We also noticed from the near-infrared imaging that the luminescence is not just from the core of the sample, but the sample displays luminescence also from the glaze and bottom of the sample as shown in Figure 8.

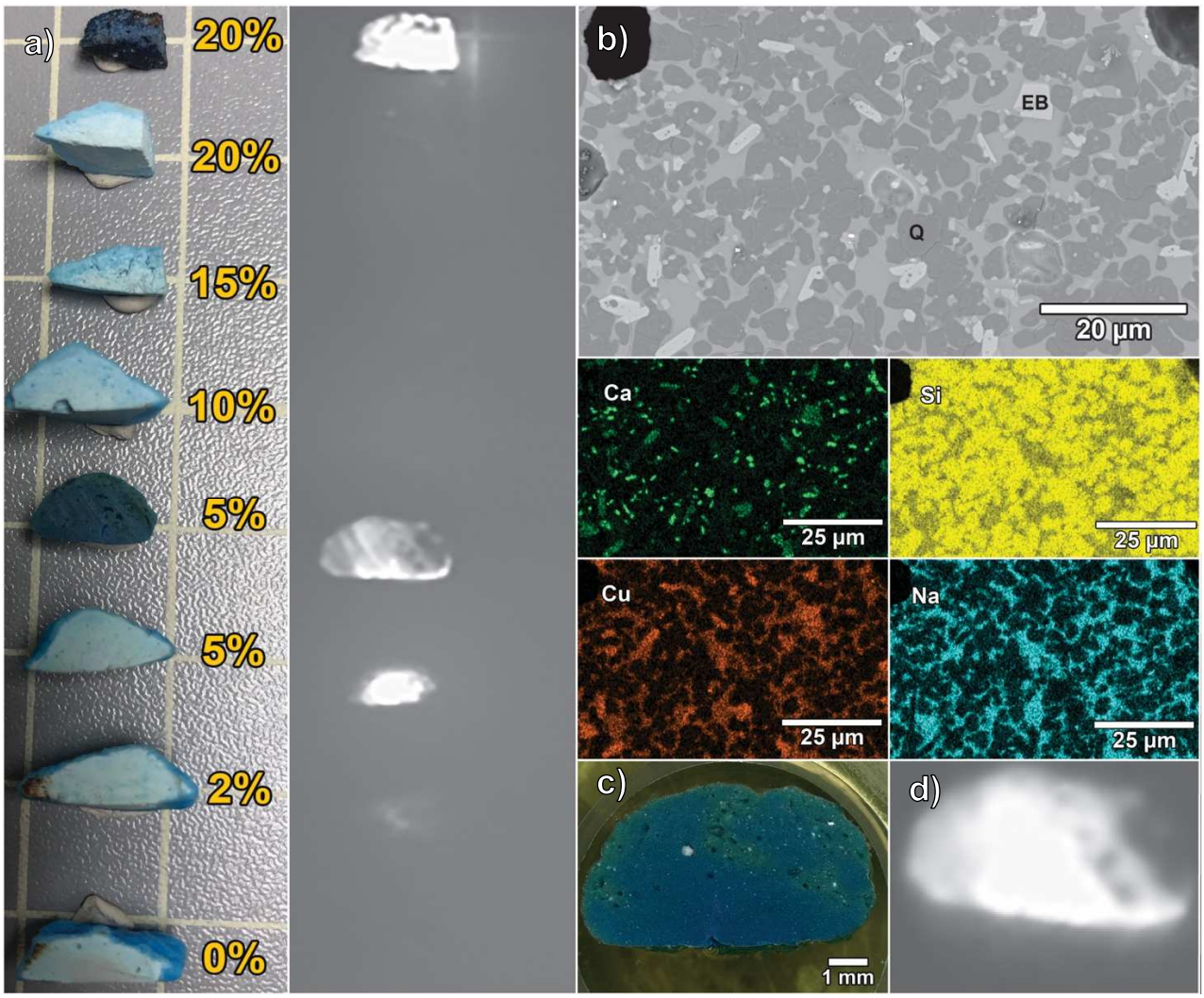

Figure 7. a) Optical image of faience samples prepared with variable concentrations of calcium hydroxide and the corresponding near-infrared luminescence imaging, b) SEM image and corresponding elemental mapping of the 5 wt% sample (molar ratio of Ca:Cu = 1:1), and c) optical microscope image of the same 5 wt% sample and d) corresponding near-infrared image.

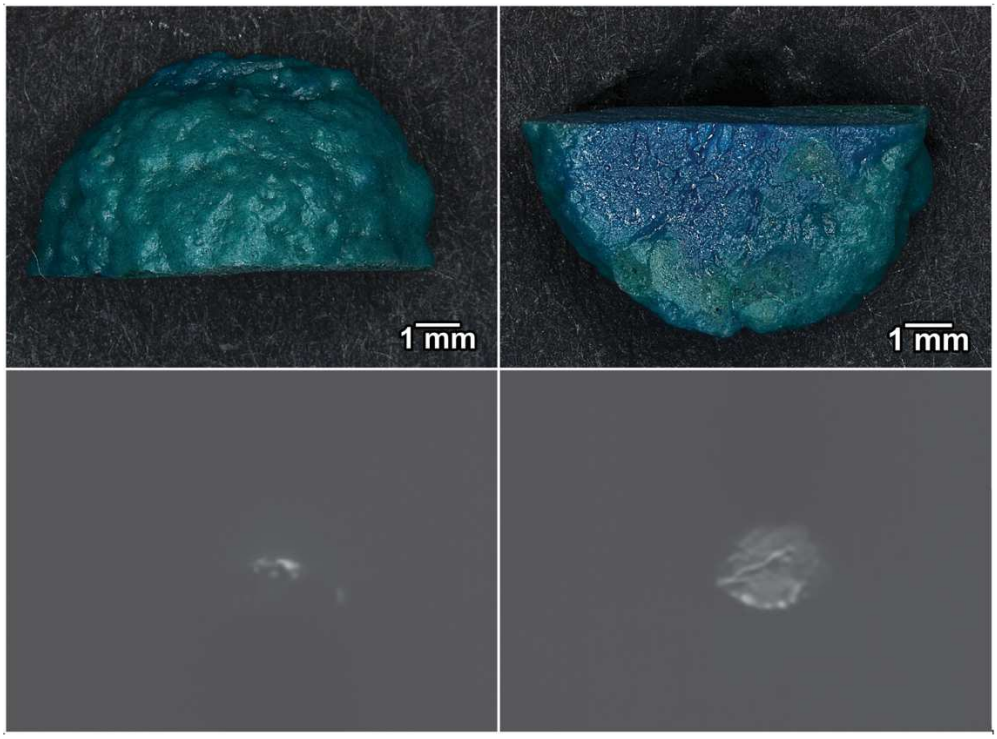

Figure 8. Optical and near-infrared luminescence imaging of the 5% Ca 5% Cu sample. The sample has a unique turquoise colored glaze (left image) and areas with a distinct blue color similar to the color of Egyptian blue (right image). This sample shows luminescence from the glaze portion (image to the bottom right) which we have not noticed before in any of the faience samples in the continuum.

From SEM-EDS evidence (elemental mapping and compositional analysis), this was the first time we observed the growth of Egyptian blue crystals with a length of ~5 μm in a faience core matrix. As a result of the crystal growth of Egyptian blue, the sample is more luminescent in comparison to the 5 wt% sample with 3.5 : 1 ratio of calcium hydroxide to copper oxide. Therefore, we concluded from the 5% Ca 5% Cu sample that just by increasing the copper content in faience samples so that it is equal to the calcium content we can stimulate the growth of Egyptian blue crystals blue crystals. This is a result of the presence of the correct stoichiometry of calcium and copper to form $CaCuSi_4O_{10}$.

Beyond the 5 wt% samples in Figure 7.(a), the luminescence disappears in the samples with 10, 15, and 20 wt% calcium hydroxide concentration. Also, these samples had a rougher looking appearance and texture and do not appear to have a glaze in comparison to the 0, 2, and 5 wt% samples which have a glassy glaze giving a smooth and shiny appearance. Analyses of prehistoric glass reveals the presence of calcium in soda-lime-silica glasses with a composition up to ~8% CaO. Calcium acts as a network stabilizer but, if present in sufficient excess, it tends to increase the melting temperature of glass.[28] Our faience samples were all fired at the same temperature of 930 °C, and it is possible that glaze formation in the 10, 15, and 20 wt% calcium hydroxide samples requires elevated temperatures. The luminescence is once again restored in the 20 wt% sample, Figure 7.(a) first sample to the top, as the concentration of calcium hydroxide : copper oxide is 1:1 along with the silicon dioxide and the flux present forms a sample which is mostly composed of Egyptian blue crystals.

Crystal growth studies of Egyptian blue in Egyptian faience

After establishing the presence of Egyptian blue in our faience samples under certain conditions, such as by controlling the ratio and stoichiometry of calcium and copper reactants, we conducted a crystal growth study of Egyptian blue in faience using two techniques: slow cooling and quenching. For the slow cooling method, we followed two routes. Starting with our original recipe in which the ratio of Ca:Cu is 3.5:1, we applied controlled cooling conditions inspired by the work of Pradell et al.[13] From the SEM in Figure 9., we noticed the presence of Egyptian blue crystals of ~5 μm in size. This can be attributed to the fact the Egyptian blue crystals continue to grow down to ~700 °C. Previously, we were not able to image Egyptian blue using SEM under standard conditions (that is, without controlled cooling). We also applied a similar crystal growth

technique conducted by Johnson-Mc Daniel et al. for the melt flux synthesis of Egyptian blue crystals.[14] This method was applied for the growth of bulk Egyptian blue using melt flux synthesis. Unfortunately, this method did not result in the crystal growth of Egyptian blue. The reason for the larger crystal size from the slow cooling method of Pradell et al. might be that these conditions allow for slower diffusion of the reactants, leading to an increase in crystal nucleation and slower growth rates over a longer period of time.[29]

We also conducted a similar slow cooling experiment with a 1:1 ratio of Ca:Cu (5% Ca, 5% Cu). From our previous experiments with this sample, the crystal size of Egyptian blue was ~5 μm. This time we applied the melt flux synthesis conditions used to grow bulk Egyptian blue crystals reported by McDaniel et al.[14] We noticed from the SEM image in Figure 9., that the size of the Egyptian Blue crystals is about 10 – 20 μm. The difference in the crystal size between the 5% Ca, 5% Cu sample in Figure 7. Synthesized without controlled cooling conditions and the 5% Ca, 5% Cu sample in Figure 9. synthesized using controlled cooling can be explained by the rate by which the sample is cooled. Once again, the equal concentrations of calcium and copper is crucial for growth of large Egyptian blue crystals over the cooling rate of the faience sample.

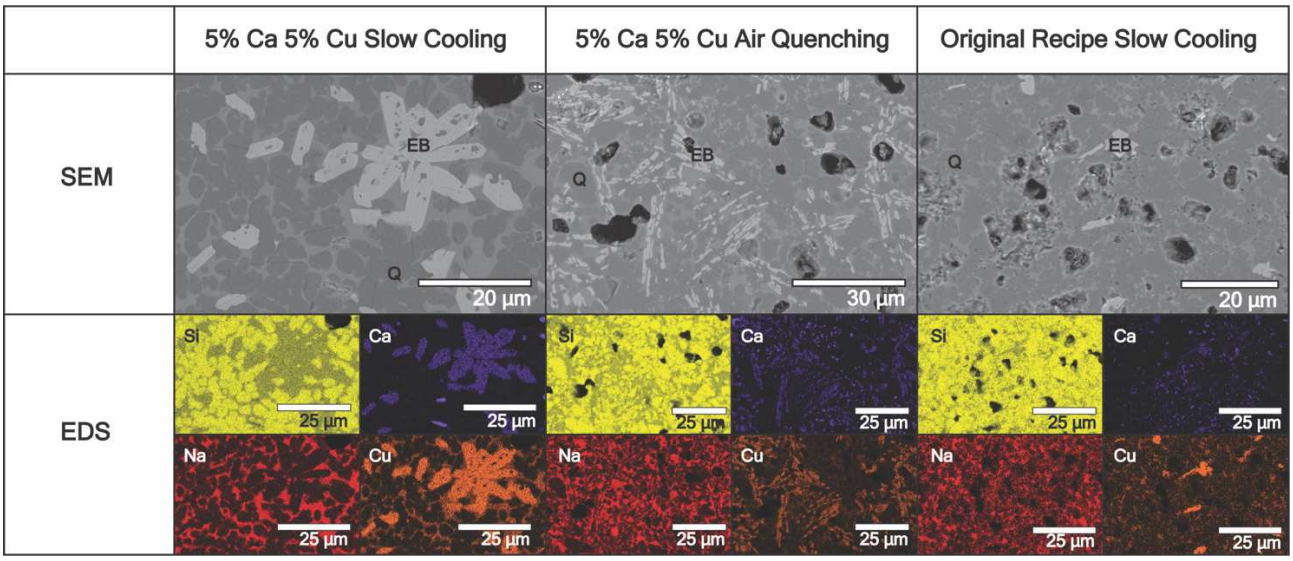

Figure 9. SEM images and corresponding elemental mapping for the Egyptian blue crystal growth in different faience samples using slow cooling and air quenching techniques. The formation of Egyptian blue in the samples is confirmed by the overlap of calcium and copper on the elemental maps. Egyptian blue is labeled EB and quartz grains (dark grey) are labeled Q. The light grey feature in the images is the glassy matrix.

The last crystal growth method we examined is air quenching, which gave crystals of ~5 – 30 µm long. It was interesting to see that the morphology of the crystals that were elongated with a "dotted line" like morphology. This "dotted line" morphology can be explained by the incomplete and lamellar growth of Egyptian blue crystals due to the sudden cooling of the sample to room temperature versus the sample that is slow cooled in which the crystals were given a long time to grow.

Synthesis of Egyptian blue objects

The faience continuum gave us a glimpse of what techniques, starting reactants, and stoichiometries were used to synthesize either faience or Egyptian blue. At the extreme end of the continuum and using the 20 wt% calcium hydroxide sample with a 1:1 calcium to copper ratio we

were able to synthesize Egyptian blue objects. The objects were obtained using a two-step process. The sample obtained from the continuum is a black-grey mass due to the presence of excess copper oxide in the sample and therefore needs further processing through addition of extra alkali flux and quartz plus grinding and refiring to produce an object that has a blue color. Furthermore, a single firing at ~900 °C of bodies formed directly from the raw material mixture leads to fragile structures. This is due to the migration of alkali flux to the surface layer of Egyptian blue leaving the bulk unreacted and greenish color.[30]

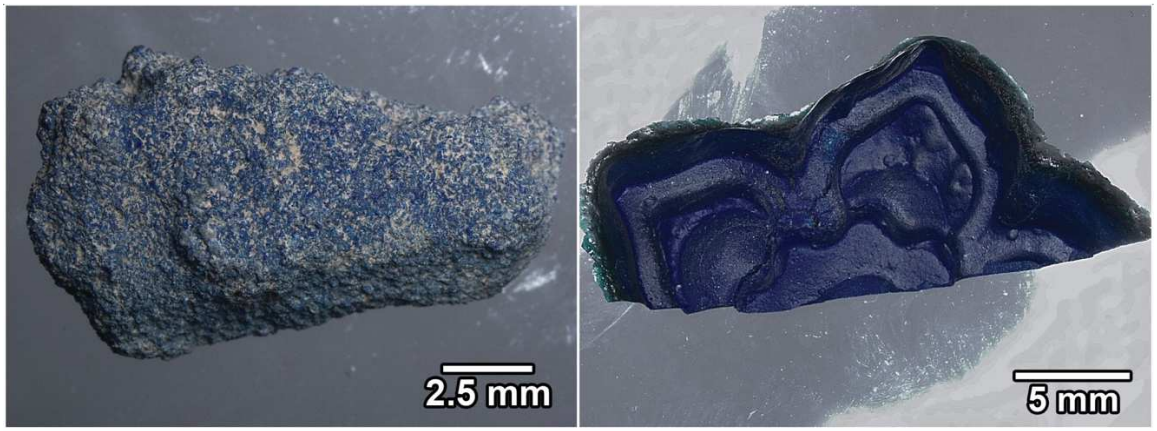

Figure 10. Optical microscope images of an ancient, weathered Egyptian blue object (left image) and a lab synthesized Egyptian blue object (right image).

Figure 10. shows an optical microscope image of a lab synthesized and an ancient Egyptian blue object. There is a clear difference between the surface textures of the two samples. The ancient sample (image to the left) looks grainier than the lab synthesized sample. This is probably due to ball milling and the two-step processing of the sample. The ancient blue sample also appears to have a lighter appearance than the lab synthesized sample perhaps due to multiple factors such as

weathering, different densities of Egyptian blue crystals, glassy phase, quartz, voids as well as different crystal sizes of Egyptian blue.

Using SEM-EDS we were able to quantify and compare the microstructures of the two samples. Figure 11. shows a comparison of polished cross-sections the optical microscope images, SEM images and elemental maps of the two samples. Ancient Egyptian blue objects that were analyzed in the literature were either a light blue color or a dark blue color. This can be explained by the crystal size of Egyptian blue in the sample. Smaller crystals give a lighter blue sample while larger crystals yield darker blue Egyptian blue object.[24, 31] In our case and as confirmed by SEM, the crystal size in the ancient Egyptian blue samples are approximately five times larger than the Egyptian blue crystals in the lab synthesized samples which can be a result of weathering. The crystal size in the lab synthesized sample ranged from ~5 – 20 μm in size while in the ancient sample the crystal size ranges from ~30 – 100 μm. This difference in size can also be explained by the grinding process where comminution using ball milling provided a greater grinding efficiency providing a smaller crystal size versus the ancient sample that was most probably hand ground. From the SEM overview of the two samples, we noticed that both samples look porous.[32] There was less porosity in the lab synthesized Egyptian blue object which can be the result of the presence of a rich glassy phase. In the ancient sample there might be a loss of the porous phase due to weathering and loss of the glassy phase. This was also confirmed by the absence of sodium from the elemental mapping for the ancient sample in comparison with the lab synthesized sample. There is a common feature between the two SEM images of the two samples. From Figure 11., the Egyptian blue crystals nucleate and grow around the quartz particles.

The oxide weight percent for the two samples are provided in Table 2. We found that the oxide percentages for calcium, copper, and silicon oxides were very similar. The elemental

composition also confirms the absence of sodium oxide, which again ca be attributed to weathering of the sample. The presence of aluminum oxide in the lab synthesized sample could be from kaolinite and ball clay. Another possible source is the polishing material, Al_2O_3, when we prepared the polished cross-sections

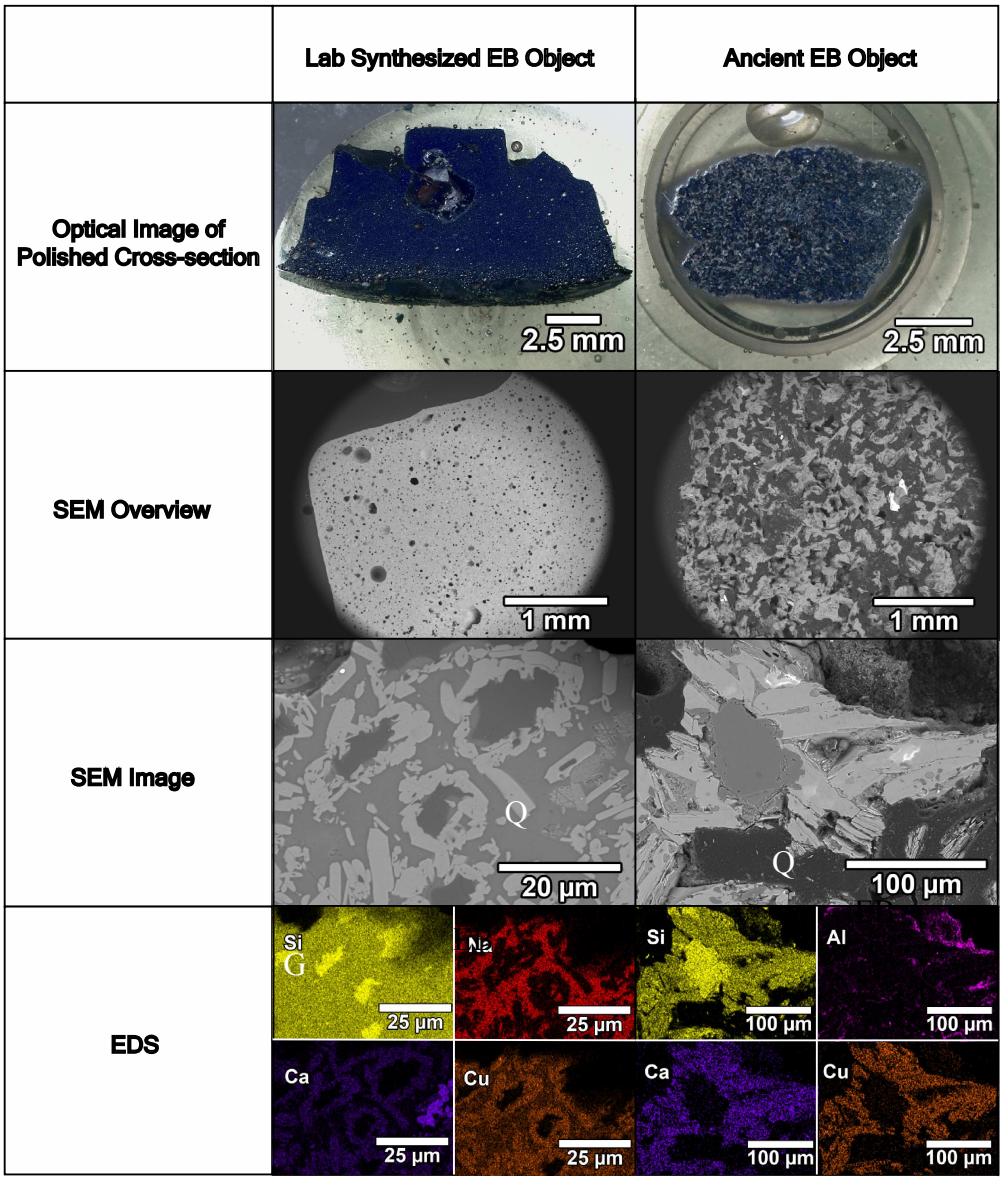

Figure 11. Optical microscope images of polished cross-sections of a lab synthesized and an ancient Egyptian blue objects. The corresponding SEM images and the elemental maps are shown below. Q =Quartz, EB = Egyptian blue, and G = glassy phase.

	SiO_2	CuO	CaO	Al_2O_3	FeO	K_2O	Na_2O
Lab Synthesized EB object	69.0	13.0	9.2	4.0	-	0.3	4.4
Ancient EB object	63.0	15.0	10.6	8.5	1.8	0.5	-

Table 2. Oxide wt% of the lab synthesized and ancient Egyptian blue objects shown in Figure 11.

Conclusion

In this work we have discovered the in-situ formation of Egyptian faience in Egyptian faience by excluding sodium chloride from the flux components. The presence of sodium chloride causes the formation of wollastonite or parawollastonite, which are calcium silicate polymorphs, and they are the main components of Egyptian green pigment. We also found that the formation of Egyptian blue pigment and the morphology of the faience is influenced by the grinding process. Ball milling provides a more uniform faience macroscopic morphology and in turn results in the formation of more Egyptian blue crystals, as evidenced by near-infrared luminescence imaging.

This work established a strong connection between Egyptian blue and Egyptian faience as they have similar elemental components. We created a continuum between Egyptian faience and Egyptian blue by tunning the concentration of calcium hydroxide and copper oxide in some instances. We obtained faience on one end of the continuum and Egyptian blue on the other extreme. We quantified the changes in the microstructures in the samples of the continuum using SEM and evaluated NIR emission through visible induced luminescence imaging. In addition, we

synthesized a sample that is a hybrid of faience and Egyptian blue by using 5% calcium hydroxide and 5% copper oxide in our faience original recipe. This unique samples lies in the middle of the continuum. This sample also allowed us to image and identify in situ-formed Egyptian blue crystals using SEM for the first time.

Crystal growth studies of Egyptian blue were also conducted in faience using either slow cooling with or without manipulation of stoichiometry or air quenching. We noticed that these crystal growth techniques resulted in Egyptian blue crystals of a size range of ~5 – 20 μm in size which is a further proof that the two systems are related and even can co-exist together.

Finally, we were able to synthesize Egyptian blue objects also using the continuum. By processing the 20% calcium hydroxide sample containing a calcium to copper ratio of 1:1 and by addition of quartz, alkali, binders, grinding and refiring the objects, we found that we obtained the objects. We also compared our Egyptian blue object to an ancient sample, and we found that the compositions of both samples are close. Overall, we have established a relationship between Egyptian faience and Egyptian blue which provides an insight on the possible techniques and raw materials used in ancient times.

References

1. Tite, M., A. Shortland, and S. Paynter, *The beginnings of vitreous materials in the Near East and Egypt.* Accounts of chemical research, 2002. **35**(8): p. 585-593.
2. Ragai, J., *Colour: its significance and production in Ancient Egypt.* Endeavour, 1986. **10**(2): p. 74-79.
3. Berke, H., *The invention of blue and purple pigments in ancient times.* Chemical Society Reviews, 2007. **36**(1): p. 15-30.
4. La Delfa, S., V. Formisano, and E. Ciliberto, *Laboratory production of Egyptian faiences and their characterization.* Journal of cultural Heritage, 2008. **9**: p. e113-e116.
5. Tite, M.S., P. Manti, and A.J. Shortland, *A technological study of ancient faience from Egypt.* Journal of Archaeological Science, 2007. **34**(10): p. 1568-1583.
6. Tite, M.S., I.C. Freestone, and M. Bimson, *Egyptian faience: an investigation of the methods of production.* Archaeometry, 1983. **25**(1): p. 17-27.
7. Rehren, T., *A review of factors affecting the composition of early Egyptian glasses and faience: alkali and alkali earth oxides.* Journal of Archaeological Science, 2008. **35**(5): p. 1345-1354.
8. Noble, J.V., *The technique of Egyptian faience.* American journal of archaeology, 1969. **73**(4): p. 435-439.
9. Riccardelli, C., J. Mass, and J. Thornton, *Egyptian Faience Inlay Techniques: a process for obtaining detail and clarity by refiring.* MRS Online Proceedings Library (OPL), 2002. **712**.

10. Liang, H., et al., *Optical Coherence Tomography for the non-invasive investigation of the microstructure of ancient Egyptian faience.* Journal of Archaeological Science, 2012. **39**(12): p. 3683-3690.

11. Moussa, A. and M.F. Ali, *Color alteration of ancient Egyptian blue faience.* International Journal of Architectural Heritage, 2013. **7**(3): p. 261-274.

12. Mirti, P., et al., *Spectrochemical and structural studies on a Roman sample of Egyptian blue.* Spectrochimica Acta Part A: Molecular and Biomolecular Spectroscopy, 1995. **51**(3): p. 437-446.

13. Pradell, T., et al., *Physical processes involved in production of the ancient pigment, Egyptian blue.* Journal of the American Ceramic Society, 2006. **89**(4): p. 1426-1431.

14. Johnson-McDaniel, D. and T.T. Salguero, *Exfoliation of Egyptian blue and Han blue, two alkali earth copper silicate-based pigments.* JoVE (Journal of Visualized Experiments), 2014(86): p. e51686.

15. Giménez, J., et al., *Effect of NaCl on the fabrication of the Egyptian blue pigment.* Journal of Archaeological Science: Reports, 2017. **14**: p. 174-180.

16. Bloise, A., et al., *Flux growth and characterization of cuprorivaite: the influence of temperature, flux, and silica source.* Applied Physics A, 2016. **122**(7): p. 1-8.

17. Pagès-Camagna, S. and S. Colinart, *The Egyptian green pigment: its manufacturing process and links to Egyptian blue.* Archaeometry, 2003. **45**(4): p. 637-658.

18. Harris, K.D., *How grinding evolves.* Nature chemistry, 2013. **5**(1): p. 12-14.

19. Yang, H.K. and J.H. Jeong, *Synthesis, crystal growth, and photoluminescence properties of YAG: Eu3+ phosphors by high-energy ball milling and solid-state reaction.* The Journal of Physical Chemistry C, 2010. **114**(1): p. 226-230.

20. Sadykov, V.A., et al., *Advanced materials for solid oxide fuel cells and membrane catalytic reactors.* Advanced nanomaterials for catalysis and energy, 2019: p. 435-514.

21. Tite, M. and M. Bimson, *Faience: an investigation of the microstructures associated with the different methods of glazing.* Archaeometry, 1986. **28**(1): p. 69-78.

22. Fontana, R., et al., *Notes on Vestorius' Blue–New findings and investigations.* Journal of Cultural Heritage, 2020. **45**: p. 370-378.

23. Hatton, G.D., A.J. Shortland, and M.S. Tite, *The production technology of Egyptian blue and green frits from second millennium BC Egypt and Mesopotamia.* Journal of Archaeological Science, 2008. **35**(6): p. 1591-1604.

24. Oudbashi, O. and M. Hessari, *A "Western" imported technology: an analytical study of the Achaemenid Egyptian blue objects.* Journal of Cultural Heritage, 2021. **47**: p. 246-256.

25. Panagopoulou, A., K. Karanasios, and G. Xanthopoulou, *Ancient Egyptian Blue (CaCuSi4O10) pigment by modern solution combustion synthesis method.* Eurasian Chemico-Technological Journal, 2016. **18**(1): p. 31-37.

26. Grifa, C., et al., *Beyond Vitruvius: new insight in the technology of Egyptian blue and green frits.* Journal of the American Ceramic Society, 2016. **99**(10): p. 3467-3475.

27. Kostomitsopoulou Marketou, A., et al., *Egyptian Blue pellets from the first century BCE workshop of Kos (Greece): Microanalytical investigation by optical microscopy, scanning electron microscopy-X-ray energy dispersive spectroscopy and micro-Raman spectroscopy.* Minerals, 2020. **10**(12): p. 1063.

28. Henderson, J., *The raw materials of early glass production.* Oxford Journal of Archaeology, 1985. **4**(3): p. 267-291.

29. Hou, F., *Open questions on physical chemistry of crystal growth from congruent melts.* Communications Chemistry, 2021. **4**(1): p. 1-3.

30. Wiedemann, H.-G. and H. Berke, *Chemical and physical investigations of Egyptian and Chinese blue and purple.* Monuments and Sites, 2001. **3**: p. 154-171.

31. Nicola, M., et al., *Late production of Egyptian blue: synthesis from brass and its characteristics.* Archaeological and Anthropological Sciences, 2019. **11**(10): p. 5377-5392.

32. Tite, M.S. and G. Hatton, *The production technology of, and trade in, Egyptian blue pigment in the Roman world.* Communities and Connections: Essays in Honour of Barry Cunliffe, 2007: p. 75-92.

CHAPTER 4

INVESTIGATION OF DIFFERENT RAW MATERIALS USED FOR MANUFACTURING EGYPTIAN FAIENCE AND THEIR CORRELATION TO THE IN-SITU SYNTHESIS OF EGYPTIAN BLUE

Introduction

Faience produced in the Near East and Egypt prior to the Roman period was based on silica as the network former, soda as the alkali flux, lime and magnesium oxide as the stabilizers that limit solubility and initially, copper oxide as a colorant.[1]

Quartz

There were two possible sources of silica: ground quartz and quartz sand. Ground quartz contained very few impurities and was characterized by, low alumina, lime, and iron oxide content therefore not significantly altering the composition of the synthesized faience. The presence of quartz was characterized by angular particles in the faience microstructure. On the other hand, quartz sand can introduce elements such as calcium and aluminum from limestone or shell fragments and alumina respectively.[2] The morphology of the quartz sand particles tend to be rounded rather than angular.[3]

Alkali Flux

The purpose of the flux is to allow the partial melting of the silica at lower temperatures. In this way, the silica grains become cemented together to give faience its physical strength.[4] Two principal sources of alkali flux used for Egyptian Faience were Natron and plant ashes. Natron is a natural evaporite which comes from the most well-known source Wadi Natrum on the edge of the Western Desert of Egypt. Natron predominantly consists of sodium carbonate and sodium bicarbonate and is characterized by low potash, lime, and magnesia content. Little was known about the preparation of natron for faience manufacturing, but it was assumed that it had been crushed to a fine powder and any impurities such as plant debris removed from it.[5,6] In 1969, Noble analyzed ancient Natron sample and found that sodium chloride, sodium sulfate, silica, sodium bicarbonate, sodium carbonate, calcium carbonate and minor components of magnesium carbonate, aluminum oxide, and iron oxide.[7]

Soda-rich ashes derived from halophytic plants were used as the flux in the production of glazes on small objects made from quartz, steatite, and faience.[8] The plant ash is characterized by the potash content which is a little bit higher than soda, and by low lime and magnesia content. The soda-rich and mixed alkali plant ashes are salt resistant, halophytic plants growing in costal, salt marsh, and desert regions, or seaweeds. Salt resistant is a plant's ability to avoid, by means of salt regulation, excess amounts of salt reaching the living cell or tolerating the toxic effects associated with increased ion concentration. The *Chenopodiaceae* plant family, .which consists of 1300 species in 120 genera which is found around the world especially in desert and semi-desert regions. *Chenopodiaceae* Family has several genera such as *Suaeda*, *Salsola*, *Salicornia* which are obligate halophytes that are absent from areas with low salinity.[9,10] The factors that determine the composition of plant ash include the plant species, the stage in the growing season, components of

the plants such as the woody parts and leaves, composition of soil and water and finally the way the way they were ashes were prepared.[11] Plant ashes prepared at temperatures between 500 – 1300 °C show evidence of partial loss of the potash component through volatilization between a temperature of 800 – 900 °C while the soda component seems to be less susceptible to volatilization in this temperature range.[12]

Lime and Magnesium oxide

The use of lime is well known in the manufacture of faience and its percentage in the faience body is estimated between 1 to 5%. Lime could have been obtained from the burning of limestone which has a main composition of calcium carbonate or dolomite which consists of a calcium magnesium carbonate.[4] Another possible source of lime is the desert sands in Egypt which might have been an accidental source due to the presence of a high proportion of limestone grains in the sand. In addition, it has been also mentioned in the literature that burned shells may have been a convenient source of lime.[13] There has also been a few reports hinting towards the use of gypsum or hydrated calcium sulfate as a possible source of calcium. Gypsum has been used as a mortar in ancient Egyptian masonry practices.[14] A source of magnesium oxide might have been from the alkali flux or dolomite.

Copper colorant

The main form of copper colorant used in ancient Egyptian faience is copper(II) oxide which can be obtained by the decomposition of malachite or azurite during the manufacture of the glaze. It has also been hypothesized that Egyptian blue pigment was also used as a source of copper.[15] Egyptian blue balls were prepared and added to the frit to impart color to the faience. The

preparation of Egyptian blue balls and their application to the faience mixture versus the addition of a copper source directly provided more control and precision over the color. Another potential source of copper coloring material is bronze scrap with ~10% tin content. It was suggested that the faience workers were obtaining bronze waste from the metal smiths or were recycling domestic metal scrap.[4]

Substrates and slip layers for firing Egyptian faience

Several reports in the literature exist confirming that faience objects were laid on supports to separate faience objects fired at the same time from each other before they were fired in kilns to ensure that the glaze layer would not be damaged. These supports were often lined with clay or marl clay mixed with limestone powder to facilitate the easy removal of the objects after firing.[16,17] It was also possible that the supports were lined using a rich layer of lime or CaO and this was confirmed by the analysis of faience objects and the high CaO content.[1]

Herein, we provided an investigation using different sources of raw materials and their effect on the faience macroscopic morphology, microstructures, and the in-situ synthesis of Egyptian blue.

Experimental

4. Visible-induced luminescence imaging

Faience samples were illuminated with a red LED light array (LEDLB-24-RED/BLUE-F-BLACK, 72 Watts - 9~42 VDC, Larson Electronics LLC) and imaged using a Xenics Bobcat 320-GigE Vision 100 Hz camera (0.9 to 1.7 μm imaging range). Images were post-processed using

Adobe Photoshop CC 2018; specifically, the dimensions of the images were adjusted to a width of 1500 and then cropped, and the luminescence was false-colored for clarity.

5. Laboratory sample preparation

Materials: Quartz pebbles (obtained from the Department of Geology, University of Georgia) were pre-ground using a Fritsch Pulverisette 6 planetary ball mill (using ~30, 10 mm silicon nitride grinding balls in a 80 mL silicon nitride milling bowl) at 450 rpm for 30 min. Kaolinite, Na_2CO_3 (anhydrous powder, 99.999% trace metal basis), $Ca(OH)_2$ (ACS reagent, ≥95.0% purity), $CaCO_3$ (BioXtra, ≥99.0% purity), $NaHCO_3$ (BAKER ANALYSED™ A.C.S reagent, JT Baker™), $CaSO_4 \cdot 2H_2O$ (ACS Reagent, 98% purity), sodium tetraborate decahydrate ($Na_4B_4O_7 \cdot 10H_2O$ ACS reagent, ≥95.0% purity), $Cu_2CO_3(OH)_2$ (regent grade), and CuO (99.99% trace metal basis), and were purchased from Sigma-Aldrich. CaO was prepared by firing $CaCO_3$ in a box furnace at 1000 °C for 12 h. $CaSO_4 \cdot 2H_2O$ has been dehydrated by heating at 160 °C for 12 h in a box furnace. Additional materials include ball clay (obtained from the Ceramics program, Lamar Dodd School of Art, University of Georgia) and commercial gum Arabic (Jacquard brand, "pure *Acacia Senegal* and *A. Arabica*").

Preparation of plant ashes: plant ashes were prepared according to the method described by Tite et al.[10] Italian agretti (*Salsola Soda)* plant ashes were prepared as follows. The plant (leaves and stems) was harvested and left to air dry on a bench top in the laboratory for a week. The dried product was weighed (21.65 g) and then transferred to a porcelain crucible and ignited at 300°C for 1 hour in a small box furnace. The resultant ashes were ground in the same porcelain dish using a porcelain pestle and then fired again at 600°C for 10 hours during which the ashes were taken

out periodically, ground up and refired. The end product weighed 1.56 g and was in the form of an off-white powder.

Faience preparation (efflorescence method): 0.750 g (12.5 mmol) of pre-ground quartz, 0.0500g (0.194 mmol) of kaolinite, 0.0500 g of ball clay, 0.0500 g (0.472 mmol) of Na_2CO_3, 0.0500 g (0.675 mmol) of $Ca(OH)_2$ or 0.0675 g (0.675 mmol) of $CaCO_3$ or 0.0378 g (0.675 mmol) of CaO or 0.919 g (0.675 mmol) $CaSO_4$, 0.0500 g (0.595 mmol) of $NaHCO_3$, 0.0107 g of gum Arabic, and 0.0150 g (0.188 mmol) of CuO were ground together using a Fritsch Pulverisette 6 planetary ball mill (using ~30, 10 mm silicon nitride grinding balls in a 80 mL silicon nitride milling bowl) at 300 rpm for 30 min. The resulting grey powder was mixed with 216 μL of distilled water to form a paste, which then was molded into a ~10×2.5 mm soft pellet. This material was placed on a substrate (alumina, terracotta, or calcium oxide) and allowed to effloresce overnight. Then the sample/substrate was transferred to a box furnace and fired at 930 °C (heating ramp of 15 °C/min) for 12 h. The furnace was allowed to cool down naturally. The product pellet easily separates from the substrate.

Faience preparation using Egyptian blue as a colorant (application glazing method): Preparation of this sample involves a two-step process. In the first step, the body of the sample is prepared and fired to obtain a sintered body. The second step involves preparation and application of the glaze to the sintered mass in first step.

Step 1: 0.750 g (12.5 mmol) of pre-ground quartz, 0.0500g (0.194 mmol) of kaolinite, 0.0500 g of ball clay, 0.0500 g (0.675 mmol) of $Ca(OH)_2$, and 0.0107 g of gum Arabic were ground together using a Fritsch Pulverisette 6 planetary ball mill (using ~30, 10 mm silicon nitride grinding balls

in a 80 mL silicon nitride milling bowl) at 300 rpm for 30 min. The resulting white powder was mixed with distilled water added dropwise until a paste is formed, which then was molded into a ~10×2.5 mm soft pellet. This material was placed on an alumina substrate and allowed to dry overnight. Then the sample/substrate was transferred to a box furnace and fired at 930 °C (heating ramp of 15 °C/min) for 12 h. The furnace was allowed to cool down naturally. The product pellet easily separates from the substrate.

Step 2: 0.200 g (3.33 mmol) of pre-ground quartz, 0.0500 g (0.595 mmol) of $NaHCO_3$, 0.0500 g (0.472 mmol) of Na_2CO_3, and 0.142 g (0.282 mmol) $CaCuSi_4O_{10}$ were ground together using a Fritsch Pulverisette 6 planetary ball mill (using ~30, 10 mm silicon nitride grinding balls in a 80 mL silicon nitride milling bowl) at 300 rpm for 30 min. The resulting light blue powder was mixed with distilled water added dropwise until a slurry is formed which is then applied to the sintered quartz body in step one using a Teflon spatula. This material was placed on an alumina substrate and allowed to dry overnight. Then the sample/substrate was transferred to a box furnace and fired at 930 °C (heating ramp of 15 °C/min) for 12 h. The furnace was allowed to cool down naturally. The product pellet easily separates from the substrate.

Preparation of Egyptian blue pigment (melt flux synthesis): the procedure was adapted from Johnson-McDaniel et al.[18] 0.133 g (1.33 mmol) of $CaCO_3$, 0.320 g (5.32 mmol) of SiO_2, 0.106 g CuO (1.33 mmol), and 12.5% by weight (0.0698 g) sodium tetraborate decahydrate, or natron, or *Salsola Soda* plant ashes are transferred to an agate mortar and pestle and ground into a fine powder. Then the powder reactants are transferred to a platinum crucible and heated in a box furnace at a ramp rate of 2 °C/min to 875 °C, and then dwell for 16 h at 875 °C, then cooled at a rate of 0.8 °C/min. For acid treatment, the crystals were soaked overnight in ~15 mL 1M nitric

acid. After being soaked in acid, they are washed twice with deionized water and decanted then dried in a vacuum oven overnight.

6. Material characterization

Sample preparation: Faience was cut using a Buhler IsoMet™ low speed precision saw. Samples were mounted (with exposed cross section) in a mixture of 2:1 Buhler EpoThin™ epoxy:hardener, then allowed to set for 24 h. Then each epoxy puck was transferred to a Hilloquest thin section machine to further expose the material's cross-section. Then each puck was transferred to a glass plate where it was hand-polished for 15 min using 600 μm grit silicon carbide powder and 15 min using 1000 μm grit silicon carbide powder. This was followed by transferring each epoxy puck to a Buhler MiniMet™ 1000 grinder polisher, where they were polished using 5 μm grit for 80 min and 1 μm grit for 80 min.

Optical microscopy: Samples were examined using a Leica DVM6 digital microscope with a 3664 x 2748-pixel camera using a low magnification objective (190x magnification). Illumination source was a ringlight LED array. Z-stacking was used for pellet cross-section.

SEM/EDS: Polished cross sections were coated by approximately depositing a 200 Å layer of carbon using a JOEL JEE-4x vacuum evaporator. Samples were examined by scanning electron microscopy (SEM) with an FEI Teneo FE-SEM, operating at 10 keV and using a spot size of 10. Energy-dispersive spectroscopy (EDS) data were collected with an integrated Oxford Instruments X-MAX^N detector operated at 5-10 keV. The EDS results are an average of three different spots/areas. The dimensions of the images have an average of height of 55.63 μm and average width of 83.51μm.

Powder X-ray diffraction (PXRD): Powder X-ray diffraction (PXRD) was conducted on the powder sample using a Bruker D8 instrument with a Co-Kα X-ray source ($\boldsymbol{\lambda} = 1.78890$ Å) operated at 35 kV and 40 mA. The data were collected from 10 to 80° 2θ at a scan rate of 0.1 s/step.

Results and Discussion

In our investigation we attempted the replication of faience using the efflorescence synthesis method using different sources of calcium, copper, flux sources, and substrates while monitoring the formation of Egyptian blue via near-infrared luminescence imaging as well as the changes in the morphology and faience microstructures using SEM.

Replication of Egyptian faience using different calcium sources

In our original work, we used calcium hydroxide as the source of calcium for the synthesis of faience. To try and emulate the synthesis of faience in ancient times, we attempted to use laboratory grade chemicals containing calcium that are related to limestone, dolomite, or gypsum. For example, calcium carbonate is the main component in limestone, dolomite, or even shell fragments when quartz sand was used as a source of silica. Figure 4.1 shows the optical microscope images of polished cross-sections and corresponding near-infrared images of four laboratory faience replicates using calcium hydroxide, calcium carbonate, calcium sulfate (main component of gypsum), and calcium oxide. Figure 4.2 shows an optical microscope image of a faience sample synthesized using CaO powder and it does not display near-infrared luminescence.

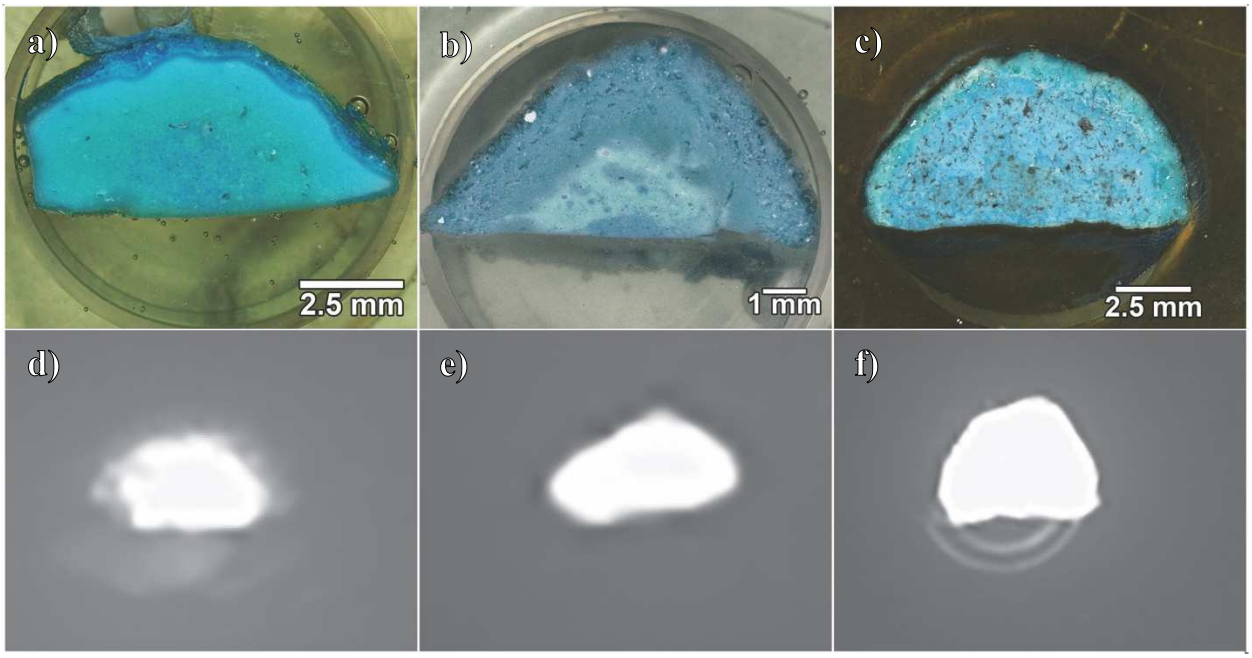

Figure 4.1 Optical microscope images of Egyptian faience synthesized using different calcium sources a) calcium hydroxide, b) calcium carbonate, and c) gypsum. The corresponding near-infrared images (d-f) are displayed below. The three samples display near-infrared luminescence confirming the presence of Egyptian blue in the sample core.

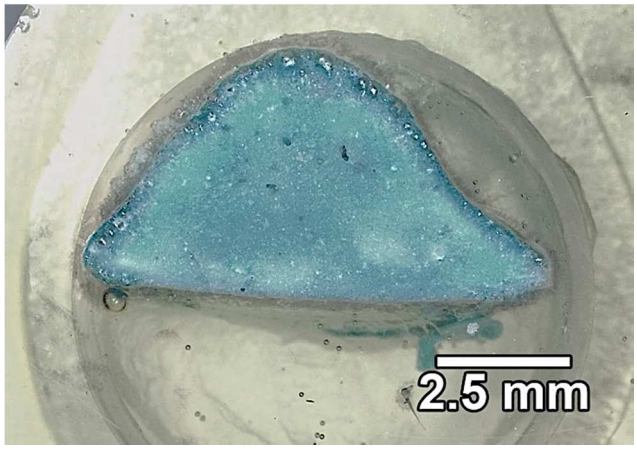

Figure 4.2 Optical microscope images of Egyptian faience synthesized using different calcium oxide as a copper source. The sample does not display near-infrared luminescence.

From figure 4.1 and 4.2, the faience samples shown have blue colored cross-sections which gave us an idea about the diffusion of ions particularly Cu^{2+}. Soda flux decomposes at ~760 °C forming a eutectic mixture with quartz giving rise to a liquid phase that covers and consumes the

quartz crystals. The first ion to diffuse into this liquid phase is Cu^{2+}, possibly from the glaze to the body which explains the blue color throughout the faience samples. The Cu^{2+} ions also form an amorphous coating around the quartz crystals at ~900 °C.[19]

Figure 4.3 shows the microstructures of the samples prepared and table 1. shows the weight percent oxide of the four faience samples prepared from the four different calcium sources. There are multiple distinct features that can be noticed from the microstructures of the four samples in the SEM images. First, we noticed with all the samples the formation of calcium silicate which is characterized by the formation of rod or needle like crystals of sizes varying from ~1 – 10 μm. The presence of calcium silicate occurs specifically in the interaction layer (IAL) and the body of the faience. However, in the faience sample prepared from calcium sulfate and in addition to calcium silicate, we noticed the formation of micron-sized Egyptian blue crystals (Figure 4.4). Previously, we have noticed the growth of Egyptian blue in the faience core under two conditions: either using controlled cooling or in samples with calcium and copper having the same stoichiometry. In this case the appearance of micron-sized Egyptian blue seemed unusual.

We attempted to analyze and form a hypothesis to answer two questions: 1) Why did the sample synthesized with calcium oxide as a source of calcium did not luminesce and 2) why the sample with calcium sulfate had micron-sized Egyptian blue crystals. To answer the first question, calcium silicate and its polymorphs form and are stable at a temperature range of 950 – 1150 °C while Egyptian blue forms and is stable within the range of 870 – 1050 °C.[19] The presence of CaO in the reaction is imperative for formation of both the glassy crystalline phases in faience. At ~950 °C, Ca^{2+} ions start diffusing and the crystallization of the calcium silicate through precipitation has a high nucleation rate at this temperature, therefore there is an abundance of the needle or rod-like crystals in the faience body.

With the temperature parameters for the formation of the crystalline phases and presence of CaO as a starting material in mind, we formulated a theory about the faience sample synthesized with calcium oxide. The temperature at which our faience samples are fired are at is 930 °C which is high enough of a temperature to form both calcium silicate and Egyptian blue but due to the presence of the highly reactive of calcium oxide in addition high temperature is consumed completely to produce calcium silicate polymorphs. Also, the presence of CaO as a starting material rather than being formed because of the thermal decomposition of calcium carbonate seemed to enhance the growth of the calcium silicate needled. On the other hand, the thermal decomposition of calcium sulfate occurs at a temperature of ~1050 - 1150 °C.[20] Therefore, 930 °C which is our synthesis temperature was not high enough for the formation of calcium oxide. We still noticed the formation of calcium silicate, but they were extremely smaller in size compared to the samples synthesized using calcium carbonate and calcium hydroxide. We attempted to synthesize faience at 1100 °C (Figure 4.5), in the range at which calcium sulfate decomposes to give CaO but we ended up with a green sample that does not luminesce. This could be a result of the decomposition of Egyptian blue at this temperature. In this sample we noticed that there were calcium silicate crystals in the size range of ~10 – 30 μm. We also noticed the formation of acicular crystals as well which is the high temperature polymorph of silicon dioxide formed at ~1000 °C. These observations were very reminiscent of archaeological Egyptian green frit samples.[19,21] We also noticed that this sample formed a glaze which is probably due to the presence of calcium oxide which we have not noticed in the original sample.

Calcium carbonate decomposes at a temperature ~800 °C[22] to give calcium oxide and carbon dioxide therefore allowing the formation of the calcium silicate polymorph and Egyptian blue and not calcium silicate solely. Calcium hydroxide decomposes at ~580 °C but its

decomposition follows a more complex route depending on the vapor pressure of water in the atmosphere, therefore again we noticed that both Egyptian blue and calcium silicate formed.[23] Therefore it can be concluded that for the synthesis of archaeological glasses, glazes or faience and in turn Egyptian blue could possibly be limestone which contains calcium hydroxide, or calcite in which calcium carbonate is a main component. Calcium oxide would have not been an ideal choice as it requires high temperatures to obtain it from calcium carbonate or even gypsum due to the scarcity of fuels in ancient Egypt.[14]

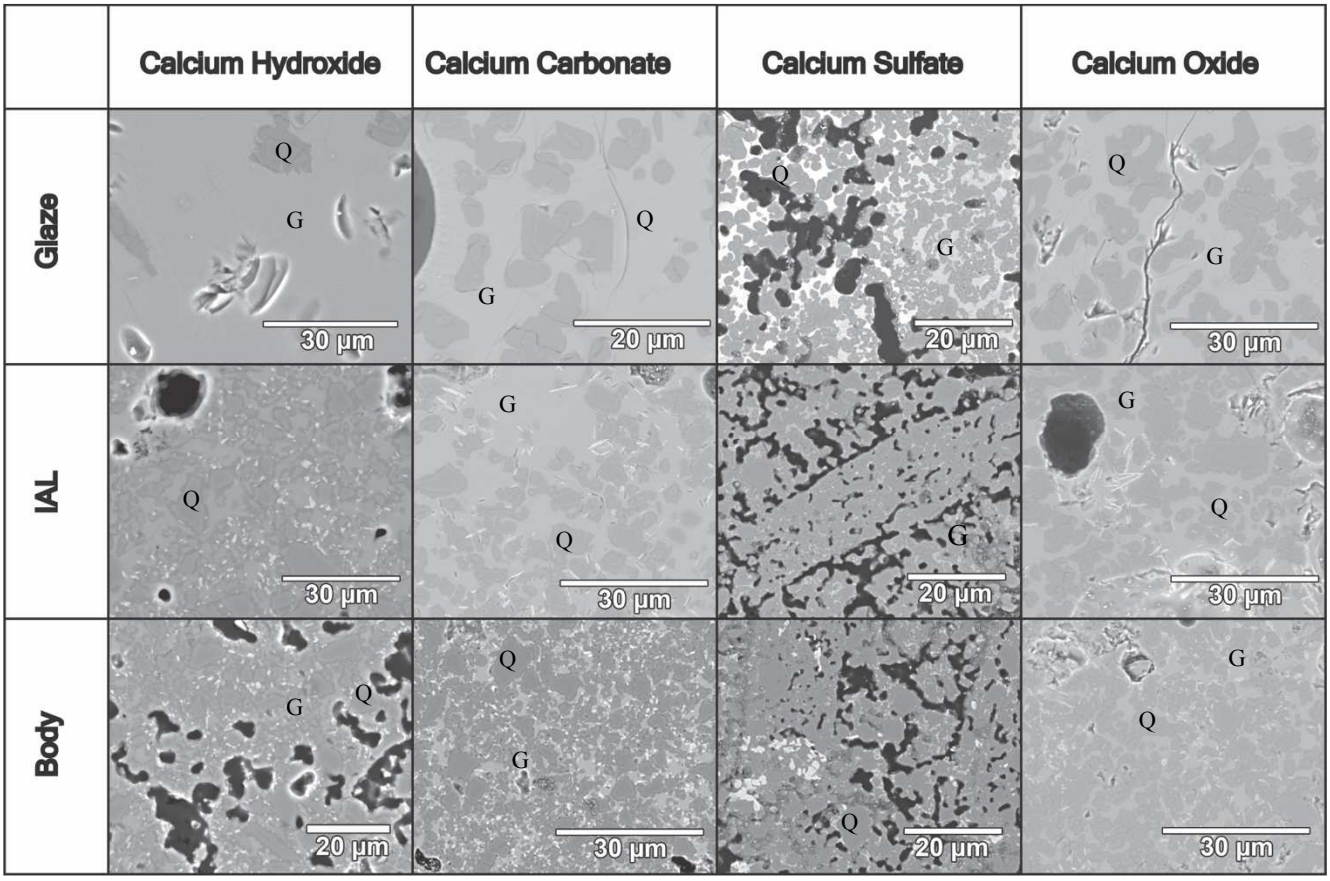

Figure 4.3 SEM images of faience microstructures synthesized using three different calcium sources. The white needles are calcium silicate (wollastonite or parawollastonite). The dark grey grains are quartz crystals (Q) and the light grey matrix is glassy matrix (G).

Calcium Source		SiO_2	CaO	Na_2O	CuO	Al_2O_3	K_2O	Na_2O/CaO	Na_2O/CuO
Calcium Hydroxide	**Glaze**	76.7	4.7	11.3	4.2	2.7	0.5	2.4	2.7
	IAL	87.4	3.5	4.4	1.3	3.3	-	1.3	3.4
	Body	88.7	3.5	3.0	1.1	3.8	-	0.9	2.7
Calcium Carbonate	**Glaze**	79.7	4.4	9.8	2.6	3.2	0.3	2.2	3.8
	IAL	81.1	3.9	7.6	1.7	-	0.3	1.9	4.5
	Body	84.9	4.4	3.4	2.3	-	0.3	0.8	1.5
Calcium Oxide	**Glaze**	80.8	3.3	7.4	4.0	2.9	0.4	2.2	1.9
	IAL	80.7	4.3	5.8	3.1	3.4	0.4	1.3	1.9
	Body	85.0	3.1	4.1	2.5	3.9	0.3	1.3	1.6
Calcium Sulfate	**Glaze**	86.3	1.1	3.5	2.7	-	0.5	3.2	1.3
	IAL	87.7	0.5	2.7	1.2	-	0.3	5.4	2.2
	Body	92.8	4.3	1.3	1.2	-	-	0.3	1.1

Table 1. Oxide% of elements in the four faience samples prepared using different calcium sources.

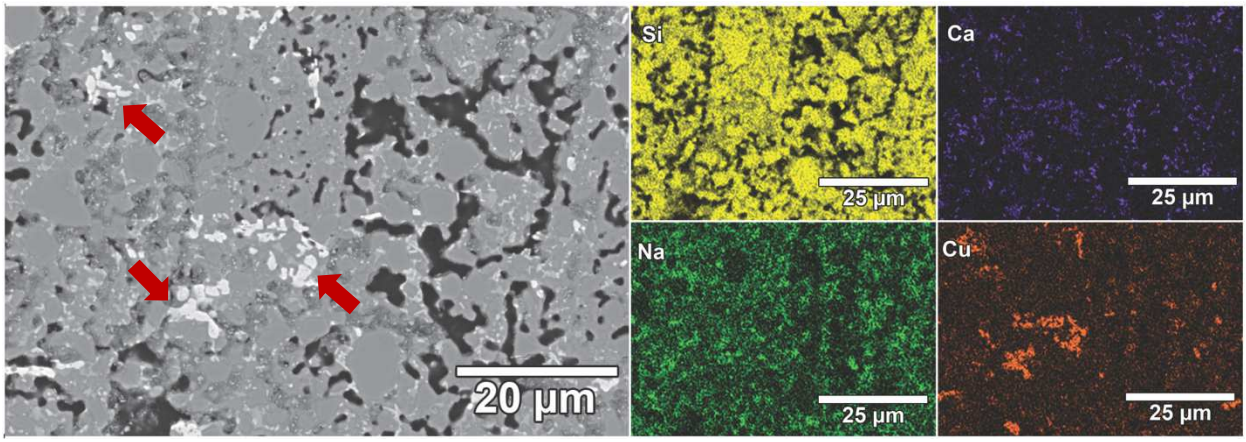

Element	Ca	Cu	Si	O
At%	1.0	1.2	4.4	10.8

Figure 4.4 SEM images of the body of the faience sample prepared using calcium sulfate (gypsum) as a source of calcium at 930 °C. The light grey crystals size range of 1 – 5 µm are Egyptian blue crystals (red arrows) which is confirmed by the elemental mapping showing the overlap of calcium and copper in addition to the elemental composition of the crystals.

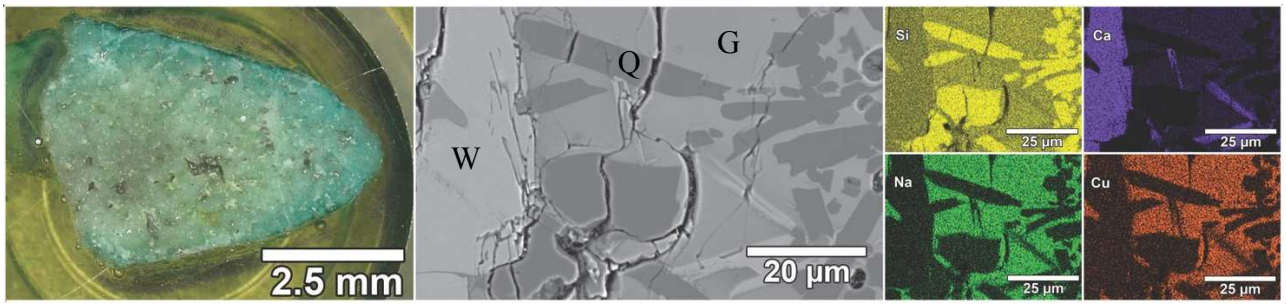

Figure 4.5 Optical image (far left) and SEM image (middle) along with the elemental mapping of the body of the faience sample prepared using calcium sulfate (gypsum) as a source of calcium at 1100 °C. The crystals with a size range of 20 – 5o µm are calcium silicate (W), and the acicular dark grey crystals are high temperature polymorphs of silicon dioxide cristobalite or tridymite (Q). The glass phase is labeled (G).

Replication of Egyptian faience using natron and plant ashes as alkali flux sources

The two possible sources of alkali in archaeological samples were either Natron or halophytic plant ashes. We attempting to replicate faience using the exact conditions and reactants except substituting our flux components, sodium carbonate and sodium bicarbonate, with a synthetic Natron salt mixture reported by Noble as a start.[7] Figure 4.6 shows optical images of a faience sample synthesized using synthetic natron and Figure 4.7 shows the SEM images of the microstructures and their elemental compositions. Archaeological faience samples synthesized using natron were characterized by their high Na_2O/K_2O ratios which is corroborated from the high Na_2O oxide percentage in our samples.

The faience sample from the Figure 4.6 appeared to be cracked from the bottom and the glazed portion of the sample. When we conducted visible induced luminescence imaging on the sample it showed very slight luminescence. A possible reason might be the presence of the high sodium chloride content used for the synthesis. The major component of the synthetic natron prepared by Noble is sodium chloride. In our previous work when we attempted to synthesize Egyptian blue crystals in the faience core, we excluded sodium chloride from our flux components. Previous analysis of natron reveals a variable amount of sodium chloride. Is still a possibility that Natron was used for the synthesis of faience or Egyptian blue but there must have been a purification process involved to exclude sodium chlorides.[24]

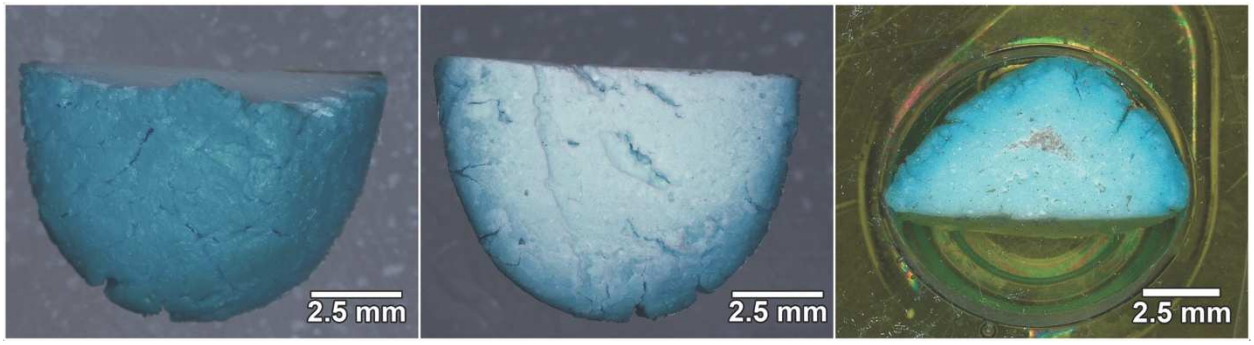

Figure 4.6 Optical microscope images of a faience sample synthesized using natron as a flux. The sample looks cracked from the top and bottom portions. The sample shows very little near-infrared luminescence.

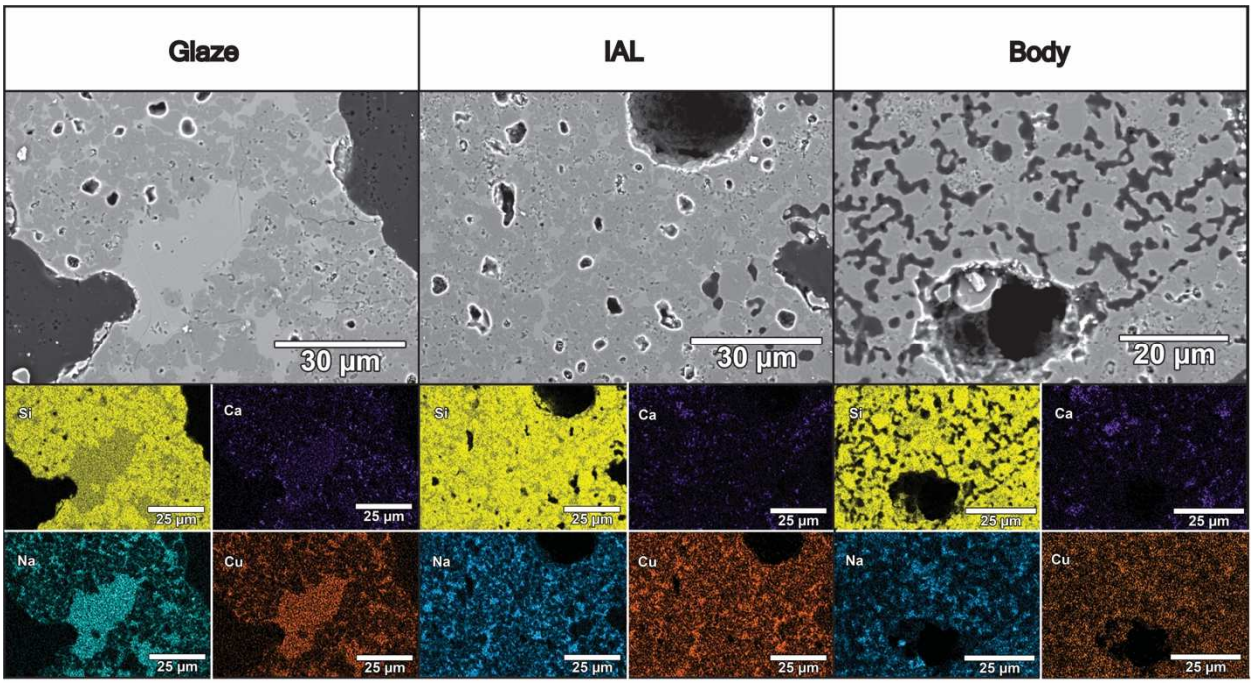

		SiO_2	CaO	Na_2O	CuO	Al_2O_3	K_2O	Na_2O/CaO	Na_2O/CuO	Na_2O/K_2O
Natron	**Glaze**	85.7	1.9	4.2	2.6	4.5	0.3	2.2	1.6	14.3
Sample	**IAL**	86.9	2.4	3.4	1.5	5.7	0.3	1.4	2.2	11.3
	Body	87.6	2.1	2.7	0.7	5.1	0.2	1.3	3.9	13.5

Figure 4.7 SEM, elemental mapping, and elemental composition (Ox%) of the faience samples synthesized with natron as a flux.

Following our faience synthesis using natron as a flux, we attempted to replicate the same faience sample but using *Salsola Soda* plant ashes. For preparation of plant ashes before we followed the method reported by Tite et al.[10] After the preparation of the plant ashes, we proceeded to analyze them before they were incorporated it in our reactions. We started by separating the plant ashes to soluble and insoluble components by simply dispersing the ashes in water. From elemental composition using EDS and PXRD in Figure 4.8, we confirmed that the soluble salts, potassium chloride and sodium chloride. With regards to the insoluble portion, we found that they contained a mixture of magnesium oxide, and silicon dioxide. We still found traces of sodium chloride and potassium chlorides in our samples.

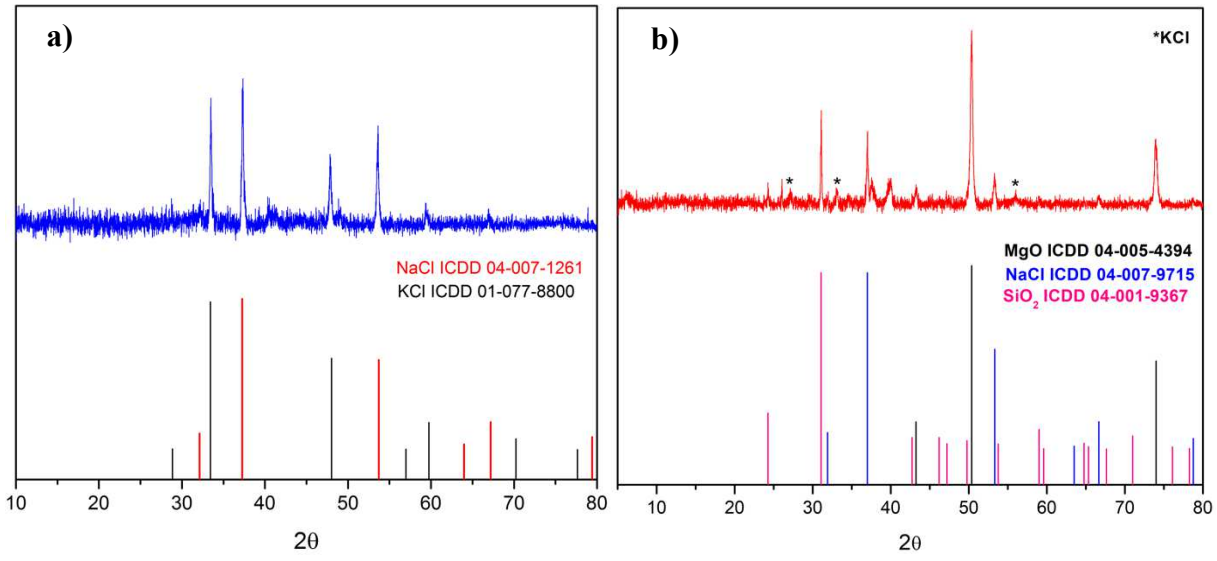

c)	SiO_2	CaO	Na_2O	MgO	K_2O	SO_3
Oxide%	1.9	7.1	10.7	5.5	55.5	3.0

Figure 4.8 PXRD patterns of the soluble portion (a) and insoluble portions (b) of the *Salsola Soda* plant ashes. (c) Analysis of the composition of the plant ashes (soluble and insoluble combined) revealed that the major component is potash.

Our results for the analysis of plant ashes were very similar to the reports in the literature in terms of the high potash content reported in Figure 4.8.[10,25,26] Bearing this information in mind, we proceeded to synthesize the faience sample using the ashes as a flux. Figure 4.9 shows the optical microscope images of the faience samples synthesized with plant ashes. The sample had a smooth shiny glaze with a turquoise color and was possibly one of the best quality faience samples we have synthesized. The sample also shows near-infrared luminescence from the core of the sample. Compared to the sample prepared with natron, the sample seemed to be of a better quality overall, meaning that the sample was not rough or cracked.

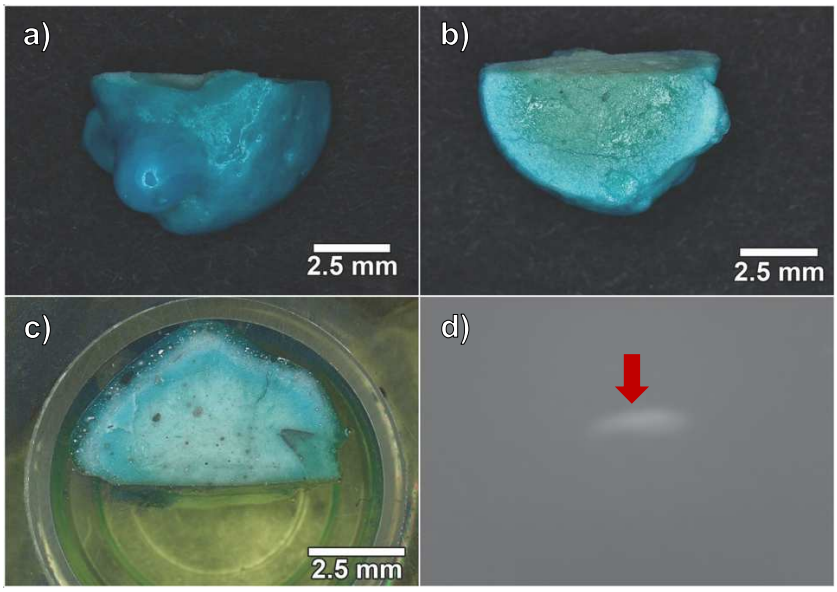

Figure 4.9 Optical microscope images of a faience sample synthesized using plant ashes a) top glazed portion of the sample, b) bottom of the sample, c) is a polished cross-section, and d) corresponding near-infrared luminescence imaging of the cross-section showing the emission of light from the core of the sample.

Figure 4.10 shows the faience microstructures of the faience samples prepared using plant ashes as a flux. Since plant ashes are rich in potash, which is indicated by the low Na_2O/K_2O ratio. One thing we noticed that plant ashes appeared to be a better flux for the growth of calcium silicate

crystals in comparison to natron. We noticed the formation of long, thin needle-like crystals, characteristic to the morphology of calcium silicate. A few of the calcium silicate crystals were also present in the glaze and body regions but they were a rod-like morphology rather than needle-like. In Figure 4.7, the calcium silicate crystals were smaller and rougher in appearance. We might form a conclusion then that for the in-situ synthesis of Egyptian blue, plant ashes would have been a better choice. To further proof our point, we attempted to synthesize bulk Egyptian blue crystals using plant ashes, natron, and borax as a flux source and we compared them.

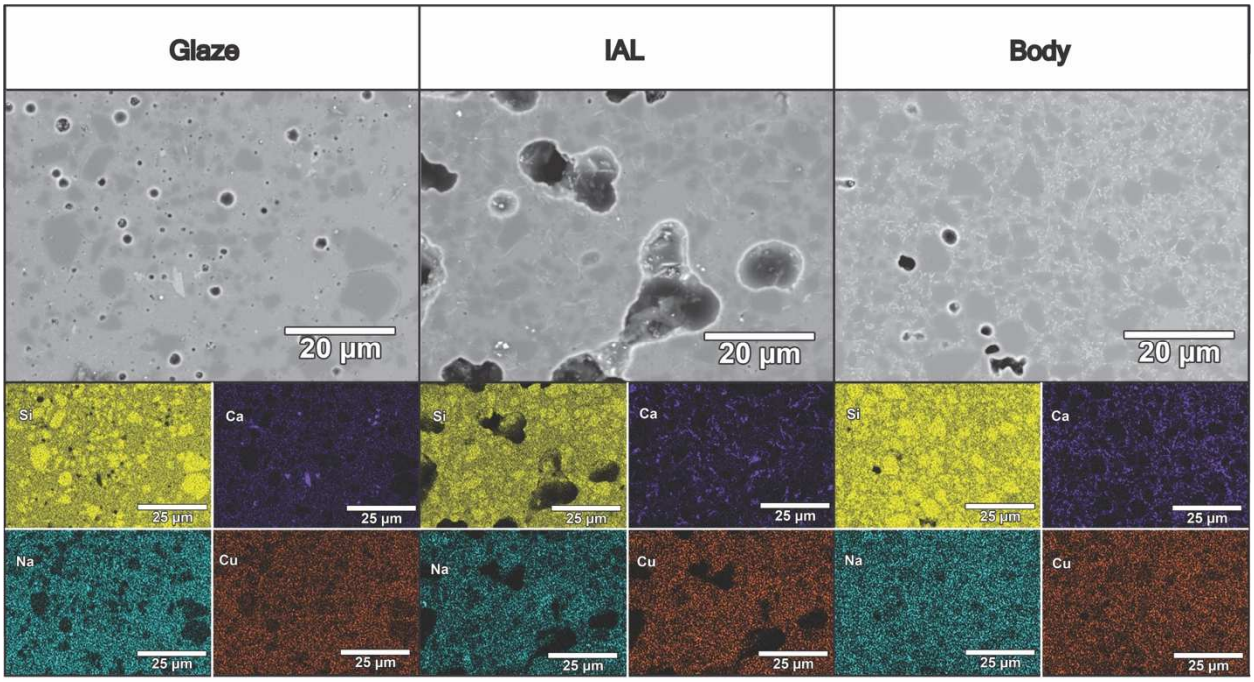

		SiO_2	CaO	Na_2O	CuO	Al_2O_3	K_2O	Na_2O/CaO	Na_2O/CuO	Na_2O/K_2O
Natron	**Glaze**	77.4	4.2	2.5	2.5	4.0	6.8	0.6	1.0	0.4
Sample	**IAL**	80.7	4.7	1.5	1.7	4.7	5.5	0.3	0.9	0.3
	Body	84.9	4.6	0.8	1.8	3.5	7.7	0.2	0.4	0.1

Figure 4.10 SEM, elemental mapping, and elemental composition (Ox%) of the faience samples synthesized with plant ashes as a flux.

Figure 4.11 shows three Egyptian blue pigment samples prepared using three different fluxes: borax, natron, and plant ashes. Borax is well established flux for the synthesis of Egyptian blue crystals.[14,18,27] From the optical images, we noticed that the color intensity of the pigments is different. For instance, the brightest blue was obtained using borax flux (Figure 4.11 (a)) and the darkest using plant ashes (Figure 4.11 (c)). The color of Egyptian blue may vary with the grain size of the crystals. Crystals that are larger in size produce a darker colored pigment while Egyptian blue crystals with a small size produce a lighter colored pigment.[28] With regards to near-infrared luminescence we also noticed that the borax sample is more luminescent than the natron and the plant ashes. Therefore, we decided to do a further investigation using SEM coupled with EDS.

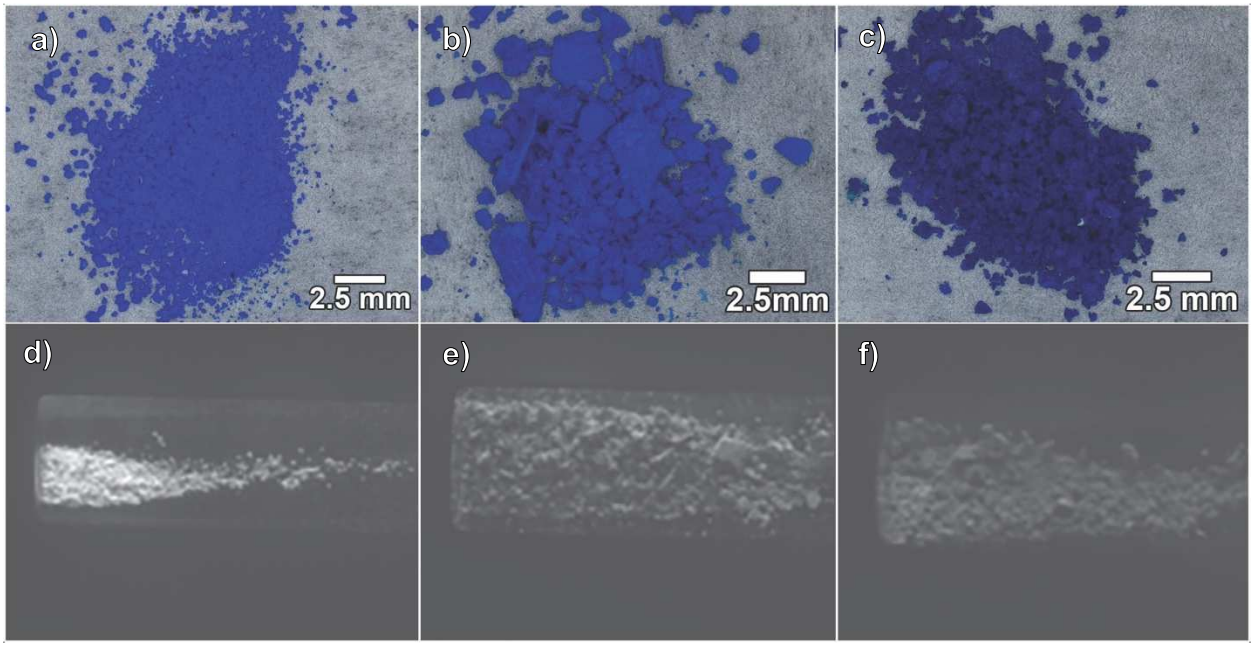

Figure 4.11 Optical microscope images of Egyptian blue pigment synthesized using different fluxes: a) borax, b) natron, and c) plant ashes. The corresponding near-infrared luminescence images are displayed below each image.

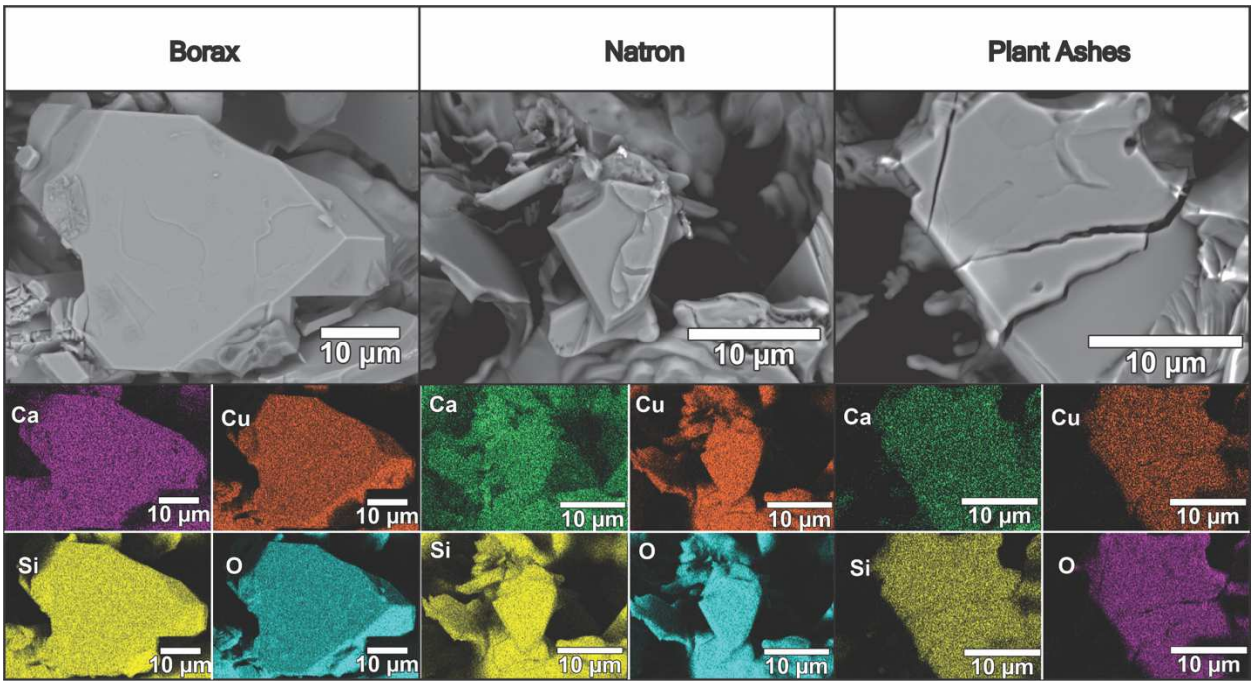

Figure 4.12 SEM images and corresponding elemental mapping for Egyptian blue crystals synthesized using borax, natron, and plant ashes as a source of flux.

From the SEM images in figure 4.12, we noticed that crystal size of Egyptian blue is very close to that of the borax sample and the crystals from the natron sample are the smallest out of the three. The crystal size of Egyptian blue obtained with plant ashes flux is very similar to the results we saw in the faience sample synthesized using plant ashes and the size of calcium silicate crystals. Although we could not image Egyptian blue crystals in the faience samples using plant ashes, but the sample gave intense luminescence from the core versus the sample synthesized using natron. One question we needed to answer is why the plant ashes sample has a darker color although it has large crystals. In the sample with plant ashes, we noticed that there is unreacted copper oxide in the imaging field making the sample darker (Figure 4.13).

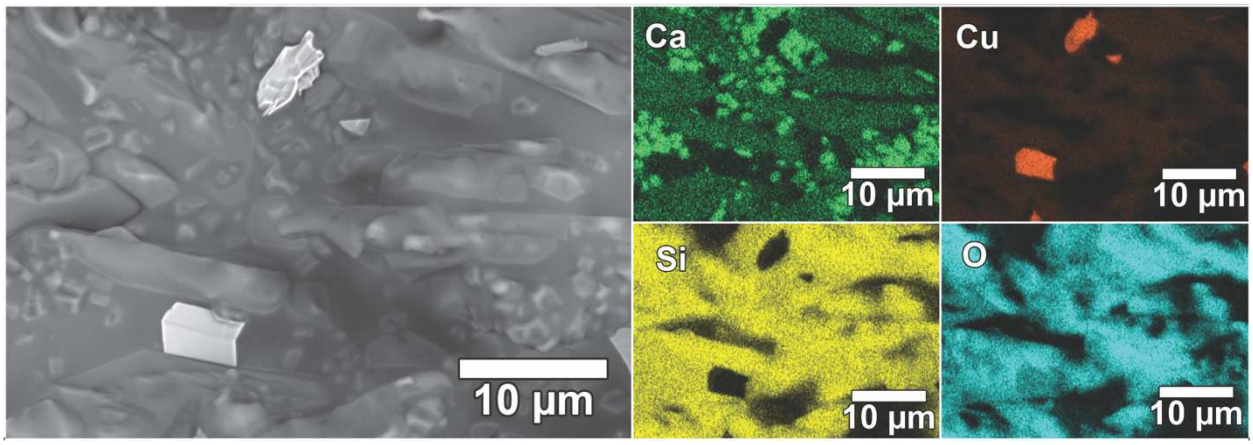

Figure 4.13 SEM image and corresponding elemental mapping for Egyptian blue crystals synthesized using plant ashes as a source of flux. The light grey features are excess copper oxide as confirmed by the copper and oxygen mapping. The dark grey Egyptian blue crystals are embedded in silicon dioxide matrix. The color density in the calcium mapping is due to the presence of calcium silicate crystals.

When we initially analyzed the plant ashes, we noticed the presence of calcium from the elemental composition and EDS. We wanted to investigate in this case if the plant ashes alone and without the addition of an external calcium source supply calcium for the in-situ synthesis of Egyptian blue. Figure 4.15 shows the optical images of the sample, and Figure 4.14 is the SEM, elemental mapping, and elemental composition of a faience sample synthesized using a plant ashes as a flux and without the addition of a calcium source. This sample did not display near-infrared luminescence indicating that the sample did not form Egyptian blue crystals. When we examined the elemental compositions of the faience microstructures, the oxide% of calcium was very low. The calcium content that was present in the plant ashes was probably consumed in the formation of calcium silicate crystals their formation is favored at this high temperature.

Therefore, and in conclusion we synthesized faience using natron and plant ashes as a flux source and we found that plant ashes gave a better-quality faience in comparison to natron.

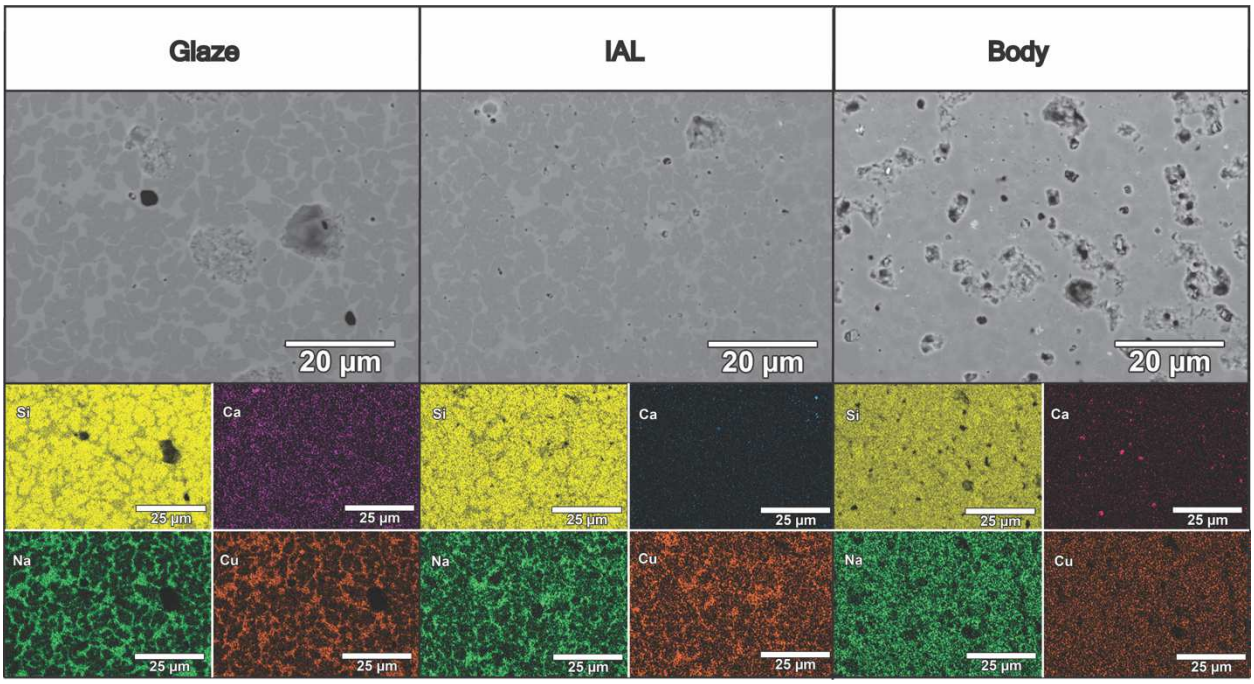

		SiO_2	CaO	Na_2O	CuO	K_2O	Na_2O/CaO	Na_2O/CuO	Na_2O/K_2O
Natron Sample	**Glaze**	88.8	0.4	3.7	2.9	0.9	9.3	1.3	4.1
	IAL	89.7	0.3	3.1	2.0	0.9	10.3	1.6	3.4
	Body	90.6	0.5	2.5	0.9	1.0	5	2.8	2.5

Figure 4.14 SEM image and corresponding elemental mapping for a faience sample synthesized using plant ashes without an additional source of calcium. There are very few calcium silicate crystals that are very small in size due to the low calcium content provided by the plant ashes.

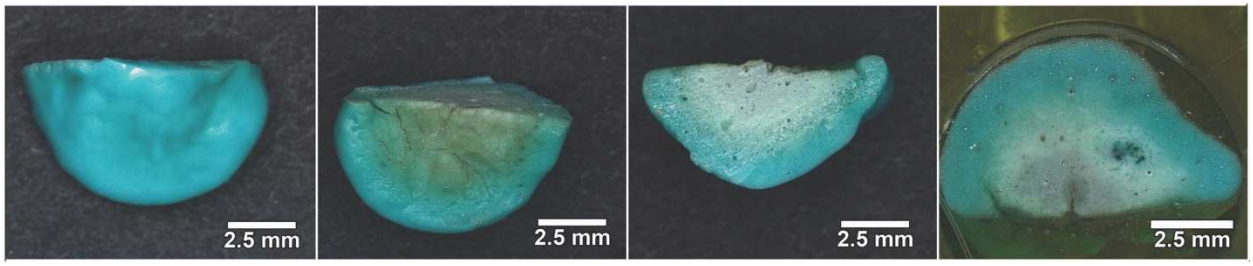

Figure 4.15 Optical microscope images of (a) top, (b) bottom, (c) cross-section, and (b) polished cross-section of a faience synthesized using plant ashes without a source of calcium. The sample did not show near-infrared luminescence.

Replication of Egyptian faience using different copper sources

In almost all our experimental work, copper oxide was the main colorant for the synthesis faience as well as the source of copper for the in-situ synthesis of Egyptian blue. Copper oxide has been found in Egyptian Late Bronze Age faience and glasses with ~0.5 – 2 % by weight and for this reason it was our source of choice.[29,30] We also wanted to explore other possible copper sources such as synthetic malachite with the formula $Cu_2CO_3(OH)_2$, as well as Egyptian blue pigment. Figure 4.16 shows the optical microscope images and corresponding near-infrared luminescence images of Egyptian faience synthesized using copper(II) oxide, synthetic malachite, and Egyptian blue as colorants. The samples synthesized using copper oxide and synthetic malachite is that both samples had a glaze that can be clearly distinguished from the body. There is also a distinct blue color in both samples which could possibly be Egyptian blue synthesized in-situ hence the luminescence emitted from their cores. However, the sample synthesized using Egyptian blue as a copper source had the same blue color throughout the sample and the glaze could not be distinguished from the core. The absence of near-infrared luminescence from this sample is an indication the absence of Egyptian blue crystals. To further investigate the reason behind the interesting features we noticed in the optical imaging we examined the samples under SEM and coupled with EDS to obtain elemental composition information.

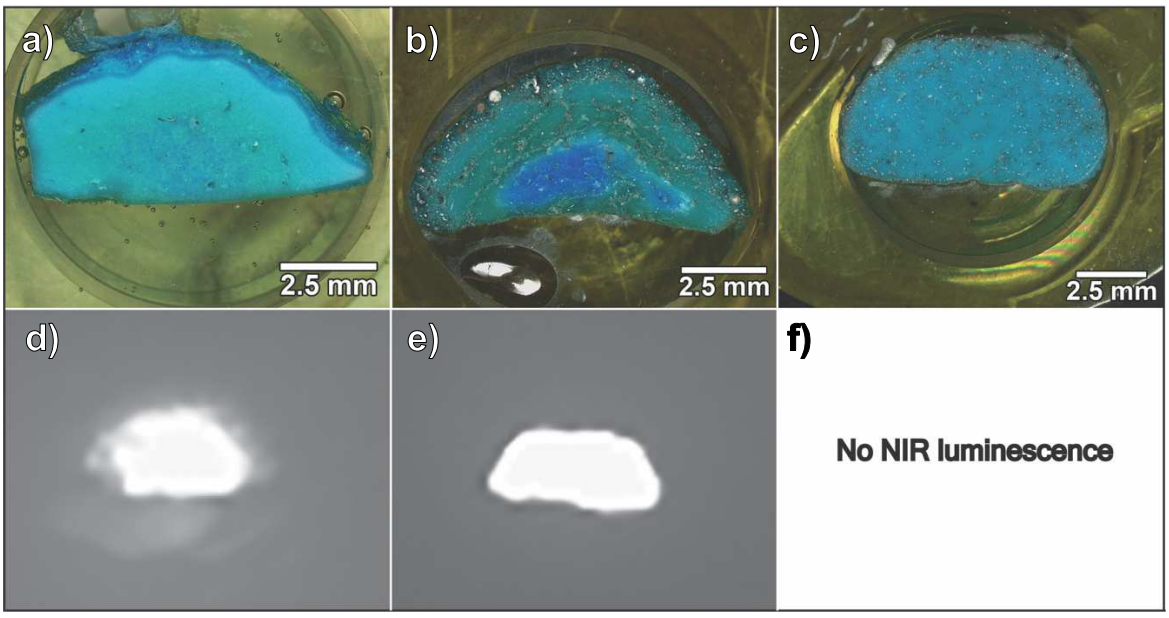

Figure 4.16 Optical microscope images of Egyptian faience synthesized using different copper sources a) copper oxide, b) copper carbonate, and c) Egyptian blue. The corresponding near-infrared images (d and e) are displayed below. The sample synthesized using EB as a source of copper did not display near-infrared luminescence. The sample also did not have a distinguishable glaze.

From the SEM images, we observed that the glaze region in faience samples synthesized using copper oxide and Egyptian blue contained acicular quartz crystals, characteristic of the high temperature polymorphs of quartz tridymite or cristobalite which can be expected at this high temperature. We previously established that calcium silicate or its polymorphs form at the temperature at which our faience samples are fired especially in the interaction layer.

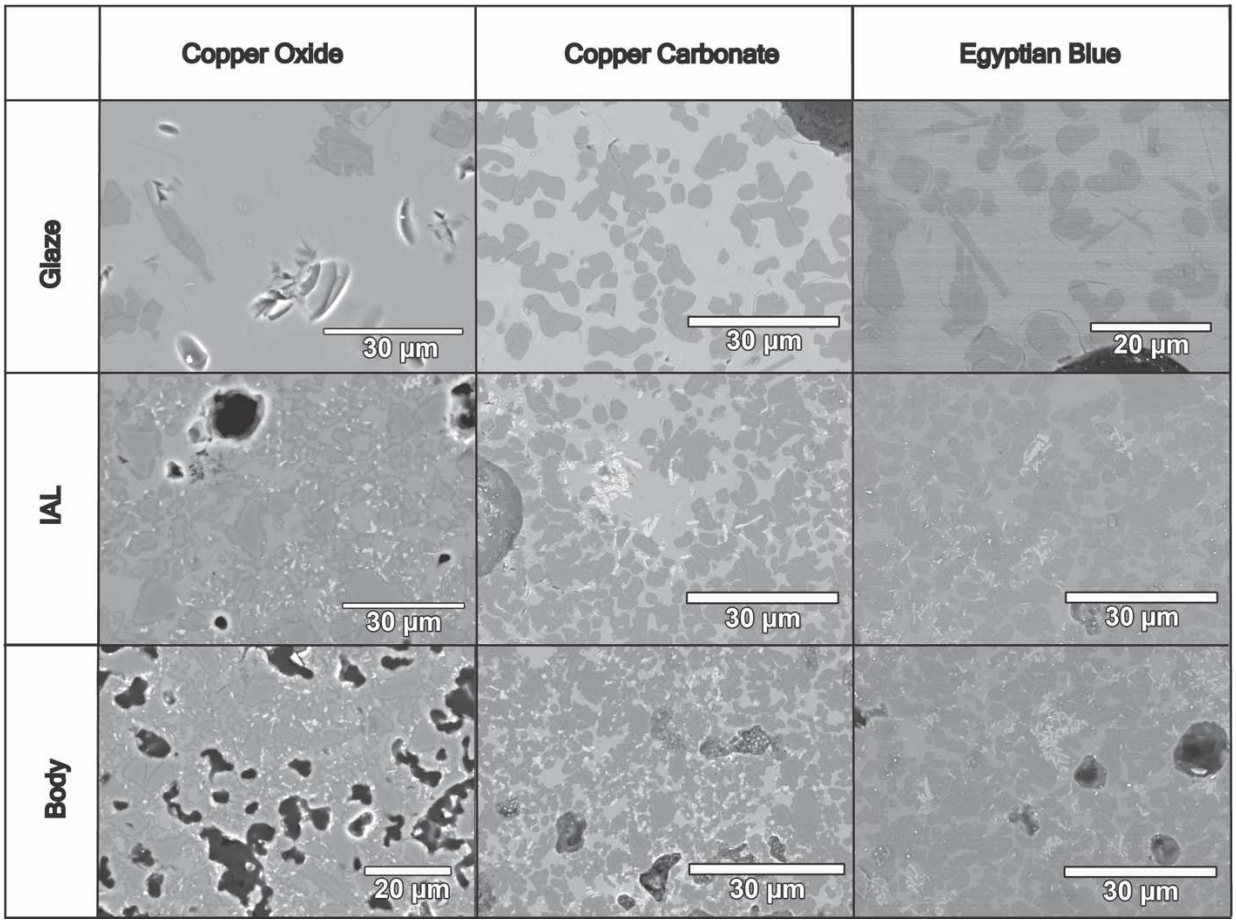

Figure 4.17 SEM images of faience microstructures synthesized using three different copper sources. The white rod or needle-like crystals are calcium silicate (wollastonite or parawollastonite). The dark grey grains are quartz crystals (Q) and the light grey matrix is glassy matrix (G).

Copper Source		SiO_2	CaO	Na_2O	CuO	K_2O	Na_2O/CaO	Na_2O/CuO	CuO/CaO
Copper oxide	**Glaze**	76.7	4.7	11.3	4.2	0.5	2.4	2.7	0.9
	IAL	87.4	3.5	4.4	1.3	-	1.3	3.4	0.4
	Body	88.7	3.5	3.0	1.1	-	0.9	2.7	0.3
Copper Carbonate	**Glaze**	81.8	3.5	8.3	6.0	0.3	2.4	1.4	1.7
	IAL	86.0	4.1	5.9	3.7	0.1	1.4	1.6	0.9
	Body	89.0	3.7	3.6	3.4	0.2	1.0	1.1	0.9
Egyptian blue	**Glaze**	80.2	4.1	10.5	2.6	0.3	2.6	4.0	0.6
	IAL	85.5	3.5	6.1	1.5	0.4	1.7	4.1	0.4
	Body	84.9	4.8	5.3	1.7	0.3	1.1	3.1	0.3

Table 2. Oxide% of elements in the four faience samples prepared using different copper sources.

Examining the data in Table 2., we noticed that the oxide% for sodium in the interaction layer for both copper carbonate and Egyptian blue are higher than in the copper oxide sample. The presence of higher flux content in the interaction layer might have played a role in the growth of the calcium silicate crystals. It intrigued us that we saw the blue color in the sample synthesized with the synthetic malachite (copper carbonate) as this color appeared to us to be closer to the color of Egyptian blue. In addition, from Table 2., we noticed that the CuO/CaO ratio was the highest out of the three samples which strongly indicates the presence of Egyptian blue especially in the body of the sample. Upon further examination of the body of the faience sample synthesized with copper carbonate, we found Egyptian blue crystals that corroborated the blue color that we saw in the optical images. Figure 4.18 confirms the presence of Egyptian blue as evidenced in the overlap of the calcium and copper elemental maps.

The reason for the formation of Egyptian blue crystals in the synthetic malachite is related to the stoichiometry of copper and calcium in the faience sample. $Cu_2CO_3(OH)_2$ decomposes at a temperature ~380 °C giving copper oxide, carbon dioxide, and water according to the equation below[31]:

$$CuCO_3 \cdot Cu(OH)_2 \longrightarrow 2\ CuO + CO_2 + H_2O$$

From the equation above, $Cu_2CO_3(OH)_2$ gives off two moles of copper oxide. From our previous work we proved experimentally that when the concentration of copper is raised and is nearly equal to the concentration of calcium micron-sized Egyptian blue crystals form.

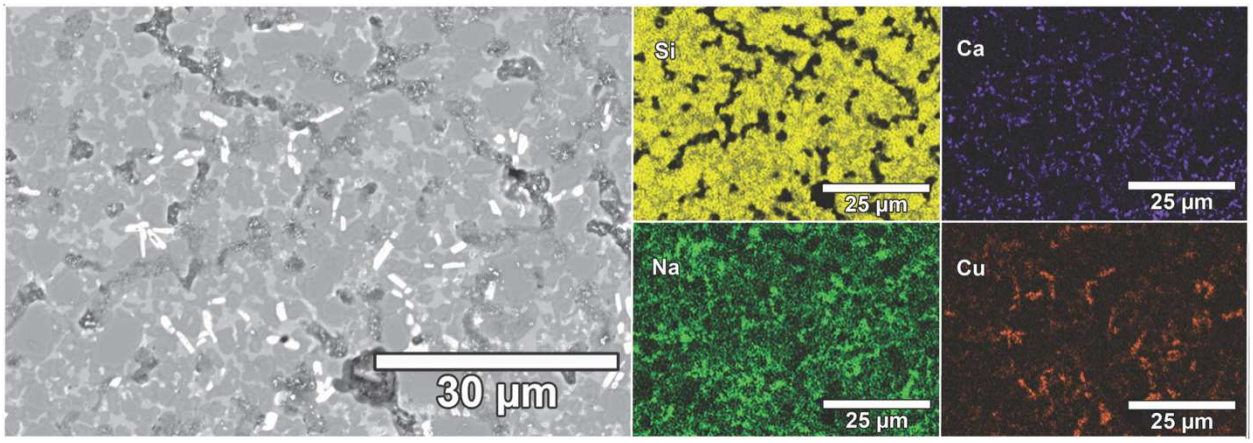

Figure 4.18 SEM images of the faience body of the faience sample synthesized with synthetic malachite. The white rod-like crystals in the imaging field are Egyptian blue crystals. The identity of the crystals is confirmed by the overlap of the calcium and copper maps.

With regards to the faience sample synthesized using Egyptian blue as a source of copper we wanted to find out the reason behind it not showing luminescence. We suspected that the flux mixture, sodium carbonate and sodium bicarbonate, dissolved the Egyptian blue crystals and therefore the glaze, interaction layer, and body was indistinguishable macroscopically. We hypothesize that the flux dissolved all Egyptian blue crystals, therefore copper was evenly spread across the sample.

We also wanted to test a different method in which we used Egyptian blue is a source of copper colorant. This was our first attempt using application glazing method using Egyptian blue as a colorant specifically for the glaze. Application glazing is a two-step process in which the body is prepared from quartz, calcium hydroxide, and binders without a copper colorant and then fired. The next step involved the preparation of preparation of a glaze mixture consisting of quartz, Egyptian blue which is the copper colorant, and flux. Figure 4.19 shows optical microscope images faience sample synthesized using application glazing and Figure 4.20 shows the SEM and elemental mapping of the microstructures of the sample. From the optical microscope images, we noticed that the sample closely resembles semi-precious stones such as lapis lazuli or azurite. The glaze seemed to be glassy and of a translucent nature very different than the faience samples prepared using efflorescence glazing. However, this sample did not show any near-infrared luminescence.

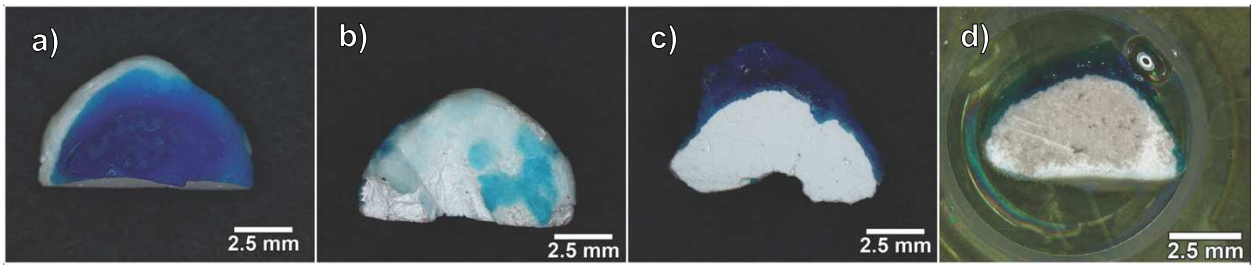

Figure 4.19 Optical microscope images of (a) top, (b) bottom, (c) cross-section, and (b) polished cross-section of a faience synthesized using application glazing and Egyptian blue as a source of copper.

From the SEM images in Figure 4.20, the glaze contained the high temperature polymorph of silicon dioxide, cristobalite which we confirmed its identity by PXRD in Figure 4.21. The interaction layer and the body showed quartz grains which was expected. We were questioning why the sample did not luminesce although the sample contained Egyptian blue crystal? Similar to the faience sample prepared using the efflorescence method and Egyptian blue as a colorant we

also proposed that the flux components used to prepare the glaze dissolved the crystals. We proceeded with an experiment where we ran the glaze at a lower temperature, specifically at 300 and 600 °C to examine if the glaze will dissolve the Egyptian blue crystals or not.

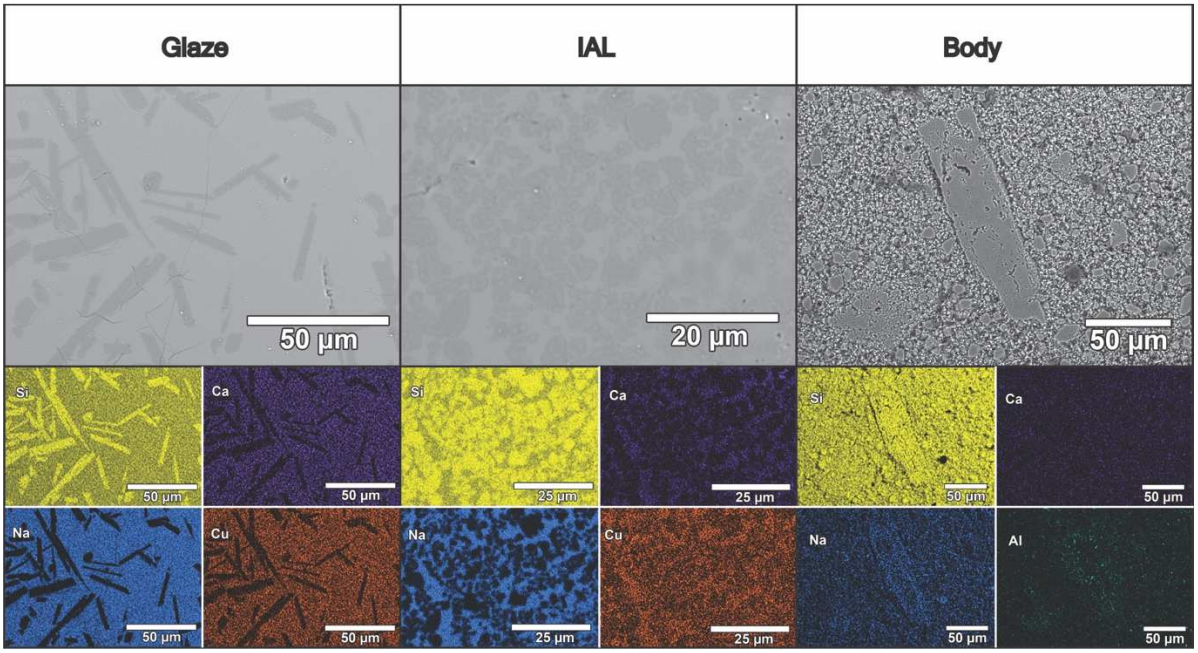

		SiO_2	CaO	Na_2O	CuO	K_2O	Al_2O_3	Na_2O/CaO	Na_2O/CuO
Natron	**Glaze**	78.1	3.4	13.2	5.3	-	-	3.9	2.5
Sample	**IAL**	87.7	1.9	6.0	-	-	-	3.2	-
	Body	87.9	3.8	1.3	-	0.4	6.3	0.3	-

Figure 4.20 SEM image, corresponding elemental mapping, and elemental composition for the faience sample synthesized using application glazing and Egyptian blue as the glaze copper colorant. The acicular crystals in the glaze are cristobalite, the high temperature polymorph of silicon dioxide.

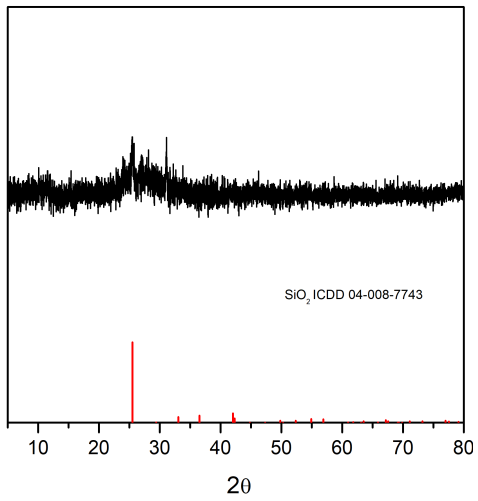

Figure 4.21 PXRD pattern on the blue glaze of the sample shown in Figure 4.19. The pattern matched with the high temperature silicon dioxide polymorph cristobalite.

Figure 4.22 shows the SEM and corresponding elemental mapping of the glaze in the application glazing process fired at 300 °C (a) and 600 °C (b). At 300 °C we saw that there were still intact Egyptian blue crystals although the edges started to dissolve. Upon raising the temperature to 600 °C the crystals appeared to be completely dissolved giving copper oxide.

The sources of copper used seemed to be a viable option as faience colorant although the synthetic malachite produced micron-sized Egyptian blue crystals and copper oxide gave submicron crystals. Egyptian blue was also an option although it is dissolved by the flux mixture and therefore the samples did not display luminescence.

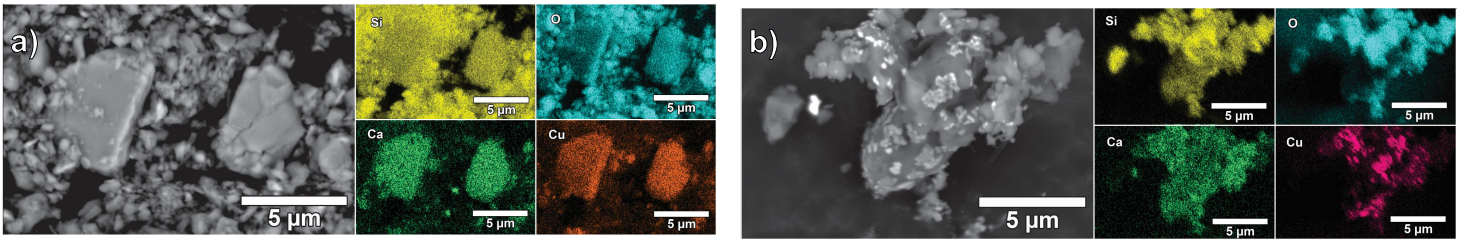

Figure 4.22 SEM imaging of EB crystals mixed with flux for the application glazing fired at 300 (a) and 600 °C (b). The corresponding elemental mapping is shown for each temperature. At 300 °C the Egyptian blue crystals remain intact while at 600 °C the crystals dissolve to give copper oxide.

Replication of Egyptian faience using different substrates

Our experimental work with faience entailed one main substrate which is laboratory grade alumina crucibles. We wanted to extend our work further and test out the effect of substrates such as clay or terracotta which is an aluminosilicate clay or lime (main component was CaO) that were archaeologically discovered and examine their effect on the in-situ synthesis of Egyptian blue on Faience. In our experiments we kept all the conditions and the starting reactants the same as our original synthesis to see how the substrate will affect our results. Figure 4.23 shows the optical images of the polished cross-sections of the four faience samples synthesized on three different substrates: alumina, terracotta, terracotta plus lime powder, and terracotta plus lime powder without a source of calcium.

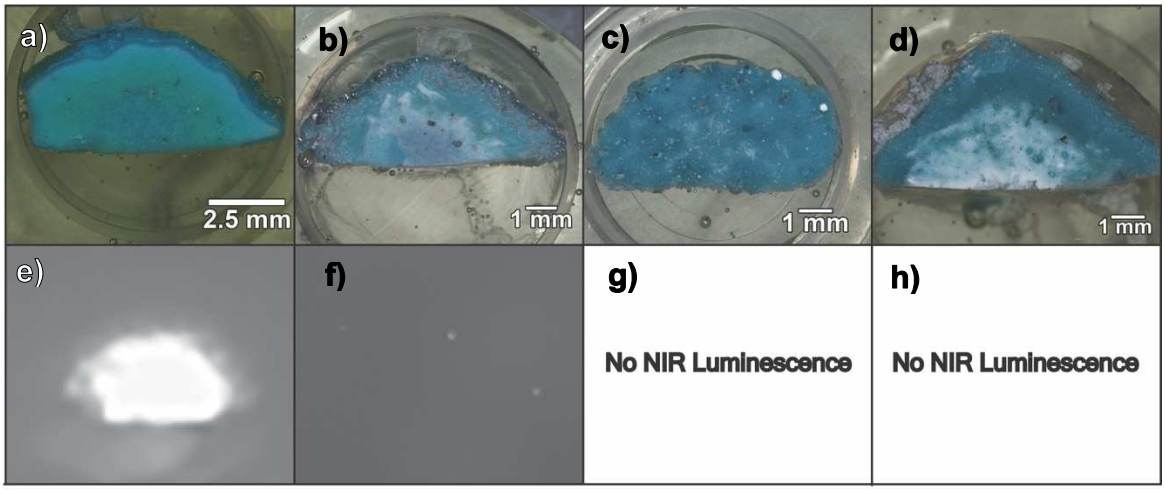

Figure 4.23 Optical microscope images of polished cross-sections of four faience samples synthesis using different substrates: (a) alumina, (b) terracotta, (b) lime powder and terracotta, and (c) lime powder and terracotta without a calcium source. The corresponding near-infrared images for samples (e) and (f) for the optical images are shown below.

All the samples except the ones synthesized on the alumina and terracotta substrates did not display any near-infrared luminescence. The cross-sections in Figure 4.23 of the samples looked distinctively different from each another. For instance, the cross-section of the sample synthesized on terracotta and lime powder was uniformly colored throughout while the sample synthesized on terracotta and lime powder without a calcium source for the synthesis has a whitish-blue colored core. We imaged the polished cross-sections using SEM and the microstructures along with the elemental compositions of each sample is shown in Figure 4.24 and Table 3. In faience sample synthesized on lime and terracotta, the glaze, interaction layer, and the body were abundantly populated with calcium silicate crystals which may be doped with copper and for this reason the sample is colored throughout. This is again very reminiscent of archaeological Egyptian green frit samples in terms of color which had a pale blue color or blue-green color due to the presence of the copper doped calcium silicate. From Table 3, we also noticed that the oxide% for calcium has a higher value in the interaction layer suggesting that during the firing process there

might have been a diffusion of calcium ions from the lime powder to the faience sample. The presence of excess calcium over the copper content does not favor the formation of Egyptian blue. In addition, the high temperatures favor the formation of calcium silicate. To put our hypothesis to test, we decided to fire a faience sample synthesized without a calcium source on terracotta and lime powder. From Figure 4.24, we did not notice the formation of any calcium silicate crystals in any of the faience microstructures. This might explain why the optical microscope image of this sample, Figure 4.23 (d) does not have a blue core versus the faience sample synthesized using a calcium source on lime and terracotta.

From our experiments we reached a conclusion that archaeological faience samples would have been possibly synthesized on terracotta or on terracotta with a lime slip layer in kilns. For the archaeological samples containing Egyptian blue crystals, the synthesis was conducted on terracotta and not terracotta and lime powder.

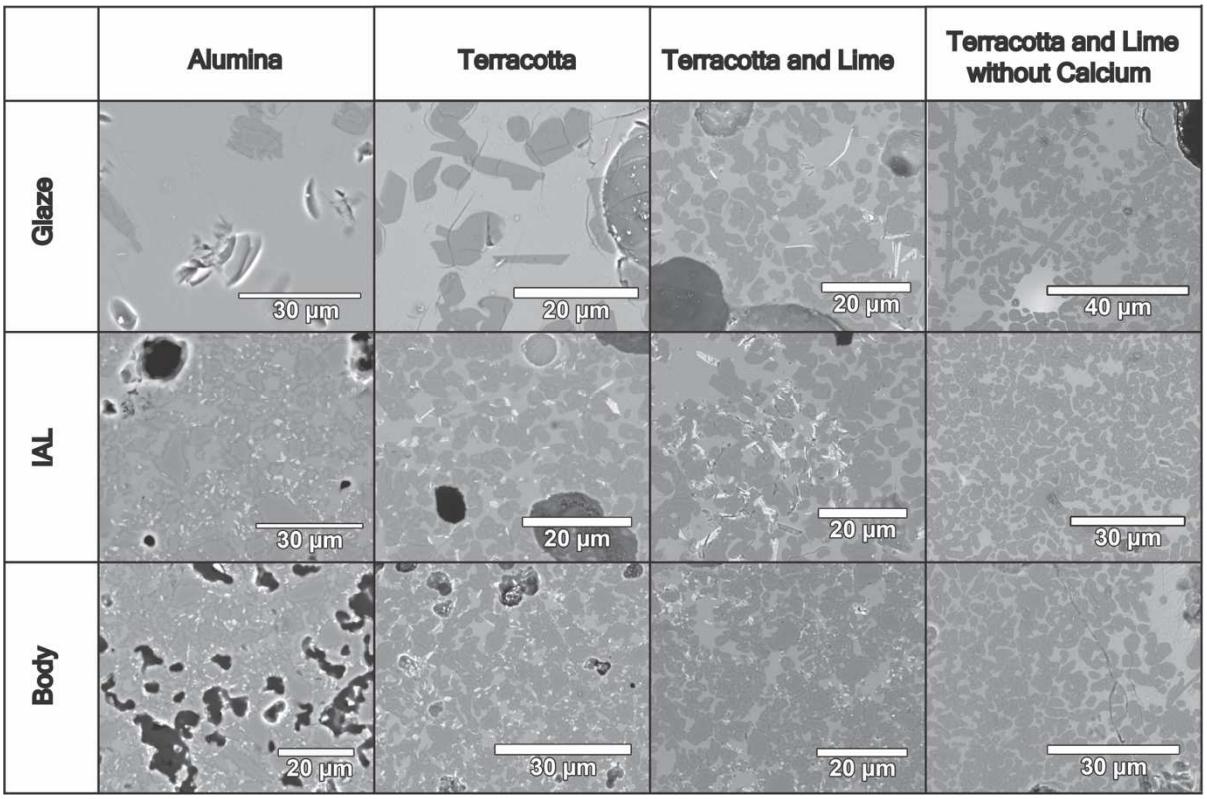

Figure 4.24 SEM images of faience microstructures synthesized using different substrates. The white rod or needle-like crystals are calcium silicate (wollastonite or parawollastonite). The dark grey grains are quartz crystals (Q), and the light grey matrix is glassy matrix (G).

Substrate		SiO_2	CaO	Na_2O	CuO	Al_2O_3	K_2O	Na_2O/CaO	Na_2O/CuO
Alumina	**Glaze**	76.7	4.7	11.3	4.2	2.7	0.5	2.4	2.7
	IAL	87.4	3.5	4.4	1.3	3.3	-	1.3	3.4
	Body	88.7	3.5	3.0	1.1	3.8	-	0.9	2.7
Terracotta	**Glaze**	77.7	4.8	9.8	3.4	2.8	0.3	2.0	2.9
	IAL	83.9	3.6	5.7	1.8	4.5	-	1.6	3.2
	Body	85.2	3.9	3.6	1.9	4.1	-	0.9	1.9
Terracotta and Lime	**Glaze**	84.7	3.3	5.9	2.3	-	0.3	1.8	2.6
	IAL	83.8	4.9	5.4	2.3	-	0.3	1.1	2.3
	Body	87.6	2.7	4.3	1.7	-	0.3	1.6	2.5
Terracotta and Lime without Calcium	**Glaze**	86.2	-	7.2	2.5	3.4	-	-	3.0
	IAL	89.7	-	4.6	3.3	3.3	0.3	-	1.4
	Body	87.0	1.5	5.0	2.7	0.3	0.3	4.2	1.9

Table 3. Oxide% of elements in the four faience samples prepared using different substrates.

Conclusion

The choice starting material for faience synthesis plays an important role in the evolution of Egyptian blue crystals in the faience core as they share common starting materials such as calcium, alkali flux, copper source, or even substrates. Calcium carbonate found in calcite, dolomitic stones, or shell fragments might have been a source for both faience and Egyptian blue synthesis in archaeological samples. Similarly, calcium hydroxide found in limestone serves a

similar person. Calcium oxide or lime on the other hand maybe a starting raw material for synthesis of faience but not for the in-situ synthesis of Egyptian blue in faience samples. Also, to obtain calcium oxide, very high temperatures were required which did not seem viable due to limited fuel resources in ancient Egypt.

Alkali flux was quantified in archaeological samples and the two main resources the evaporitic deposit, natron, or halophytic plant ashes. In either cases, a purification process for both sources might have been conducted to remove sodium chloride to serve two purposes: obtain a smother and better quality of faience and for the in-situ synthesis of Egyptian blue in faience cores. Halophytic plant ashes were a better flux for our synthesis providing a better-quality glaze. Although the plant ashes contained calcium, they produced a glassy smooth glazed faience but did not provide enough calcium for the synthesis Egyptian blue in the faience core.

Variety of copper sources have been proposed as the colorant in archaeological faience samples including Egyptian blue pigment. For our efflorescence glazing experiments, we mainly utilized copper oxide which was consistently provided luminescence in faience. Synthetic malachite, which is a basic copper(II) carbonate yielded micron-sized Egyptian blue crystals in the faience core as it decomposed to give two moles of copper oxide raising the copper content in Faience making it close to the stoichiometry of calcium.

Finally, the substrate used for firing the faience samples should not be understated. Kilns used for firing ancient faience samples were lined with terracotta or often with terracotta and a lime slip layer to be able to separate the samples from one another. Lime, with the main component of CaO seemed to inhibit the formation of Egyptian blue crystals in the faience samples. We also discovered that there might be diffusion of calcium during the firing process into the faience samples however it was not enough for the in-situ synthesis of Egyptian blue crystals. Overall, we

successfully investigated possible sources of raw materials for the synthesis of faience and in-situ synthesis of faience in Egyptian blue.

References

1. Tite, M., A. Shortland, and S. Paynter, *The beginnings of vitreous materials in the Near East and Egypt.* Accounts of chemical research, 2002. **35**(8): p. 585-593.
2. Glass, C.M.o. and R.M. Brill, *Chemical Analysis of Early Glasses: The Catalogue*. 1999: Corning Museum of Glass.
3. Tite, M.S., P. Manti, and A.J. Shortland, *A technological study of ancient faience from Egypt.* Journal of Archaeological Science, 2007. **34**(10): p. 1568-1583.
4. Nenna, M. and P. Nicholson, *Faience technology.* WORKING IN MEMPHIS, 2013: p. 133.
5. Shortland, A., *Evaporites of the Wadi Natrun: seasonal and annual variation and its implication for ancient exploitation.* Archaeometry, 2004. **46**(4): p. 497-516.
6. Shortland, A., et al., *Natron as a flux in the early vitreous materials industry: sources, beginnings and reasons for decline.* Journal of Archaeological Science, 2006. **33**(4): p. 521-530.
7. Noble, J.V., *The technique of Egyptian faience.* American journal of archaeology, 1969. **73**(4): p. 435-439.
8. Sayre, E.V. and R.W. Smith, *Some materials of glass manufacturing in antiquity*, in *Archaeological chemistry*. 2016, University of Pennsylvania Press. p. 279-312.
9. Crawford, R., *Studies in plant survival*. 1989: Blackwell Scientific Oxford.

10. Tite, M.S., et al., *The composition of the soda-rich and mixed alkali plant ashes used in the production of glass.* Journal of Archaeological Science, 2006. **33**(9): p. 1284-1292.

11. Pospíšilová, J., *Larcher, W.: Physiological Plant Ecology. Ecophysiology and Stress Physiology of Functional Groups.* Biologia Plantarum, 2003. **47**(4): p. 500-500.

12. Thy, P., C. Lesher, and B. Jenkins, *Experimental determination of high-temperature elemental losses from biomass slag.* Fuel, 2000. **79**(6): p. 693-700.

13. Brill, R.H., *Ancient glass.* Scientific American, 1963. **209**(5): p. 120-131.

14. Ragai, J., *Snapshots of chemical practices in Ancient Egypt.* Substantia, 2018. **2**(1): p. 93-101.

15. Ragai, J., *Colour: its significance and production in Ancient Egypt.* Endeavour, 1986. **10**(2): p. 74-79.

16. Wendrich, W., *UCLA Encyclopedia of Egyptology*. 2008: UCLA, Department of Near Eastern Languages and Cultures.

17. Welc, F., *Faience Workshop in Ptolemaic Athribis (Tell Atrib) in the Nile Delta. Archaeological Evidence.* Études et travaux, 2013. **26**: p. 719.

18. Johnson-McDaniel, D. and T.T. Salguero, *Exfoliation of Egyptian blue and Han blue, two alkali earth copper silicate-based pigments.* JoVE (Journal of Visualized Experiments), 2014(86): p. e51686.

19. Pagès-Camagna, S. and S. Colinart, *The Egyptian green pigment: its manufacturing process and links to Egyptian blue.* Archaeometry, 2003. **45**(4): p. 637-658.

20. Swift, W., et al., *Decomposition of calcium sulfate: a review of the literature.* 1976.

21. Hatton, G.D., A.J. Shortland, and M.S. Tite, *The production technology of Egyptian blue and green frits from second millennium BC Egypt and Mesopotamia.* Journal of Archaeological Science, 2008. **35**(6): p. 1591-1604.

22. Karunadasa, K.S.P., et al., *Thermal decomposition of calcium carbonate (calcite polymorph) as examined by in-situ high-temperature X-ray powder diffraction.* Journal of Physics and Chemistry of Solids, 2019. **134**: p. 21-28.

23. Koga, N., L. Favergeon, and S. Kodani, *Impact of atmospheric water vapor on the thermal decomposition of calcium hydroxide: A universal kinetic approach to a physico-geometrical consecutive reaction in solid–gas systems under different partial pressures of product gas.* Physical Chemistry Chemical Physics, 2019. **21**(22): p. 11615-11632.

24. Giménez, J., et al., *Effect of NaCl on the fabrication of the Egyptian blue pigment.* Journal of Archaeological Science: Reports, 2017. **14**: p. 174-180.

25. Tite, M.S. and A.J. Shortland, *Production technology for copper-and cobalt-blue vitreous materials from the New Kingdom site of Amarna—a reappraisal.* Archaeometry, 2003. **45**(2): p. 285-312.

26. Dariz, P. and T. Schmid, *Trace compounds in Early Medieval Egyptian blue carry information on provenance, manufacture, application, and ageing.* Scientific reports, 2021. **11**(1): p. 1-12.

27. Wiedemann, H.G. and G. Bayer, *The bust of Nefertiti.* Analytical chemistry, 1982. **54**(4): p. 619-628.

28. Oudbashi, O. and M. Hessari, *A "Western" imported technology: an analytical study of the Achaemenid Egyptian blue objects.* Journal of Cultural Heritage, 2021. **47**: p. 246-256.

29. Smirniou, M. and T. Rehren, *Shades of blue–cobalt-copper coloured blue glass from New Kingdom Egypt and the Mycenaean world: a matter of production or colourant source?* Journal of Archaeological Science, 2013. **40**(12): p. 4731-4743.

30. Shortland, A. and K. Eremin, *The analysis of second millennium glass from Egypt and Mesopotamia, part 1: new WDS analyses.* Archaeometry, 2006. **48**(4): p. 581-603.

31. Brown, I., K. Mackenzie, and G. Gainsford, *Thermal decomposition of the basic copper carbonates malachite and azurite.* Thermochimica acta, 1984. **75**(1-2): p. 23-32.

CHAPTER 5

CONCLUSIONS AND FUTURE WORK

Conclusions and Future Work

Near-infrared luminescent materials specifically those based on d-block metals such as copper and manganese have a wide range of applications due to their unique optical properties in fields such as biomedical imaging,[1-4] solid state lasers,[5,6] archaeology,[7,8] and forensics.[9,8] Near-infrared luminescent pigments such manganese blue and Egyptian blue are two blue colored pigments known for their history and their unique near-infrared emission profiles. Manganese blue displays a broadband emission profile centered at ~1300 nm[11] making it an ideal candidate for the biomedical imaging in the NIR-II window (1000 – 1700 nm) where there is minimal tissue autofluorescence and scattering affording better resolution.[12] Egyptian blue displays strong near-infrared luminescence at 910 nm which is a convenient tool for its non-invasive characterization in ancient artifacts.[13]

In chapter 2, we detailed the synthetic procedures for both bulk and nano manganese blue crystals. The manganese source, which was manganese(IV) oxide, supplied in our reaction is very important especially when using an oxidizing flux such as barium nitrate. The temperature as well as the firing conditions are important determining factors for the success of our reactions. Temperatures up to ~710 °C were adequate for our bulk pigment synthesis as at higher temperatures, ~800 °C barium manganate in the pigment system decomposes. When the pigment was fired for two hours versus one hour, the pigment showed a more uniform particle size when

we conducted SEM imaging and granulation particle test. We also determined nitrous acid formed by combining 6 M HCl and sodium nitrite is the best choice for post-synthetic acid treatment over a dilute solution of HCl as it preserves the manganese content and the crystal structure of manganese blue. The stability of the bulk pigment was using TGA and color fastness. For the synthesis of the nanoparticles, we followed a similar synthetic procedure starting with barium sulfate and amorphous manganese(IV) oxide nanoparticles while using bulk barium nitrate. Since the reactivity is higher at the nanoscale, we achieved the synthesis at a temperature that is 190 °C lower than the temperature for the bulk synthesis while following the exact post-synthetic acid treatment. The particle size distribution of the nanoparticles was narrowed down using size selection by centrifugation and for biomedical imaging application they were coated using a dense amorphous silica coating.

In chapter 3, we discussed the in-situ synthesis of Egyptian blue crystals in the core of Egyptian faience. By eliminating sodium chloride from our flux mixture, we were able to synthesize Egyptian blue crystals as sodium chloride inhibits its growth.[14] Since Egyptian blue and Egyptian faience share the same starting materials: a calcium source, copper source, and silicon dioxide, we discovered that by controlling the concentration of the calcium and copper concentrations we were able to create a continuum between Egyptian faience and Egyptian blue. This work was also extended to grow micron-sized Egyptian blue crystals in faience using controlled cooling and air quenching methods. We also accomplished the synthesis of a sample that is a hybrid of faience and Egyptian blue by using 5 wt% calcium hydroxide and 5 wt% copper oxide. From the continuum, we accomplished the synthesis of the Egyptian blue objects using a two-step process. The Egyptian blue objects synthesized by our lab were very similar to an archaeological Egyptian blue object.

In chapter 4, we investigated the possible sources of raw materials such as possible sources of calcium, copper, alkali flux, and even substrates for the in-situ synthesis of Egyptian blue in Egyptian faience. We learned that calcium carbonate from calcite or dolomites, calcium sulfate which is the main component of gypsum, and calcium hydroxide which is the main component of limestone are all possible calcium sources. Natron and halophytic plant ashes were the two main sources of alkali flux for the synthesis of faience and/or Egyptian blue. Our results have shown that the halophytic plant ashes were a better flux compared to synthetic Natron.[15] The plant ashes provided us with a smooth and glassy faience which displayed near-infrared luminescence while the natron sample did not show any luminescence which can be attributed to the presence of sodium chloride which inhibited the formation of Egyptian blue crystals. In archaeological samples with a high Na_2O/K_2O, which could be due to the use of natron as a possible source of flux along with the presence of luminescence from Egyptian blue, suggests that there was possibly a purification process of natron before its use. With regards to the copper sources, we have tested copper oxide, synthetic malachite (basic copper(II) carbonate), and melt flux synthesized bulk Egyptian blue crystals. Copper oxide was the standard source of copper which consistently gave us luminescence from the faience core indicating the possibility of it being a source of copper for the in-situ synthesis of Egyptian blue. Synthetic malachite in SEM images provided us with micron-sized crystals due to its decomposition at ~380 °C to give two moles of copper oxide which gives a copper concentration close to the calcium concentration. From our previous experiments, when the stoichiometry of calcium and copper are close, we grew micron-sized Egyptian blue crystals in the faience core. The substrate on which the faience was fired played an important role in the in-situ synthesis of Egyptian blue in faience core. Substrates such as alumina crucibles for lab synthesis or terracotta for archaeological faience samples could have been potential substrates.

Calcium oxide as a slip layer on terracotta used in ancient times to facilitate the removal of glazed objects as faience unfortunately, inhibited the formation of Egyptian blue crystals.

In terms of future work for manganese blue, we would like to further narrow down the size distribution of the manganese blue nanoparticles controlling the size of barium sulfate nanoparticles which would eventually result in a more uniform and smaller manganese blue nanoparticles.[16,17] Furthermore, we need to evaluate the cytotoxicity of the manganese blue nanoparticles in-vitro and in-vivo for clinical translation.

For faience, feldspars, which are aluminum tetrasilicate minerals that may contain other elements such as sodium, potassium, or calcium, were suggested as a starting material for faience synthesis.[18,19] We have conducted a few preliminary experiments for the in-situ synthesis of Egyptian blue crystals in Egyptian faience but this time using feldspars such albite, labradorite, and oligoclase. The macroscopic morphology of the faience in terms of color and appearance drastically changed from the samples that do not have feldspars in them.

Overall, in this work we have shown how near-infrared luminescent materials, specifically near-infrared luminescent pigments based on copper such Egyptian blue or manganese like manganese blue can be synthesized. In this case we successfully achieved the synthesis of Egyptian blue in a complex matrix such as faience while unveiling the secret for the synthesis of manganese blue and transforming the bulk pigment into nanoparticles for future biomedical applications.

References

1. Cao, R., et al., *Near-infrared emission Ba3 (PO4) 2: Mn5+ phosphor and potential application in vivo fluorescence imaging.* Spectrochimica Acta Part A: Molecular and Biomolecular Spectroscopy, 2014. **128**: p. 671-673.
2. Zhang, X., et al., *Controllable synthesis of Mn6+ doped nanoparticles by a facile anion exchange method.* Nanotechnology, 2016. **28**(2): p. 025604.
3. Zhang, X., et al., *A general strategy for controllable synthesis of Ba 3 (MO 4) 2: Mn 5+(M= V, P) nanoparticles.* RSC Advances, 2017. **7**(17): p. 10564-10569.
4. Cui, Y., et al., *Facile synthesis of near-infrared emissive CdS quantum dots for live cells imaging.* Journal of Nanoscience and Nanotechnology, 2018. **18**(4): p. 2271-2277.
5. Brunold, T.C. and H.U. Güdel, *Absorption and Luminescence Spectroscopy of MnO42--Doped Crystals of BaSO4.* Inorganic chemistry, 1997. **36**(9): p. 1946-1954.
6. Brunold, T.C. and H.U. Güdel, *Absorption and luminescence spectroscopy of manganese-doped BaSO4 crystals.* Chemical Physics Letters, 1996. **257**(1): p. 123-129.
7. Thavapalan, S., J. Stenger, and C. Snow, *Color and meaning in ancient Mesopotamia: The case of Egyptian blue.* Zeitschrift für Assyriologie und vorderasiatische Archäologie, 2016. **106**(2): p. 198-214.
8. Johnson-McDaniel, D., et al., *Nanoscience of an ancient pigment.* Journal of the American Chemical Society, 2013. **135**(5): p. 1677-1679.

9. King, R.S., P.M. Hallett, and D. Foster, *NIR− NIR fluorescence: A new genre of fingermark visualisation techniques.* Forensic science international, 2016. **262**: p. e28-e33.

10. Shahbazi, S., et al., *Preparation, characterization, and application of a lipophilic coated exfoliated Egyptian blue for near-infrared luminescent latent fingermark detection.* Forensic Chemistry, 2020. **18**: p. 100208.

11. Accorsi, G., et al., *Imaging, photophysical properties and DFT calculations of manganese blue (barium manganate (VI) sulphate)–a modern pigment.* Chemical Communications, 2014. **50**(97): p. 15297-15300.

12. Li, D., et al., *Excretable lanthanide nanoparticle for biomedical imaging and surgical navigation in the second near-infrared window.* Advanced Science, 2019. **6**(23): p. 1902042.

13. Accorsi, G., et al., *The exceptional near-infrared luminescence properties of cuprorivaite (Egyptian blue).* Chemical Communications, 2009(23): p. 3392-3394.

14. Giménez, J., et al., *Effect of NaCl on the fabrication of the Egyptian blue pigment.* Journal of Archaeological Science: Reports, 2017. **14**: p. 174-180.

15. Noble, J.V., *The technique of Egyptian faience.* American journal of archaeology, 1969. **73**(4): p. 435-439.

16. Reissig, F., et al., *Sub-10 nm Radiolabeled Barium Sulfate Nanoparticles as Carriers for Theranostic Applications and Targeted Alpha Therapy.* ChemistryOpen, 2020. **9**(8): p. 797-805.

17. Fang, C., et al., *Surface functionalized barium sulfate nanoparticles: controlled in situ synthesis and application in bone cement.* Journal of Materials Chemistry B, 2014. **2**(9): p. 1264-1274.

18. Purowski, T., O. Syta, and B. Wagner, *Mycenaean and Egyptian faience beads discovered in southern Poland.* Journal of Archaeological Science: Reports, 2019. **28**: p. 102023.

19. Rehren, T., *A review of factors affecting the composition of early Egyptian glasses and faience: alkali and alkali earth oxides.* Journal of Archaeological Science, 2008. **35**(5): p. 1345-1354.